JUSTUS-LIEBIG-
UNIVERSITÄT
GIESSEN

Justus-Liebig-Universität Gießen

I. Physikalisches Institut

Design, fabrication and testing of miniaturised electrospray thrusters fabricated by two-photon laser lithography

Design, Herstellung und Test von
miniaturisierten Elektrosprayтriebwerken,
hergestellt mit Zwei-Photonen-Laser-Lithographie

Dissertation

zur Erlangung des Grades
„Doktor rerum naturalium“
im Fach Physik

Fynn Lukas Kunze

Gießen 2024

"Remember to look up at the stars and not down at your feet. Try to make sense of what you see and wonder about what makes the universe exist."

- Stephen Hawking

Betreuer und Erstgutachter:	Prof. Dr. Peter J. Klar
Zweitgutachter:	Prof. Dr. Stefan Schippers

Abstract

The utilisation of electric propulsion systems has become a well-established and integral component of the contemporary space industry, particularly over the past decade. Their enhanced longevity and efficiency render them optimal for use as in orbit propulsion systems for long-term missions and similar endeavours. The number of launches of spacecraft equipped with electric propulsion systems has increased exponentially since 2010 and continues to grow at a steady rate. The necessity for propulsion systems on these satellites is evident; however, established propulsion systems, such as Hall thrusters, are inadequate for the requirements of small- and micro-satellites. It is therefore evident that there is a high demand for specialised micropropulsion systems.

One particularly promising technology that may prove capable of satisfying the need for miniaturised propulsion systems are electrospray emitters. Electrospray emitters represent a subcategory of the electrostatic thruster family. The intrinsic design of these devices ensures their compactness, high efficiency, and the ability to circumvent the necessity for external neutralisation. Their operation is based on the extraction of ions from a liquid ion source. The extraction process is facilitated by the application of a strong, localised electric field, which deforms a fluid meniscus into a so-called Taylor cone. At the apex of the Taylor cone, ions are forcibly extracted from the fluid, subsequently exiting the electrospray emitter in the form of a spray of ions, charged droplets, or a jet of charged fluid. The three most common types of emitter are porous, externally wetted, and capillary.

The objective of this dissertation is to develop miniaturised capillary emitters. In order to achieve a significant degree of miniaturisation, a micro 3D printing method, referred to as two-photon lithography, is utilised. The emitters and supplementary components of the thruster assembly are manufactured using a polymeric base material. The project entails an investigation of the influence of miniaturisation, as well as the realisation of new emitter designs. Furthermore, an experimental characterisation setup has been designed and implemented for the purpose of testing the fabricated emitters. This encompasses time-of-flight mass spectrometry, optical analysis and current measurements.

Zusammenfassung

Der Einsatz elektrischer Antriebssysteme hat sich insbesondere in den letzten zehn Jahren als fester Bestandteil der modernen Raumfahrtindustrie etabliert. Aufgrund ihrer erhöhten Langlebigkeit und Effizienz eignen sie sich optimal für den Einsatz als Antriebssysteme in der Erdumlaufbahn für lang andauernde Missionen und ähnliche Unternehmungen. Die Zahl der Starts von Satelliten, die mit elektrischen Antriebssystemen ausgestattet sind, hat seit 2010 exponentiell zugenommen und steigt weiterhin stetig an. Die Notwendigkeit von Antriebssystemen für diese Satelliten liegt auf der Hand, jedoch sind etablierte Antriebssysteme, wie Hall-Triebwerke, für die Anforderungen von Klein- und Mikrosatelliten nicht geeignet. Daher besteht ein hoher Bedarf an spezialisierten Mikro-Antriebssystemen.

Eine besonders vielversprechende Technologie, die als Mikro-Antrieb fungieren kann, sind Elektrospray-Emitter. Elektrospray-Emitter sind Teil der Familie der elektrostatischen Triebwerke und sind so konzipiert, dass sie kompakt sind, einen hohen Wirkungsgrad haben und keine externe Neutralisierung benötigen. Ihr Betrieb basiert auf der Extraktion von Ionen aus einer flüssigen Ionenquelle. Der Extraktionsprozess wird durch das Anlegen eines starken, lokalisierten elektrischen Feldes hervorgerufen, das einen Flüssigkeitsmeniskus in einem sogenannten Taylor-Kegel verformt. An der Spitze des Taylor-Kegels werden die Ionen zwangsweise aus der Flüssigkeit extrahiert und verlassen den Elektrospray-Emitter in Form eines Ionensprays, von Tröpfchen oder eines Flüssigkeitsstrahls. Die drei gebräuchlichsten Emittertypen sind porös, extern benetzt und kapillar.

Ziel dieser Dissertation ist die Entwicklung von miniaturisierten Kapillaremittern. Um einen signifikanten Miniaturisierungsfaktor zu erreichen, wird ein Mikro-3D-Druckverfahren, die so genannte Zwei-Photonen-Lithographie, eingesetzt. Die Emitter und die ergänzenden Komponenten der Triebwerksbaugruppe werden aus einem polymeren Basismaterial hergestellt. Das Projekt umfasst die Untersuchung des Einflusses der Miniaturisierung sowie die Realisierung neuer Emitterdesigns. Außerdem wurde ein experimenteller Charakterisierungsaufbau entworfen und implementiert, um die hergestellten Emitter zu testen. Dieser umfasst Flugzeitmassenspektrometrie, optische Analyse und Strommessungen.

Contents

Chapter 1

Introduction

There has been a gradual increase of interest in space applications over the past two decades. The collection of data, the transmission of information and the observation of the Earth's surface drive the development of interest in space applications at the administrative and governmental levels. From approximately the early 2000s onwards, new private companies amassed in excess of $20 billion in funding over the period between 2000 and 2018 [2]. The term "new space" was first coined to describe this increase in funding and competitiveness in the sector, which had previously been dominated by government entities. Although the term "new space" is not precisely defined, it is most commonly attributed to a change in mindset and risk management of the newly founded companies [2]. The companies associated with this paradigm shift are more inclined to assume financial risks with the ob-

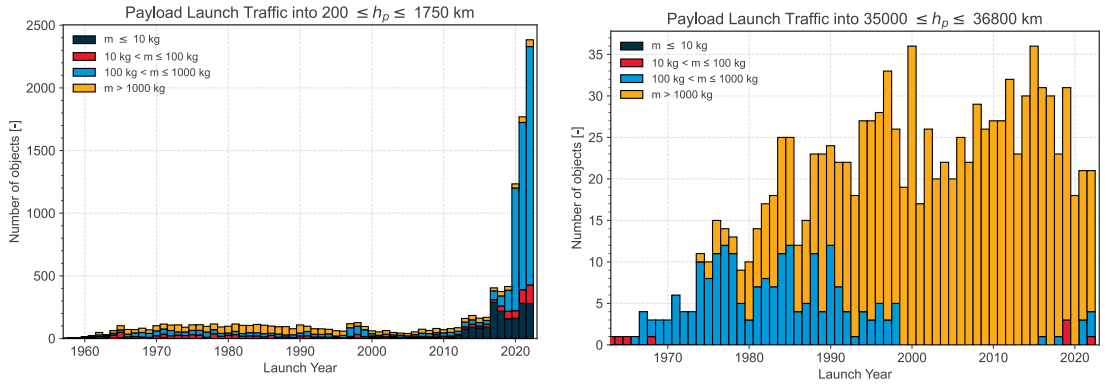

Figure 1.1: The charts illustrates the distribution of payload launches by orbit and object mass. The graphic on the left depicts the number of objects launched annually into an orbit height range of 200 km to 1750 km. The right-hand graph illustrates the number of objects launched on an annual basis into an orbit with a height range of 35000 km to 36800 km. In both plots, the objects are classified into distinct categories based on their respective masses. Source: [1]

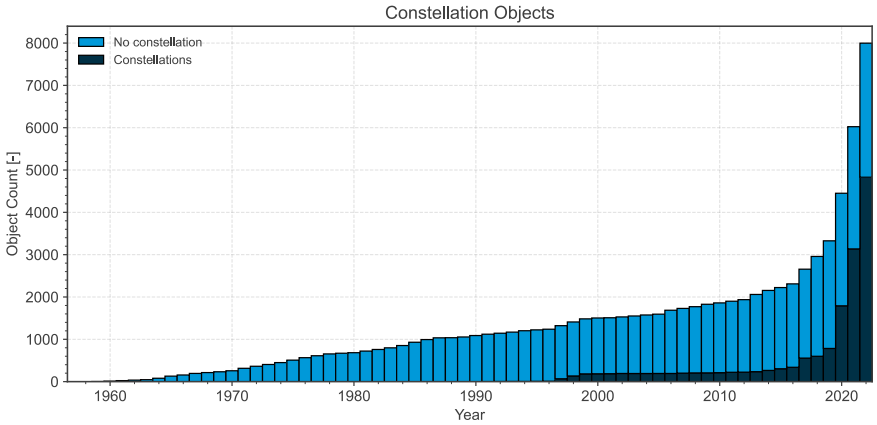

Figure 1.2: The number of objects contributing to a constellation in low Earth orbit (LEO) is illustrated in the accompanying graph, which depicts the total number of objects in LEO over a period of years. The objects have been categorised according to whether they contribute to a constellation or not. Source: [1]

jective of accelerating the development of launch and satellite systems, as well as reducing the costs associated with launching payloads into orbit. A case in point is the company SpaceX, which has enjoyed considerable success with its approach to the development of launchers and its mega constellation, StarLink [2]. This increase in space activities results in a notable increase in the number of both active and inactive spacecraft in Earth orbit [1]. The European Space Agency (ESA) reports an exponential growth in the number of objects launched into Earth's orbit, with the most significant changes observed in low Earth orbit (LEO). Moreover, the type of spacecraft launched into orbit has undergone significant changes over the past decade, with a notable shift towards smaller satellites in recent years [1]. In the early 2000s, the majority of telecommunication satellites were launched into geocentric Earth orbit (GEO). However, from approximately 2006 onwards, there was a notable shift towards the deployment of smaller satellites in lower orbits. Figure 1.1 illustrates the distribution of satellites in low Earth orbit (LEO) and geosynchronous Earth orbit (GEO). As can be observed from the graphs, there has been an exponential increase in traffic in the LEO, while there have been almost no changes in the GEO. The majority of traffic in LEO is attributable to satellites with a mass of 100 kg to 1,000 kg, which are classified as small satellites. The increase in traffic can be attributed, at least in part, to the advent of constellations, as illustrated in Figure 1.2. Over half of the satellites with a mass of 100 kg to 1,000 kg contribute to constellations in the LEO. Furthermore, it is notable that despite the majority of traffic being caused by small satellites, a significant portion is contributed to cubesats with a mass of less than 10 kg. The emergence of constellations has also led to an increased demand for affordable and commercially

viable propulsion systems. Additionally, there has been a rise in the number of countries advocating for the establishment of space laws, with a particular focus on regulating the usage and end-of-life management of spacecraft in orbit. France, for instance, requires a dedicated "end-of-life" strategy for orbital systems, entailing either a scheduled re-entry or the placement in a graveyard orbit [3, 4]. With an on-board propulsion system, the planned re-entry can be accelerated, thereby reducing the probability of collisions.

In light of the growing interest in cost-effective, miniaturised thruster solutions, electrospray emitters were identified as a potential technology for consideration in this project. Electrospray emitters, also known as colloid emitters, are classified as a type of electrostatic thruster [5]. The primary advantages of electrospray emitters are their minimal power requirements, straightforward access to propellants, and their capacity for miniaturisation. This renders them an optimal technology candidate for a miniaturised thruster system for small and micro satellites. A commercial implementation with flight heritage of this technology is already in place. The Austrian company ENPULSION has been highly successful in the commercialisation of an electrospray thruster utilising porous metal emitters and indium as a propellant. To date, they have deployed in excess of 200 thrusters in orbit, primarily on small satellites [6]. The heritage thrusters produced by ENPULSION are capable of delivering thrusts ranging from 300 µN up to 1 mN, with an input power of 40 W to 105 W [7]. This makes them an attractive propulsion system for smaller satellites. Nevertheless, there is scope for further enhancements to the technology. The emitter needles utilised by ENPULSION are on the centimetre scale and significantly exceed the limits of miniaturisation. Furthermore, it should be noted that ENPULSION's thrusters require the use of an external neutraliser in order to operate.

The objective of this project is to advance the development of electrospray thrusters to the next generation. This will entail the further miniaturisation of both the emitter structures and the thruster as a whole to the micro scale. The reduction in size facilitates enhanced flexibility for the thruster system. In contrast to the use of a single digit number of emitters, the new approach is to employ a significant number of micro-emitters in parallel. The desired level of thrust is achieved by employing a scaling-up by numbering-up paradigm. This approach enables the adaptation of the thruster system to a wide range of small and micro-satellites. Furthermore, the new type of emitter is designed for the utilisation of ionic liquids as propellant and for operation in both polarities. This eliminates the necessity for an external neutraliser, thereby enhancing the flexibility of the system. In order to achieve the desired miniaturisation, a compatible manufacturing method was selected. In a previous project, two-dimensional planar photo lithography was employed for the fabrication of flat capillary-type electrospray emitters [8–10]. In

line with the findings of the preceding project, the decision was taken to alter the manufacturing method from 2D planar photo lithography to 3D two-photon lithography. This defines the initial objective of the project. This entails the adaptation of the preceding results to the recently selected manufacturing technique, namely a transition from planar 2D geometries to 3D geometries. The project's objective is to plan, design and fabricate electrospray emitters from polymer using 3D two-photon lithography. As the 3D capabilities offer completely novel geometric approaches to the emitter structure, this objective also encompasses the identification and characterisation of new geometries for emitter structures. The second objective is the design and assembly of a testing facility that allows for the characterisation of the aforementioned emitter structures. The third and final objective of this project is the miniaturisation of the complete electrospray thruster assembly, which includes the emitter structures, the extractor electrode and peripheral emitter parts.

Chapter 2

Theoretical foundations

2.1 Electrospray thrusters

Electrospray thrusters represent a subcategory of the broader electrostatic thruster family. This thruster type extracts ions from a conductive liquid propellant and accelerates them using a static electrical field [11, 12]. The required electrical field is generated by an applied voltage between the liquid propellant and an extraction electrode situated in the emission direction [13]. The thrust generated is a function of the accelerated ions and is determined by the molecular mass of the propellant and the applied voltage. In comparison to other common electric propulsion systems, such as ion engines or Hall thrusters, electrospray emitters utilize a liquid ion source (LIS) instead of ionized gases [11, 12, 14–16]. A liquid ion source may be constituted by a liquid metal exposed to a strong electrical field or an ionic liquid [17]. Electrospray thrusters utilising a liquid metal ion source are also commonly referred to as field emission electric propulsion (FEEP) [6, 16, 18, 19]. Figure 2.1 depicts a computer-generated illustration of an exemplar of an electrospray emitter with an integrated extraction electrode. The operational principles of electrospray thrusters will be discussed in greater detail below.

Electrospray thrusters possess a number of significant advantages, which collectively position them as a highly promising technology for small and micro spacecraft among the various electric thruster types [20]. They offer an extremely favourable ratio of electrical power to thrust, as well as a high mass efficiency. In contrast to Hall thrusters and ion engines, there are no losses of propellant due to neutral gas losses. Furthermore, the vacuum-stable liquid propellant exhibits almost no propellant loss due to evaporation. The combination of a very high specific impulse of 1,000 seconds to beyond 4,000 seconds and the minimal propellant loss, result in an overall very high mass efficiency [6, 18, 19, 21]. As the propellant is readily ionized by the static field, or is already ionized in the case of ionic liquids, the energy cost for generating ions is minimal. Consequently,

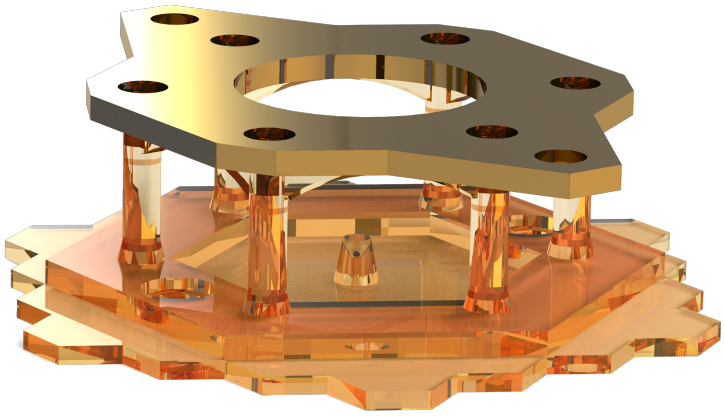

Figure 2.1: Computer-generated image depicting an electrospray thruster comprising a capillary emitter with an integrated extraction electrode. The emitter design, developed during this project, comprises three parts: the emitter plate with the emitter structure and the bottom; a spacer layer which separates the emitter from the extraction electrode; and the extraction electrode itself.

the majority of the input power is directly translated into thrust [21]. Additionally, this technology exhibits excellent miniaturization capabilities, as electrospray thrusters are inherently compact and can be further miniaturized without compromising efficiency. In contrast to the majority of plasma-based thrusters, which experience a decline in performance upon miniaturization, electrospray thrusters can actually benefit from the miniaturization process, depending on the design of the emitter [16, 21–24]. Moreover, the handling of the liquid propellant is considerably more straightforward than for gaseous propellants, as there is no requirement for pressure vessels. In the case of a liquid metal ion source, the propellant may be in a solid state, when the thruster is turned off and only heated and liquefied during operation, thus, further simplifying the handling process [18, 19]. Electrospray thrusters are capable of providing highly precise thrust and impulse bits, rendering them optimal for precision movement and station keeping. This quality makes them particularly attractive for constellation flight or low Earth orbit (LEO) operations [6, 25]. Additionally, electrospray emitters operating with ionic liquids possess the unique ability to emit ions of both positive and negative polarity. By alternating between these polarities, it is possible to achieve active charge balancing of the spacecraft, reducing the necessity for an external neutraliser [26–28].

Overall electrospray thrusters offer a wide variety of advantages for small and micro spacecraft; however, these systems also have their drawbacks. The total thrust generated by electrospray propulsion systems is relatively low, which renders them less suitable for use in larger spacecraft [25, 29]. This can be mitigated to some extent by increasing the number of thrusters, but it is ultimately constrained by the size of the spacecraft and the diminishing returns associated with additional

mass. Another significant challenge is the lifetime of these propulsion systems. The thrusters are known to experience issues with the deposition of propellant on the extraction electrode, which can result in a degradation of performance or even a failure of the entire system. As the propellant is vacuum-stable, it cannot be removed passively; thus, either active cleaning procedures or more complex designs are necessary to counteract this deposition [6, 30, 31]. Furthermore, the handling of propellants in the absence of gravity presents an additional challenge. In the absence of gravity, the out-gassing or residual gases in the liquid propellant can become a significant issue, as the gases are unable to rise or leave the fluid. This can result in the formation of bubbles in the liquid or the occurrence of spontaneous overflows in the emitter structures. Overflowing emitter structures represent another challenge for electrospray thrusters [32]. Depending on the emitter design, an overflow can directly cause a short circuit, rendering the thruster unusable.

A comparison of the advantages and challenges indicates that, in the majority of cases, the advantages outweigh the disadvantages. This is particularly evident in the context of small and micro spacecraft. In light of the prevailing trends in launches, as outlined in Chapter 1, there is a notable increase in scientific and commercial interest in electrospray thrusters. Furthermore, given the potential for further improvements that could address or resolve many of the current challenges, this interest is likely to continue to grow.

2.1.1 Principle of operation of electrospray thrusters

As previously stated, electrospray thrusters operate by extracting ions or charged droplets of a conductive liquid propellant via a static electrical field. Subsequently, the ions or droplets are accelerated by the same field, thereby generating thrust. The extraction of ions is a direct consequence of the interaction between the fluid and the electrical field [5, 33–35]. In the absence of an applied electrical field, the fluid assumes the form of a droplet or meniscus, shaped by the combined effects of viscosity and surface tension. Once the conductive fluid is exposed to an electrical field, a process known as charge polarization ensues. The direction of the field determines whether a negative or positive charge is accumulated in the vicinity of the fluid's surface. The charges are subject to the Coulomb force, which gives rise to a tangential and normal component in relation to the fluid surface. Moreover, a dielectric force acts to displace the charges in an outward direction, typically along the surface of the fluid. The fluid attains a state of equilibrium between the internal cohesion forces (surface tension and viscosity stress) and the external electrical forces (dielectric and Coulomb forces), which results in a deformation of the fluid meniscus [33–37]. In the majority of cases, the internal forces exert a considerably greater influence than the external electrical forces generated by weak electrical fields. This results in only minimal deformation. However, an

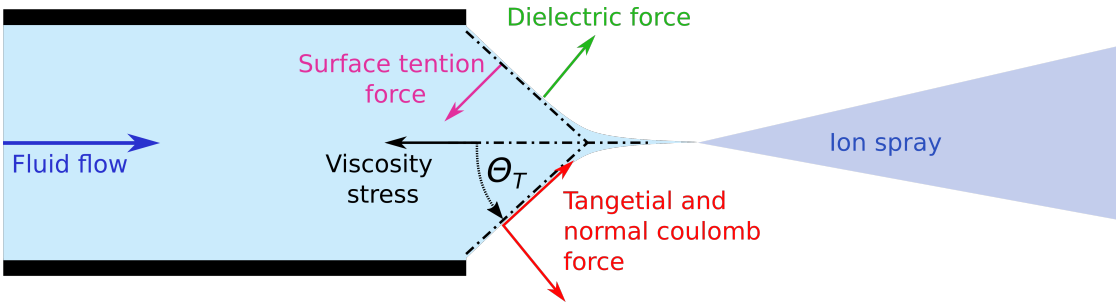

Figure 2.2: Schematic drawing depicting the Taylor cone in the process of ion emission. It should be noted that this drawing assumes rotational symmetry along the central axis. The half angle of the cone, also referred to as the Taylor angle, is represented by the symbol θ_T. Taylor used a static model to describe the physical process behind the cone formation. In this model in the state of equilibrium of forces, the angle is calculated to be 49.3 ° [36]. Additionally, the acting forces and their direction, which define the Taylor cone, are outlined by arrows. The relevant forces are the surface tension force, the viscosity stress, the dielectric force and the tangential and normal Coulomb forces. For the Taylor cone to form, it is assumed that a voltage is applied to the fluid and that there is an electrode connected to ground downstream. Graphic adapted under © from [37]

intensification of the electrical field strength will result in an augmentation of the external electrical forces. As the external electrical forces approach a magnitude similar to that of the internal forces, the deformation becomes more severe, resulting in the formation of a cone-like shape. This phenomenon was documented for the deformation of water droplets by Geoffrey Taylor in 1964 and was given the name "Taylor cone" [33–36, 38]. Figure 2.2 depicts a schematic representation of a Taylor cone and the forces acting upon it. The typical half angle of a Taylor cone is 49.3° , which can be calculated from the equilibrium of the forces acting upon it [33–36, 38, 39]. The precise electrical field required for the formation of a Taylor cone is contingent upon the physical properties of the fluid in question. Nevertheless, the resulting cone shape remains consistent. A significant attribute of the Taylor cone is the intense local electrical field that acts upon its tip. The tip of a Taylor cone is typically only nanometers in diameter, rendering it susceptible to an extreme local electrical field given its minute volume. In this environment, ions are dislodged from the fluid as the acting electrical forces prevail over the internal cohesion forces [33–36, 38–40]. The ions are then accelerated within the electrical field and exit the area of the Taylor cone as a fine spray. This phenomenon lends the thruster its designation of "electrospray".

Multiple factors can influence the emission behaviour of the Taylor cone. The characteristics of the emitted particles can depend on the applied field, the flow rate, and the characteristics of the fluid in question [41]. Furthermore, the Taylor cone can emit charged droplets of varying sizes or a constant jet of fluid. The

charged droplets typically consist of quasi neutral pairs and additional ions. Such droplets can also split into neutrals and ions after leaving the area of emission. The continuous emission is called cone jet mode, and can be stable or exhibit motion patterns like a whip, or alternatively, they can manifest in transient modes that are a combination of the aforementioned characteristics [21, 31, 42–45]. Each emission mode is designated a distinct nomenclature for its description and has varying applications. For example, the pure ionic mode is characterised by the emission of pure atomic or molecular ions. In this mode, the ions are accelerated to high velocities due to their low mass, resulting in a high specific impulse (I_{sp}). This mode is highly mass-efficient, rendering it an optimal choice for electric propulsion systems [11, 46]. However, this mode also exhibits a very low mass flow rate, which results in a corresponding low thrust. In the event that the cone begins to emit droplets in addition to pure ions, the mass flow rate will be considerably higher for the same emitted current. The droplets typically carry multiple ions of opposing charge, with only an imbalance of one or two charges. This results in a markedly different charge-to-mass ratio compared to pure ion emission. Depending on its size a single charged droplet can readily transport a mass two to ten times greater than that of a pure ion [21, 43]. This results in a reduction of the acceleration of the droplets, which in turn leads to a lower I_{sp}. Nevertheless, the elevated mass flow rate at a constant emission current yields increased thrust. In light of these considerations, it becomes evident that each emission mode possesses distinctive advantages and disadvantages. The selection of the optimal emission mode in a given situation provides a high degree of flexibility within an electrospray system. Nevertheless, this also necessitates the precise regulation of emission parameters, such as electrical field strength, to prevent the transition from one emission mode to another [21, 31, 42–45].

2.1.2 Emitter types and designs

In order to facilitate the ion emission in a controlled manner, it is possible to utilise structures that are capable of shaping the electrical field or of moving and retaining the fluid within a specified volume. Such structures are referred to as emitters or emitter structures. The use of emitters has been demonstrated to significantly enhance the predictability of ion emission, thereby facilitating the reproducible generation of ions under designed operational parameters. In order for electrospray to be successfully applied in an electric propulsion system, it is essential that both reproducibility and reliability are achieved. The majority of emitter structures can be classified into one of three categories. All three types of structure operate on the same fundamental principle, as outlined in Section 2.1.1. However, there are significant differences in the manner in which they move and expose the conductive liquid to the electrical field. The three emitter types are externally

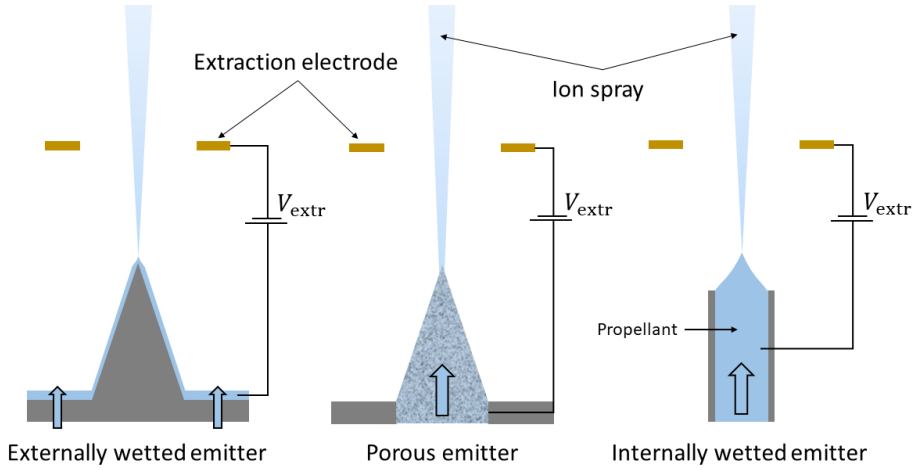

Figure 2.3: Schematic illustration depicts the three most prevalent emitter types. From left to right, the externally wetted emitter, the porous emitter and the internally wetted capillary emitter. While all three types employ the same fundamental emission process, they utilise different mechanisms for the propellant transport. The light blue arrows delineate the propellant flow for each emitter type. Moreover, the requisite extraction electrode and associated extraction voltage are illustrated in the diagram. Graphic adapted under *from [21]*

wetted emitters, porous emitters and internally wetted capillary emitters [11, 21, 47–50]. Figure 2.3 illustrates the schematic representation of each emitter type, highlighting the principal distinctions between them.

The first emitter type, the externally wetted emitter (depicted on the left side of Figure 2.3), provides and exposes the liquid through surface forces. The operation of these devices is facilitated by the application of a liquid to the surface of the emitter base. Subsequently, the fluid is drawn towards the emitter by surface forces [51, 52]. In the majority of instances, externally wetted emitters are coated with a material that enhances the adhesion of the fluid and facilitates wetting behaviour. One example of such a coating is a layer of nano wires [53]. The nano wires exert capillary forces on the fluid, thereby pulling and maintaining it along the surface of the emitter. Typically emitters are shaped in a cone-like manner or feature sharp edges or corners. Such shapes facilitate the concentration of the electrical field at the emitter's tip, thereby localising the ion emission. At the tips, the electrical field strength is significantly enhanced in comparison to a flat surface. This phenomenon can be attributed to the gradient of the electrical field and is analogous to the effect observed in a lightning rod [54]. Externally wetted emitters can be manufactured from a wide range of materials. The most commonly used materials are metal needles and silicon [51, 52]. Metal needles are employed in the

fabrication of macroscopic emitters with a diameter of up to several millimetres, whereas silicon is the material of choice for the production of microfabricated emitters. The most common range for microfabricated emitters is between 1000 µm and less than 50 µm, with a variety of sizes and shapes [51, 53]. Such emitters can be manufactured by wet etching of silicon wafers or micro-machining of wafers with an ion beam or conventional mechanical methods. These emitters are generally the most straightforward to manufacture due to their comparatively simple shape and the readily available processing methods. Although externally wetted emitters are more straightforward to manufacture, they are also constrained in terms of design flexibility. The surface wetting restricts the potential for modifications to the shapes of the emitters and reduces the flexibility of the thruster design. Furthermore, externally wetted emitters are confronted with a considerable obstacle in regard to the propellant delivery. It is of the utmost importance to ensure that the influx of fluid is carefully balanced. In the event that an excess of fluid accumulates between the emitter structures, the potential for the formation of secondary emission sides arises [31, 53]. Secondary emission refers to the extraction of ions from a larger droplet of propellant, and is, in general, an unpredictable phenomenon. It results in uncontrolled wetting of other thruster parts. This has a particularly detrimental effect on the extractor electrode, which can result in short circuits and accelerated degradation of the thruster, thereby reducing its lifespan considerably [31, 55].

The second category of emitters is the porous emitter. Figure 2.3 illustrates a porous emitter in its centre. Porous emitters are manufactured from porous materials, as the term "porous" would suggest. The two most commonly utilised materials are of a distinct nature. One of the two material types are porous metals, such as tungsten or titanium sponges [11, 48]. The aforementioned metals are typically shaped into emitters via a mould sintering process or machined from a metal sponge. The second category of materials comprises non- or semi-conductor materials, including porous glasses and silicon [16, 50, 56]. The most common method of manufacturing emitter from these materials is through machining or etching. Porous emitters are typically similar in shape and manufacturing to external emitters, with cone shapes being the most common. A significant distinction between porous and externally wetted emitters is the manner in which the former facilitate the transfer of propellant to the emission sites. The porous microstructure enables the propellant to flow through the material itself, in a manner analogous to the flow through a sponge. The capillary forces exerted by the minute pores draw the liquid propellant from a reservoir or superstructure, thereby establishing a passive propellant feeding system that supplies propellant to the entire structure. Upon reaching the tip of a coned emitter, the propellant forms a Taylor cone on the pore's orifice, thereby initiating ion emission. A notable benefit of the porous microstructure is that porous emitters are capable of exhibiting multiple

emission sites on a single emitter [48, 57]. The tip of such an emitter has a high density of pores facing the extractor electrode, allowing multiple pores to emit ions in parallel. This significantly enhances the ionic current that can be emitted from a single emitter. However, this advantage is accompanied by a disadvantage. The porous structure is inherently dependent on a statistical distribution of the pores, which significantly reduces the predictability of the emitters in case of miniaturised devices. No two emitters will be identical, and the variation in fabrication will affect the emission behaviour of each emitter. This gives rise to a certain degree of uncertainty with regard to the thruster system, insofar as there is a possibility that the emission site may spray onto the extractor electrode or onto another location [57]. Furthermore, the miniaturisation of the emitters is contingent upon the base material employed. If the pore size of the material is too large, the emitters cannot be miniaturised beyond a certain point. As the lateral dimension of the process approaches the same magnitude as the emitter dimensions, miniaturisation becomes challenging [58, 59]. Overall, the majority of manufacturers and research groups focus on this type of emitter due to its high current output and inherent propellant feeding mechanisms, making it the most used emitter type in electrospray propulsion systems.

The third category comprises capillary emitters, which are also referred to as internally wetted emitters. The present study is primarily concerned with this particular emitter type. On the right-hand side of Figure 2.3, an example of an internally wetted emitter is provided. Capillary-type emitters constitute the most prevalent type of electrospray emitter, because they were the first ones used. At the outset of the investigation into the electrospray phenomenon, steel capillaries were employed to facilitate ion emission. Furthermore, macro capillary emitters are widely used in mass spectrometry experiments as a means to ionise sample material [33, 34]. For this application a Nobel price was awarded in 2002 [60]. However, they have seen little use in electric propulsion systems in recent years. Internally wetted emitters utilise a capillary system to facilitate the movement of fluid towards an orifice [33–36, 38, 42]. At the orifice, the fluid is exposed to the electrical field, whereby it forms a Taylor cone under the influence of the field. Figure 2.2 provides a more detailed illustration of this process. In contrast to externally wetted or porous emitters, the configuration of the capillary has a relatively limited impact on the emission process. As the fluid meniscus constitutes the cone itself, no external assistance is required for the emission of ions. The key factors influencing the emission at the macroscopic level are the propellant flow rate, the capillary orifice diameter and the local electrical field [21, 31, 43]. A significant benefit of capillary emitters is their capacity for scalability. The reduction in propellant flow rate that occurs as a result of the miniaturisation of the capillary orifice leads to an increase in the efficiency of the emitters. A reduction in flow rate increases the likelihood of the emitter operating in pure ionic

emission mode [22]. Nevertheless, reducing the flow rate represents a significant challenge. There are multiple ways to achieve a lower flow rate for capillary-type emitters. One obvious approach is the miniaturisation of the emitters, which has already been mentioned. By reducing the diameter of the capillary for a given pressure difference, the flow resistance decreases in accordance with the law of Hagen-Poiseuille. The law of Hagen-Poiseuille provides a means of calculating the flow rate $\dot{V}$ for a given system. The flow rate $\dot{V}$ is given by pressure gradient over the length of the capillary $\frac{\mathrm{d}p}{\mathrm{d}x}$ multiplied by π and the 4^{th} power of the capillary radius r divided by eight times the viscosity of the liquid η.

Given the law of Hagen-Poiseuille, one method of reducing the flow rate is to decrease the diameter of the capillary. The radius exerts the greatest influence on the volume flow, with an impact that is proportional to the fourth power of the radius. To illustrate this, a reduction in the diameter of the capillary by half will result in a decrease in the volume flow by a factor of 16. Given the aforementioned characteristics of capillary-type emitters, namely their enhanced efficiency at low flow rates and the significant reduction in flow rate that can be achieved by reducing the capillary diameter, it is evident that downscaling the emitters is a logical conclusion. Nevertheless, downsizing the emitters to the micro level represents a significant challenge. At the time this phenomenon was first identified and proposed for use as a propulsion system, the manufacturing options were limited, which led to the cessation of this approach. It was only with the advent of microfabrication technology in the early 2000s that efforts were made to manufacture micro-scale capillary-type emitters [8, 15]. One method of manufacturing a miniaturised micro emitter is by the etching of channels into silicon [61]. This process yields microcapillaries with a diameter of 10 µm or less. An alternative approach is to additively manufacture the capillary structure from a polymer using, for example, a stereo or 3D lithography device. Nevertheless, the downscaling of the emitters presents an additional challenge. The high degree of miniaturisation necessitates precise control of the pressure or feeding rate of the capillaries. Overspilling is a common issue with miniaturised capillary-type emitters [32, 61]. It has been demonstrated during this study that only reducing the capillary diameters is an ineffective solution to this problem. Furthermore, at this microscopic scale, influences such as capillary forces and surface tension become significant factors that must be considered. This results in a system that is difficult to control, with a fragile balance of input pressure and fluid feed rate. In order to address this challenge from multiple perspectives, one research group attempted to infuse capillaries etched from silicon with silica beads. The objective was to affix the beads to the internal surface of the capillary in order to impede the flow of the propellant and thereby reduce the likelihood of overflow. An alternative approach was to increase the fluid path by manufacturing fluid channels of considerable length, which would increase the flow resistance due to the high surface friction along

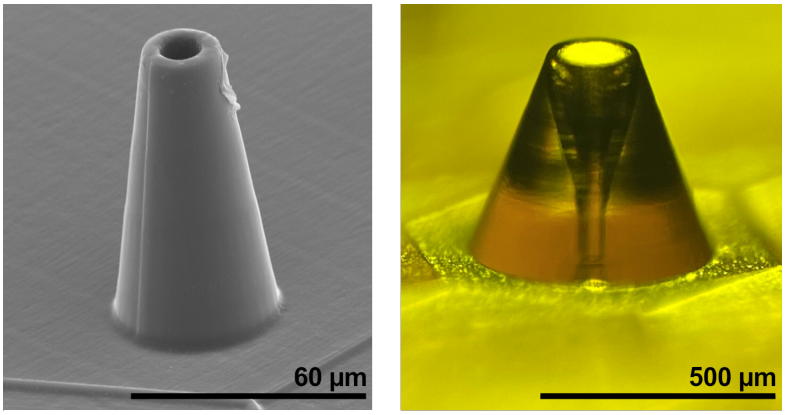

Figure 2.4: Images depicting a emitters that have been fabricated by additive 3D micro-printing using two-photon lithography. The image on the left is a scanning electron microscope (SEM) image of a single microcapillary emitter. The emitter features a straight capillary with a diameter of 10 µm , which is manufactured from SU-8 polymer. The image on the right was captured using an optical microscope. The image on he right depicts a single emitter, with the capillary modified to resemble a diverging nozzle. The diameter of the capillary is 60 µm at its narrowest point and widens to 200 µm at the tip. The material is an IPx-Q polymer, a photosensitive resin developed for use in two-photon lithography applications.

the way [32, 61]. The research that led to this work addressed the challenge by modifying the geometry of the emitter. The utilisation of micro 3D printing technology, coupled with the freedom of design afforded by 3D capabilities, enables the fabrication of capillary emitters with more sophisticated capillary designs and increased flow resistance. Moreover, the 3D printed designs are more suitable to account for and manipulate the influence of surface tension and capillary forces, thereby offering a greater range of possibilities for adjusting the flow through the emitter [23, 24]. Images of examples are provided in Figure 2.4. The images illustrate the versatility of the additive manufacturing approach. It is feasible to fabricate an emitter comprising "classical" straight capillaries, as illustrated in the left-hand image of Figure 2.4. Moreover, modified capillaries can also be manufactured. The image on the right-hand side of Figure 2.4 depicts an emitter featuring a diverging capillary, which widens from 60 µm to 200 µm in diameter. Such a design is very difficult to create using non-additive manufacturing methods, especially if the structures are on the micrometre scale.

The selection of capillary emitters for this project was based on a number of considerations. As previously stated, they display highly favourable behaviour upon miniaturisation. The downscaling process is relatively straightforward, and their design is well-suited to the chosen additive manufacturing method of 3D lithography. While porous emitters can be manufactured additively, the available methods have yet to demonstrate efficacy in micro-scale fabrication. Moreover, the findings

of previous projects provided support for the decision to continue the research with a capillary design. The new freedom of design for the shape of the capillary allows for the exploration of a broad field of geometries. The combination of the selected micro fabrication method and capillary design enables the fabrication of emitters that are more than one magnitude smaller than those found in commercially available thrusters [7]. Moreover, the integration possibilities and rapid prototyping afforded by 3D lithography permit a more flexible approach to thruster designs. There are few manufacturing methods that allow such a high degree of freedom of design and miniaturisation capabilities, making this approach a novel development in the field. There has been limited research conducted on miniaturised additive manufactured electrospray emitters, which makes this project appealing not only for the development of a thruster system, but also for fundamental research into electrospray process.

2.1.3 Electrospray thruster systems with flight heritage

A considerable number of electrospray thrusters are currently in development or are already commercially available. Nevertheless, only a small number of these have reached a qualified state and have been flight-tested. The most successful are the thrusters from ENPULSION, which were previously referenced. Their indium-based FEEP thrusters are capable of delivering thrusts ranging from 300 µN up to 1 mN, with an input power of 40 W to 105 W [7]. The required power includes the external neutraliser necessary for operation. Each thruster features a "crown" of emitters, that are made of of porous tungsten and are fabricated by mould inject sintering. The resulting emitters are about 1 to 2 cm in hight and 1 to 2 mm in diameter, which places them outside the the currently possible miniaturisation capabilities. This also is reflected in the low number of emitters per thruster, with typically feature only 20 to 30 emitters. The thruster reaches a specific impulse of 1500 s to 6000 s depending on its configuration and are designed to fit into a standard cube-sat module, with a size of one U. They are marketed towards multi-U cube-sats and small spacecraft. With over 200 thrusters currently operational in space, this is one of the most successful thruster series for small spacecraft.

Another exemplary thruster system is the "BET-MAX Electrospray Thruster System", developed by Busek. This thruster employs porous glass emitters in conjunction with the ionic liquid EMI-Im, and is designed for use on small platforms of 3U and above. The system can provide thrust between 1 µN and 150 µN, and is designed for precision thrust and orbital control. With an input power of 24 W, this system is intended for deployment on very small satellites with limited available power. [62]. The thruster operates with a specific impulse of 850 s to 2300 s. There is also none information available regarding the specific the emitter sizes and designs. A comparative analysis of the available thruster systems reveals that

the Busek BET-MAX is the most closely aligned with the project goals. Nevertheless, the Busek thruster necessitates the utilisation of an external neutraliser and exhibits a considerable degree of rigidity in its operational scope, which leaves still room for further improvements.

A newer and less establish thruster is IENAI's ATHENA thruster. The thruster was tested in flight in 2022 on a technology demonstration platform, but has yet reached marked maturity. According to specifications listed by IENAI the thruster has a thrust to power ration of 30 to 50 µN/W, a specific impulse of 1600 to 2000 s and a system efficiency of 30 to 40%. ATHENA is based on an externally wetted silicon emitters with lateral dimensions in the range of 100 to 200 µm The thruster features an externally aligned extractor electrode with some modularity. However, more information on the system is not available [63].

2.2 3D printing and two-photon-lithography

2.2.1 Additive manufacturing by 3D printing

The advancement of three-dimensional printing technology has been rapid since its initial introduction in the early 1990s [64]. What began as a niche technology has evolved into a fabrication methodology that offers a multitude of advantages for the production of components. From the reduction in material costs, faster fabrication times, to the possibility of manufacturing parts that are impossible to manufacture via conventional methods, 3D printing has become a focus of industrial manufacturing. A plethora of 3D printing technologies are currently available. The range of materials and application types is vast, encompassing laser-based metal sintering processes, thermoplastic polymer extrusion, and light-based polymerisation printing, among others [65–68]. Given the evident advantages of these technologies, it is unsurprising that 3D printing has become a major tool in the field of space technology [69]. For instance, 3D-printed rockets are currently undergoing further development, with some prototypes already in use [67, 70, 71]. The rapid prototyping available with additive manufacturing and 3D printing has the effect of

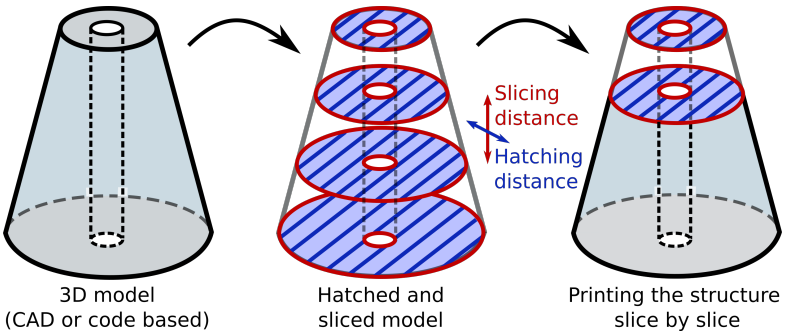

Figure 2.5: Typical process flow for an additive 3D printing process, from a 3D model to the printing process. Initially, a 3D model is generated, either by utilising computer-aided design (CAD) software or program code. An exemplar of a 3D model is illustrated on the left of the schematic. Subsequently, the generated model is imported into a dedicated software program, referred to as a "slicer." This software divides the 3D model into thin layers, or "slices." The schematic in the centre illustrates an exemplar, with the slices delineated in red. Each slice is separated from the adjacent slices by a distance designated as the "slicing distance."The slicing distance is selected in accordance with the printing parameters and the employed printing system. Subsequent to the division of the 3D model into slices, each individual slice is subdivided into parallel or concentric lines. This procedure is referred to as "hatching," and the distance between the lines is termed the "hatching distance." An exemplar of the hatching process is illustrated in the central drawing, wherein blue lines are employed. Subsequent to the slicing and hatching of the 3D model, a file format readable by the printer is generated. This file contains all data obtained from the slicing process and is translated by the printer into a set of instructions. With this set of instructions, the printer initiates the printing of the desired 3D structure, as depicted in the rightmost drawing.

shortening development cycles and speeding up research and innovation. Another area of development in 3D printing technology is microfabrication, especially for medical and semiconductor applications [72]. Light-based lithography processes represent a well-explored method of manufacturing 2D and 3D microstructures, offering the potential for the fabrication of features in the micrometre to nanometre range [8, 9, 66]. The specific method employed determines the achievable feature size [23, 24, 73].

The majority of 3D printing technologies adhere to a highly analogous process flow. A considerable number of methods are only capable of printing from a single point. Examples of such methods include powder bed fusion, fused deposition modelling (FDM) and laser lithography. Only a small number of technologies is capable of printing two-dimensional structures in a single process. An exemplar of this is stereo lithography (SLA) printing. Nevertheless, all of the aforementioned methods are capable of directly fabricating three-dimensional structures. The typical process flow for 3D printing is illustrated in Figure 2.5. The initial step is the generation of a 3D model, which can be achieved through the utilisation of computer-aided design (CAD) software or program code. An exemplar of a three-dimensional structure is illustrated on the left side of Figure 2.5. Subsequently, the generated model must be processed by a slicing software. A slicer software program, or simply "slicer," divides the model into thin layers, or "slices". The slices are separated by a predefined distance, referred to as the slicing distance. The slicing distance is contingent upon the process parameters and the selected printing method. To illustrate, a reduction in the slicing distance results in a closer proximity of the layers. This results in an enhanced resolution of slopes and other features. However, it also results in an increase in processing time, as the printing process is required to perform progressively more iterations. Moreover, some printers are constrained by a minimum slicing distance, which is determined by physical limitations, such as the precision of a stepper motor. Figure 2.5 illustrates an example of slicing, with the slices delineated in red. In the case of non-layer printing methods, such as FDM printing, a secondary post-process is required. This process, known as hatching, involves the separation of each slice into lines, a process analogous to the colouring of an image. In the majority of cases, the lines are either parallel or concentric, and they occupy the entire slice. This is illustrated in the centre of Figure 2.5 by the blue lines. The distance between two lines is referred to as the hatching distance. Furthermore, the hatching distance and direction can be varied over the 3D model, thereby generating hollow in-fills with the objective of reducing material and processing time. Furthermore, the hatching distance is subject to variation in accordance with the process parameters. To illustrate, in selective laser sintering, the hatching distance is dependent on the laser spot size. In the event that the 3D-printed component is to be entirely solid, it is necessary for the sintered lines to overlap. Accordingly, the hatching

distance must be selected in accordance with the dimensions of the laser spot. The final stage of the printing process is the actual printing procedure. Subsequently, the preprocessed code of the 3D model is fed into a 3D printer, which then interprets the sliced and hatched file and creates a set of instructions that it follows in the actual printing process. Subsequently, the printer executes the instructions and initiates the deposition of material through extrusion, laser sintering, or other techniques specific to the printing technology. This process is illustrated in the right portion of Figure 2.5. Typically, the printer commences at the base of the model and adds material in successive layers until the entire structure is complete.

2.2.2 Two-photon laser lithography

Two-photon laser lithography, also referred to as 3D micro-lithography, represents an additive microfabrication technique. The manufacturing process bears resemblance to the well-known stereo lithography technique. Both techniques employ light to initiate a localised photochemical reaction in a photosensitive polymer base, commonly referred to as a photo resin [74–76]. The aforementioned photochemical reactions typically result in the polymerisation of the base material, thereby hardening it. The photo-chemical reaction may also break the polymer chains and render the exposed areas more susceptible to solvation, depending on the type of photo resist. The first type of photo resin is typically employed in 3D printing processes and additive manufacturing, whereas the second type is commonly utilised in the fabrication of semiconductor components [77, 78]. This chapter will focus on the additive manufacturing of micro components and will therefore concentrate on the first type of photo resin.

The operational principle of a two-photon laser lithography device is illustrated in Figure 2.6. A near-infrared (IR) femtosecond laser with a wavelength of approximately 1080 nm provides a constant flux of photons. The laser beam is then focused through a microscope lens into a layer of photosensitive material, which is commonly referred to as a photo resin or photo resist. A single IR photon possesses insufficient energy to excite any of the molecules within the photo resist [79]. Only in the vicinity of the focal point of the microscope optics is the light intensity sufficiently high to permit the interaction of photons with the photosensitive material. The primary driving factor is the occurrence of two-photon absorption processes, which are most prevalent in areas of extreme intensity [76, 80, 81]. Two-photon absorption (TPA) is defined as the process of absorbing two photons of identical or different wavelengths, resulting in an excited state across a virtual energy level [82, 83]. In the absence of the combined action of the two photons, the excitation of the contributing photons would be prohibited by quantum mechanical principles. However, the simultaneous absorption of both photons enables exited electrons to reach an excited state higher in energy then the energy of the single

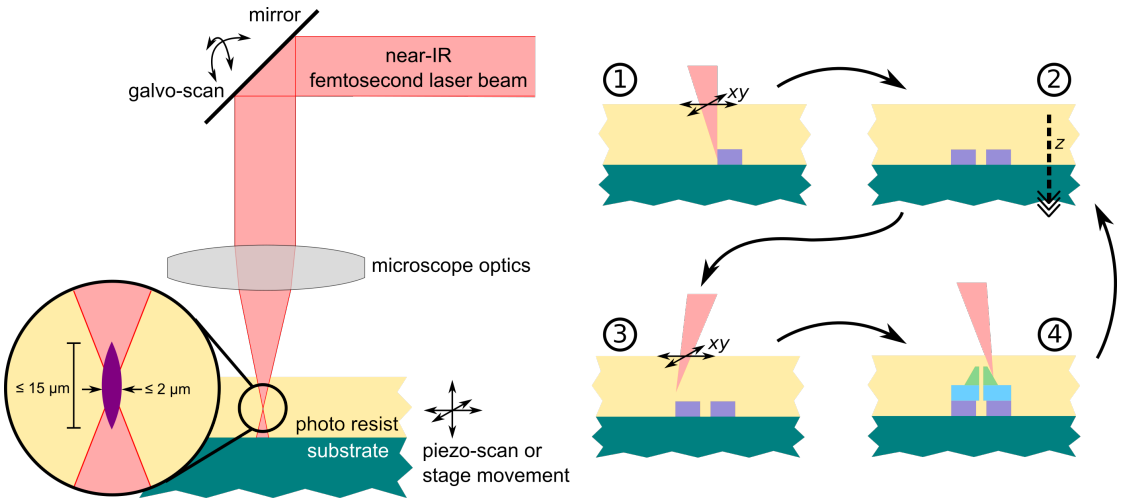

Figure 2.6: Schematic illustrating the operational principle of a two-photon laser lithography device. The illustration on the left demonstrates the method of achieving a localised exposure of a small volume of photo resist. A near-infrared laser is focused by a microscope lens. In the vicinity of the focal point of the optical system, a volume of considerable intensity is generated. In this volume, which is also referred to as a voxel, two-photon absorption processes occur with a high probability. The initiation of a photochemical reaction is only possible if two photons are absorbed by the photo resist. A three-dimensional structure can be created by moving the focused laser beam in all three dimensions within the photo resist. This can be achieved either by moving the substrate and the resist, or by changing the beam path via a mirror. The right-hand drawing provides a simplified overview of the printing process. Initially, the laser is focused in close proximity of the substrate (1), and subsequently, it is moved in the xy-plane, thereby exposing a thin layer (slice) of the 3D structure. Once the entire slice has been exposed and attached to the substrate, the latter is then moved downwards (2). This results in the voxel being elevated and separated from the preceding layer (3). Subsequently, a new slice is printed and attached to the previously printed one (4). These steps are repeated until the desired three-dimensional structure has been fully printed into the photo resist.

photon. Two-photon absorption is contingent upon the simultaneous absorption of two photons, and thus is proportional to the square of the light intensity. This indicates that TPA exhibits nonlinear behaviour. In contrast, single-photon absorption is a linear process and directly proportional to the light intensity [83]. The nonlinear behaviour of TPA in combination with the focused IR laser results in a highly localised exposure event around the focus of the microscope optics [80, 81]. This is shown in Figure 2.6 (left-hand), which shows a magnified view of the focal area of the laser. If one were to calculate the square of the light intensity in 3D around the focal area, the resulting shape would be an ellipsoid. Within this ellipsoidal structure, chemical processes may be initiated by TPA, resulting in the formation of a polymerised material that hardens the surrounding area. The ellipsoid is also referred to as a volumetric pixel or, in short, a voxel. The manipulation of the voxel allows for the exposure of 2D structures in a manner

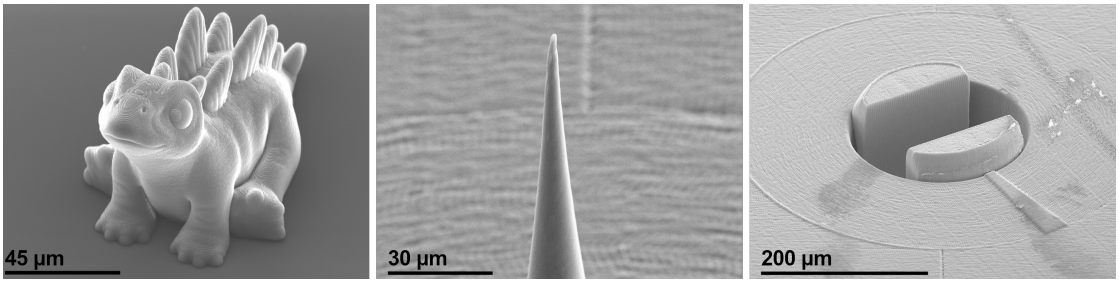

Figure 2.7: Images, captured using a scanning electron microscope, illustrating examples of three-dimensional micro-printed structures created by the utilisation of a two-photon laser lithography device. The image on the left depicts a dinosaur. This figurine serves to exemplify the potential for manufacturing objects with exceedingly high resolution and minute features. The image in the centre illustrates a micro needle. The sharp tip has a diameter of approximately 1.2 µm and the surface of the needle is characterised by a high degree of smoothness. A number of such needles were printed, and all were found to be identical. This illustrates the dependability of the process and the quality of the printed surface. The image on the right illustrates a mechanical micro connector. The presented connectors facilitate the mechanical connection of multiple 3D micro-printed components by the application of friction and spring forces. The presented example illustrates the mechanical functionality and strength of the polymer material.

analogous to the act of drawing a picture. The movement of the voxel can be achieved in two ways: either by moving the substrate via a mechanical stage or by changing the laser path via mirrors [74, 75, 78]. The size of the voxel is dependent on the microscope optics [84]. The larger the magnification, the tighter the focus of the laser beam, which in turn reduces the lateral dimensions of the exposed area. Consequently, higher magnifications facilitate the printing of more precise features [84]. Conversely, the reduction in voxel size results in a narrower hatching and slicing distance, increasing the processing time significantly.

By moving the voxel along a pattern generated by the process illustrated in Figure 2.5, a three-dimensional structure may be printed in photo resin [78]. This process is also illustrated on the right-hand of Figure 2.6. The printing process of a two-photon laser lithography device closely resembles that of a standard 3D printing process. Initially, a layer connected to the substrate is printed (1 in Figure 2.6). This layer provides structural support and prevents unwanted movement. Thereafter, additional layers are printed and attached to the subsequent layers (2-4 in Figure 2.6). Examples of micro-printed structures created using a two-photon lithography device are shown in Figure 2.7. Three scanning electron microscope images of micro-printed models are presented. These include functional components such as micro connectors, which facilitate the assembly of multiple parts into larger macro structures.

The two-photon laser lithography process can be configured in a number of ways, depending on the device and photo resin used. If the photo resin is in a solid state, the process is designated as "air gap printing" [84]. In this configuration, the lens is positioned above the solid resin, with the laser exiting the lens and re-entering the photo resin. This results in the occurrence of an additional diffraction process along the trajectory of the laser beam, which widens or deflects it [84]. Consequently, the maximum attainable resolution is diminished as the voxel widens. The advantage of a solid resin is that it provides structural support for the printed structures, thereby enabling free-float printing without the need for additional supports [78]. However, due to the solid nature of the material, the maximum height of the structures is limited by the layer thickness of the resin. In the event that a liquid resin is utilised during the printing process, the lens may be introduced into the resin droplet. This process is referred to as "dip-in lithography" [84]. By immersing the lens in the resin, the effect of diffraction is significantly reduced. Moreover, the liquid resins are designed to have a diffraction coefficient that is similar to that of glass, which further reduces diffraction at the interface between the lens and the resin [84]. In comparison to solid resins, liquid resins exhibit greater freedom in terms of structure height. As the droplet adheres to substrate and lens by capillary forces, the height is constrained only by the mechanical limitations of the device and the resin availability [84]. However, liquid resins offer less support than solid resins, necessitating the incorporation of additional structures to support free-floating models [84].

2.2.3 Applied resins and realised structures

The application of the print process to real emitter designs was conducted throughout the duration of this project. The emitter structures were fabricated using SU-8 resin and IP-Q as well as IPx-Q. The successful replication of structures with feature sizes in the single micron range was demonstrated using SU-8 resin, as illustrated in Figure 2.4.. SU-8 provides high-resolution printing for features ranging from single microns to more than 200 microns in lateral size [78]. Furthermore, the mechanical, vacuum and chemical stability of SU-8 are additional factors that contributed to its selection for utilisation in this project. The resolution of the printing process is not the limiting factor for SU-8-based structures; rather, it is the maximum achievable layer thickness of the resist that limits the vertical structure size. In addition, IP-Q and its derivative IPx-Q were employed throughout the course of this project. Both IP-Q and IPx-Q were developed for the printing of structures ranging from the meso to the macro scale, with feature sizes from 1 µm to 1000 µm. The resin was optimised for printing with a 10× magnification, which results in a minimal feature size of approximately 1 µm in lateral dimensions and 5 µm to 10 µm in vertical minimal feature size. By employing a high magnification,

such as 63×, it is possible to realise features in the sub-micrometre range. This is demonstrated in Figure 2.7, which illustrates examples of structures fabricated using the 63× and 10× objectives. In contrast to SU-8, IP resins lack a maximum layer height, thereby enabling the fabrication of structures up to 10 mm in height. Furthermore, the IP resins feature similar mechanical, vacuum and chemical stability compared to SU-8. A thin plate of 200 µm in thickness is more than stable enough to support a practical implementation of an electrospray emitter. The mechanical properties also allow for micro assemblies like those shown in Figure 2.7 Their physical properties and realisable feature sizes make the IP resins an ideal choice for this application.

2.3 Ionic liquids

Ionic liquids represent an intriguing class of materials. Their vast range of compositions and potential applications render them highly adaptable. However, before delving into the specifics of their prospective and actual applications, as well as the synthesis of ionic liquids, it is imperative to first define ionic liquids. One possible definition of ionic liquids is:

'Ionic liquids are liquids comprised entirely of ions' [85].

Although the fundamental parts of the definition of "liquid" and "ions" are widely accepted, there is considerable variation in the specific concepts that are included in these definitions. Some definitions include a temperature range, allow solvents to be mixed into the liquid, or define ionic liquids as molten salts [85–87]. The inclusion or exclusion of certain liquids in a given definition is dependent on the specific definition employed. In order to adopt a comprehensive approach to the subject matter, this study will adopt the definition of MacFarlane, as it offers a highly flexible perspective while maintaining the essential core concepts of liquid and ions. In accordance with the aforementioned definition, ionic liquids may be classified as molten salts, mixtures of diverse cations and anions, organic and inorganic compounds, or any other substance that is constituted solely of pure ions. Figure 2.8 illustrates an exemplar combination of anions and cations for an ionic liquid. The ionic liquid under discussion is 1-ethyl-3-methylimidazolium tetrafluoroborate, or EMI-$BF4_4$ for short. This liquid is commonly used for electrospray thrusters and has been demonstrated to be stable in space-like and space conditions [5, 88, 89].

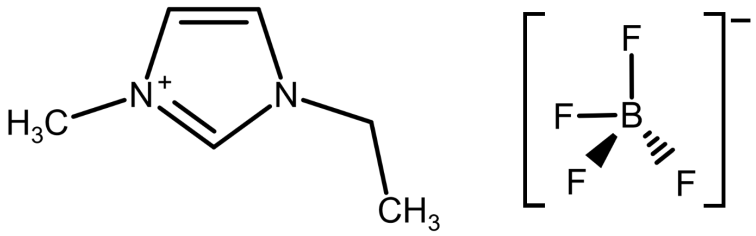

Figure 2.8: Natta projection of the ionic liquid 1-ethyl-3-methylimidazolium tetrafluoroborate, also referred to as EMI-BF_4. The molecule on the left represents the EMI cation. The organic ring structure, in which nitrogen atoms are substituted for carbon atoms, gives the resulting molecule a positive charge. The molecule on the right is the BF_4 anion. The negative charge is distributed over the four bonds, resulting in the formation of a negatively charged complex.

The vast number of possible ionic liquid combinations and mixtures yields a significant flexibility in their synthesis and characterisation. Only a modest proportion of the total number of calculated or simulated combinations has been synthesised to date, and an even smaller proportion has undergone comprehensive characterisation [85, 86]. A number of open access databases have been established with the aim of collating all available information about ionic liquids. One such database is the Ionic Liquids Database - ILThermo (v2.0). As of June 2024, the database contained only 3,041 ionic liquids, representing a mere fraction of the potential combinations [90]. To illustrate the malleability of ionic liquids, Figure 2.9 depicts the Natta projection of the ionic liquid 1-ethyl-3-methylimidazolium bis(trifluoromethylsulfonyl)imide, or EMI-Im for short. This ionic liquid shares the same EMI cation as the EMI-BF_4 ionic liquid depicted in Figure 2.8, but instead of the BF_4 anion, the Im (bis(trifluoromethylsulfonyl)imide) anion is employed. The replacement of the anions is associated with alterations in the physical and chemical characteristics of the liquid. For instance, EMI-BF_4 exhibits a yellowish hue, whereas EMI-Im is predominantly transparent. Additionally, EMI-Im displays a reduced viscosity and surface tension in comparison to EMI-BF_4. These observations illustrate the impact of anion exchange on the properties of ionic liquids.

Ionic liquids possess a distinctive liquid state and are constituted by pure ions, exhibiting intriguing physical and chemical properties. One such property is their markedly low vapour pressure, which is essentially negligible. This renders ionic liquids highly stable in vacuum and space conditions. Another notable attribute is their adjustable viscosity, which varies in accordance with the ions employed. The viscosity of a solution can be modified by exchanging one ion for a different type of

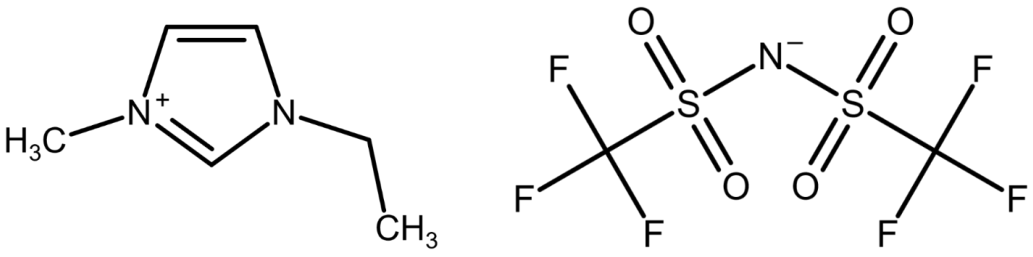

Figure 2.9: Natta projection of the ionic liquid 1-ethyl-3-methylimidazolium bis(trifluoromethylsulfonyl)imide, also known as EMI-Im. The left-hand molecule is identical to the EMI molecule present in the ionic liquid EMI-BF_4, as illustrated in Figure 2.8. In the case of EMI-Im, however, the anion bis(trifluoromethylsulfonyl)imide ($[N(SO_2CF_3)_2]^-$) *is used. In comparison to the* BF_4 *anion, the Im anion is considerably heavier while maintaining the same charge.*

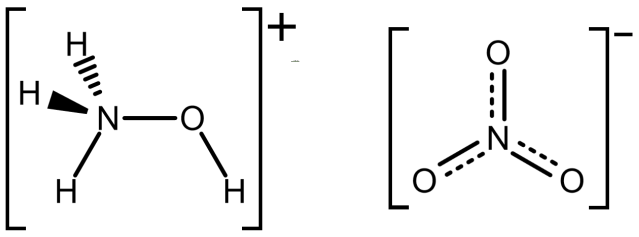

Figure 2.10: Natta projection of the ionic liquid hydroxylammonium nitrate ($[NH_3OH]^+[NO_3]^-$)*, better known as HAN. This ionic liquid has the potential to be utilised in chemical propulsion systems and electrospray thrusters [93]. When employed as a chemical propellant, HAN exhibits comparable or even enhanced performance relative to hydrazine, while retaining its suitability as an electrospray propellant. This paves the way for dual-propulsion solutions, which leverage the benefits of both propulsion systems with a single propellant.*

ion. This is a highly beneficial property, which is particularly advantageous in specific applications. Nevertheless, the synthesis of ionic liquids with extremely low viscosity remains a significant challenge, and is an area of ongoing research [85]. The potential of low viscosity ionic liquids for use in electrochemical devices such as batteries is an area of significant interest, given that a reduction in viscosity could lead to enhanced device performance. Furthermore, the viscosity of ionic liquids is subject to alteration upon the application of elevated temperatures, exhibiting a pronounced dependence on temperature [85, 91]. Furthermore, ionic liquids exhibit excellent electrochemical properties, including high ionic conductivity and robust electrochemical stability. This renders them optimal for utilisation as an electrolyte in batteries, capacitors, fuel cells and solar cells [85, 92]. Additionally, ionic liquids can be used in vacuum conditions due to their low vapour pressure, which makes them ideal for use in space flight. Their inherent conductivity allows them to serve as electrical bridges in ion thrusters without the need for prior ionisation, unlike neutral gases like xenon. This makes them an attractive option for this application, as the propellant typically needs to be ionised beforehand and has to exert a certain conductivity [5].

One of the most significant advantages of ionic liquids is their versatility. Ionic liquids are suitable for use in a multitude of applications in terrestrial and space environments [85, 86]. A few potential applications were previously outlined, including use as a battery component or fuel source for electrospray thrusters. However, this represents only a subset of the possible applications. In addition to the aforementioned applications, ionic liquids can also be employed as fuel for chemical propulsion systems, utilized in the bio-processing of human waste, incorporated into life support systems, utilized as vacuum-stable lubricants, and applied in material processing, among other potential applications [85, 86, 91–95]. In the context of this study, particular attention should be paid to a specific type

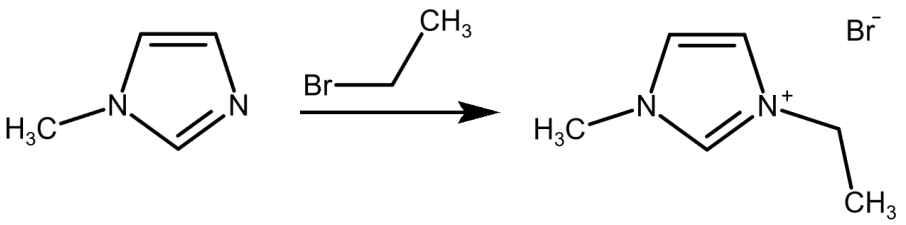

Figure 2.11: Synthesis of 1-ethyl-3-methylimidazolium bromide from 1-methylimidazole and 1-ethyl bromide. This reaction is an example for a quarternisation and results in the widely used 1-ethyl-3-methylimidazolium cation and in this case a bromide counter-ion.

of ionic liquid. Hypergolic ionic liquids constitute a distinctive subset of ionic liquids characterised by a high chemical energy density. The stored energy enables combustion with an oxidiser (bipropellant) or by catalytic decomposition (monopropellant). It can therefore be stated that these ionic liquids can be used as a chemical rocket fuel. A number of studies have demonstrated the considerable potential of hypergolic ionic liquids, which have been shown to exhibit comparable performance or even superior characteristics to established chemical propellants such as hydrazine [85, 86, 91, 93, 95, 96]. Figure 2.10 illustrates an example of a hypergolic ionic liquid, namely hydroxylammonium nitrate (HAN), which has a comparable composition to that of hydrazine. It can be employed as a monopropellant or bipropellant. Since HAN retains its properties as an ionic liquid due to the presence of positively and negatively charged complexes, it can still be used for electrospray propulsion [93, 97]. This enables the development of dual-propulsion systems that benefit from the advantages of both high-thrust chemical propulsion and high-efficiency electric propulsion. Furthermore, in comparison to hydrazine, ionic liquids are significantly more environmentally friendly and less hazardous to humans. This makes the handling of the propellant significantly more straightforward and allows for more thorough laboratory testing.

2.3.1 Synthesis of ionic liquids

The preceding sections have addressed the fundamental characteristics of ionic liquids and their potential applications. Nevertheless, the question of how such ionic liquids are synthesised remains unanswered. Ionic liquids can be synthesised from organic bases by quarternisation [91]. This process entails a reaction from a 3- to a 4-coordinate phosphorus or nitrogen. An illustrative example of such a reaction is the alkylation of 1-methylimidazole with 1-ethyl bromide, which results in the formation of a 1-ethyl-3-methylimidazolium cation and a bromide counter-ion. Figure 2.11 illustrates the synthesis reaction for 1-ethyl-3-methylimidazolium bromide. The reaction is conducted in the presence of a solvent, which enhances the yield. Acetonitrile is a solvent frequently employed for this reaction [91]. The

cation 1-ethyl-3-methylimidazolium is identical to that present in Figure 2.8 and Figure 2.9 and is a prevalent component in numerous ILs. Following the initial chemical reaction, a series of cleansing procedures are undertaken with the objective of removing any residual impurities. Additionally, the solvent is removed during this process. Moreover, the counter-ion, which is a byproduct of the quaternization process, is not always the desired product. To illustrate, the ionic liquid EMI-Im employs the same cation but a distinct anion. Consequently, an anion exchange may be conducted to produce the desired ionic liquid [86, 91]. The precise mechanism and potential reactions involved in the exchange of the anion can be highly intricate and are beyond the scope of this study. Further insights on this subject can be found in the referenced literature [86, 91].

2.3.2 Ionic liquids for electrospray thrusters

As previously outlined, a plethora of potential ionic liquids exist for utilisation in electrospray propulsion systems. The most commonly employed ionic liquids are EMI-BF_4 and EMI-Im [5, 46, 62, 88]. Both ionic liquids are distinguished by their high vacuum stability, high conductivity, and relatively low viscosity. Additionally, both utilise the same and highly prevalent EMI cation, which ensures the liquids are readily available in large quantities. Their physical properties, when considered alongside their high performance in electrospray applications, render them optimal candidates for use as thruster propellants. Based on the extensive experience of other research groups with these liquids, EMI-BF_4 and EMI-Im were also selected for this project. While both were employed during this project, EMI-Im has demonstrated a more benign application profile for this project. The surface tension of EMI-Im is slightly lower than that of EMI-BF_4, which renders it less susceptible to the formation of bubbles and foam. Recently, research has been conducted into alternative liquids that may be able to substitute for EMI-BF_4 and EMI-Im in the future. A suitable candidate is EMI-$FeCl_4$ a metal halide. EMI-$FeCl_4$ shows higher emission current than EMI-BF_4 and has higher ion masses, which results in better thruster performance. In this regard, it is possible that a more suitable ionic liquid may be identified in the future [98].

Chapter 3

Results (Publications)

A total of seven publications was produced over the course of this project. These publications comprise two journal articles and five conference papers. Of the latter, four were deemed to be of particular interest and are included in this chapter. The final conference paper was moved to the Appendix due to its overlap with the first journal article.
All publications included in this chapter and added to the Appendix are:

- Publication I: AIP Advances 2021
- Publication II: Space Propulsion Conference 2022
- Publication III: International Electric Propulsion Conference 2022
- Publication IV: Journal of Electric Propulsion 2024
- Publication V: Space Propulsion Conference 2024
- Publication VI: International Electric Propulsion Conference 2024
- Additional Publication A1: Rus. Ger. Conf. on Electric Prop. 2021

A more detailed overview of the publications and their respective contents can be found in the table on the following page. Additionally, the table includes a set of keywords for each publication. Each keyword is associated with a specific topic addressed in the publication, which correspond to the topics outlined in Chapter 2.

List of Publications

#	Type	Emitter geometries	Scale	Resin	Propellant	Electrode
I	Journal	straight capillaries, single emitters, small arrays	10 µm capillaries	SU-8	EMI-BF_4	external
II	Conf.	straight capillaries, small arrays	10 µm capillaries	SU-8	EMI-BF_4	external
III	Conf.	straight capillaries, large arrays	10 µm capillaries	SU-8	EMI-BF_4	external
IV	Journal	tapered, square and straight capillaries, single emitters, small arrays	10 µm to 100 µm capillaries	IP-Q	EMI-BF_4	integrated
V	Conf.	spiral capillaries, ext. wet. emitters, single emitters	5 µm needles 50 µm capillaries	IP-Q	EMI-Im	integrated
VI	Conf.	spiral and tapered capillaries, ext. wet. emitters, single emitters	60 µm to 300 µm tapered capillaries	IP-Q, IPx-Q	EMI-Im	integrated
A1	Conf.	straight capillaries, single emitters, small arrays	8 µm to 20 µm capillaries	SU-8	n.a.	n.a.

Characterisation	Emission	Additional keywords
SEM/optical imaging, emission current	single events	cross section view, focused ion beam
SEM imaging, emission current	unstable, short period	radiation hardness
SEM imaging, time of flight	unstable, short period	Bradbury-Nielson ion gate, ion trajectory simulations
SEM/optical imaging, video observation, emission current	unstable, semi stable, short period	self aligning micro assembly, in-situ optical imaging
video observation, emission current	semi stable, short period	improved micro assembly external emitter emission
optical imaging, video observation, emission current	semi stable, long period, periodic/alternating	in-situ optical imaging Taylor-Cone emission video
SEM/optical imaging,	n.a.	cross section view, focused ion beam/milling

3.1 Publication I: AIP Advances

This publication marks the inaugural publication in a series of works focused on the fabrication of miniaturised electrospray emitters. This represents the initial transition from the previously employed 2.5D planar stacking fabrication methodology to the utilisation of true 3D printing techniques. The successful application of 3D printing to these microstructures has enabled the fabrication of electrospray emitters with capillary diameters of less than 10 µm and heights of more than 200 µm. The fabrication of emitters at this scale with an aspect ratio of more than 20 represents a significant advancement. Moreover, the suitability of the SU-8 polymer for this particular application and its compatibility with the micro printing process were demonstrated. Furthermore, this publication validated the manufacturing process for array fabrication. Demonstrating the reproducibility of the printing process represented a significant achievement for this fabrication method. Arrays comprising upwards of 25 individual emitters were successfully manufactured, with minimal instances of fabrication-related errors. In addition to the aforementioned fabrication milestone, a considerable effort was made to enhance the experimental characterisation setup. The utilisation of a high-precision syringe pump enhanced the characterisation capabilities and facilitated more rigorous experimentation with the manufactured emitters.

F. Kunze wrote the first draft of the manuscript. The manuscript underwent revision by all of the contributing authors. The experiments and data acquisition were conducted by F. Kunze. Furthermore, P. Klar and T. Henning provided supervisory and project management oversight.

AIP Advances ARTICLE scitation.org/journal/adv

Taking internally wetted capillary electrospray emitters to the sub-ten-micrometer scale with 3D microlithography

Cite as: AIP Advances 11, 105315 (2021); doi: 10.1063/5.0066619
Submitted: 6 September 2021 • Accepted: 20 September 2021 •
Published Online: 8 October 2021

Fynn L. Kunze,[a] Torsten Henning, and Peter J. Klar

AFFILIATIONS

Institute of Experimental Physics I and Center for Materials Research ZfM/LaMa, Justus Liebig University, Heinrich-Buff-Ring 16, DE-35392 Giessen, Germany

[a]Author to whom correspondence should be addressed: Fynn.Kunze@physik.uni-giessen.de

ABSTRACT

Electrospray emitters are an obvious choice for miniaturized thrusters for a variety of applications on small satellites (e. g., CubeSats), as well as for other micropropulsion purposes. They are inherently small and require a relatively low electric power for operation, and therefore, they fulfill the requirements imposed due to the small volume of CubeSats. Electrospray emitters of the internally wetted capillary type were fabricated by 3D microlithography in the SU-8 photopolymer down to capillary diameters of about 10 μm. Thus, the emitters are an order of magnitude smaller in lateral dimensions than those fabricated by advanced 3D printing methods and still half an order of magnitude smaller than those made by planar photolithography in SU-8. Fabrication methods and process parameters are presented. Furthermore, the preliminary results of the electric characterization of the emission behavior are shown. The experiments show promising results regarding the fabrication quality and extraction behavior.

I. INTRODUCTION AND MOTIVATION

In recent years, small satellites have become more and more important for both commercial and scientific purposes.[1–3] Alongside the demand for small satellites, the need for specialized micropropulsion systems arises. Specifically, electric propulsion systems have become more important due to their high efficiency and high specific impulse, resulting in good fuel and power economy, for purposes such as attitude and orbit control (AOC).[4–8]

There are two ways to develop miniaturized electric thruster systems for small satellites. The first is to scale down established thrusters, such as plasma-based propulsion systems, while the second is to develop systems from inherently small components. Electrospray emitters fall under the second approach to miniaturization, as they are inherently small and well suited for small satellites due to their low power requirements.[9]

These emitters utilize a static electric field applied between a liquid ion source (LIS) and an extraction electrode to extract droplets or, ideally, single ions from the LIS. The liquid propellant is supplied to an extraction site on the emitter surface, typically an orifice, where the liquid is exposed to the electric field. Under the influence of the (external) electric forces and the internal forces (cohesion) of the liquid, its meniscus is deformed, resulting in a cone-like shape, the so-called "Taylor cone."[10] At the tip of the cone, the electric forces are stronger than the internal hydraulic forces, thus allowing droplets or single ions to overcome the surface tension and form an ion spray, the so-called electrospray. The extracted ions can be further accelerated with suitable ion optics to generate thrust for small spacecraft.[11–13]

There are three basic emitter configuration types, namely, externally wetted emitters, porous emitters, and internally wetted capillary emitters that this paper focuses on. The three of them differ in the way the propellant is supplied to the extraction sites, while all three from there on follow the same operating principle described above.[14]

The hydraulic resistance of the propellant feed system has been identified as a key parameter for stable operation of the emitters.[15] A sufficiently high hydraulic resistance can only be achieved by the fabrication of structures with a high aspect ratio (length-to-diameter ratio), which is a difficult task in any field of microfabrication.

Porous emitters have an advantage in this respect because the fluidic path through the pores provides a high hydraulic resistance at the expense of introducing an element of randomness into the design and of imposing a lower size limit on the miniaturization of the individual emitter.

Porous emitters with liquid metal as a propellant (field emission electric propulsion or FEEP thrusters) are already in use on spacecraft and have flight heritage;[16,17] however, with the recent advances in microfabrication technologies, both in 3D printing and in silicon technologies, internally wetted capillary emitters appear to have become viable for thruster applications again. 3D printing techniques, such as vat printing [stereo-lithography apparatus/digital light processing (SLA/DLP) printing], and, for smaller critical lateral dimensions, two-photon laser lithography are new fabrication technologies that offer a high degree of freedom of design for electrospray emitters[18,19] and thus the possibility of re-addressing the subject of hydraulic resistance in miniaturized emitters. Moreover, the capability of 3D microlithography to create capillaries with diameters as small as single digit micrometer figures implies that emitters thus created are at least an order of magnitude smaller in lateral dimensions than internally wetted capillary type microemitters made by other advanced 3D printing methods reported in the literature and still about half an order of magnitude smaller than the emitters fabricated in SU-8 by planar lithography previously reported by the authors.[11,20,21]

The research aim of the authors is to create single internally wetted capillary microemitters with a footprint of less than 0.1×0.1 mm^2 and a well-defined (that is, involving no elements of randomness) geometry at the sub-micrometer level, with capillary diameters of 10 μm and below, that is, at a scale which roughly equals the typical pore size of porous emitters.

From such individual microemitters, arrays of suitable sizes should be possible to build in order to achieve the required thrust range for a given application ("scaling-up by numbering-up"). The propellant of choice is an ionic liquid, namely, EMIM-BF4, for the time being. EMIM-BF4 is an ionic liquid often used for space applications. Technically, an ionic liquid is a salt with a very low melting point. Thus, it retains a liquid state at room temperature and below. Ionic liquids feature multiple advantages for space applications, such as negligible vapor pressure in vacuum environments, a high conductivity, and pre-ionization. EMIM-BF4 is composed of two molecules of similar molecular weight and opposite charges. EMIM (1-ethyl-3-methylimidazolium) is an organic molecule featuring a ring structure and a positive charge. BF4 (tetrafluoroborate) is an inorganic ion with a negative charge. Should the need arise, there are many different kinds of ionic liquids available, which would allow one to choose a suitable substitute for EMIM-BF4.[12,22]

II. MATERIALS AND METHODS

A. Fabrication methods and parameters

The fabrication method of choice for the essential parts of the microemitters is 3D microlithography in the form of two-photon lithography, realized in the commercial fabrication tool Photonic Professional GT (PPGT) from Nanoscribe (nanoscribe.com). The operating principle of the Nanoscribe PPGT is illustrated in Fig. 1. Light from a near-infrared fiber laser is focused through microscope optics. The single near-infrared photon does not carry enough

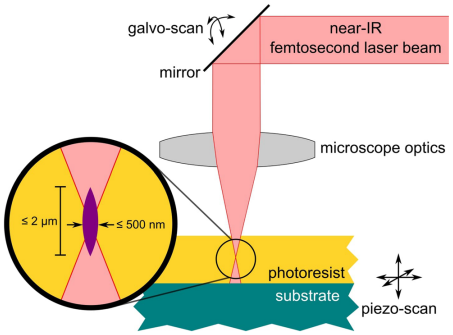

FIG. 1. Operating principle of two-photon lithography.

energy to trigger the photochemical reaction in the resist. However, in a small volume element (voxel) around the focus, the intensity is so high that two-photon processes occur. Two photons combined possess enough energy to start the photochemical reaction. The voxel typically has an extension of ~2 μm in the vertical direction and of less than the laser wavelength in lateral dimensions. By scanning this voxel through the resist, almost arbitrary shapes can be written. There are two scanning modes, namely, galvo scan, in which the laser beam is moved by galvo mirrors in the beam path, and piezo scan, in which the piezo stage carrying the sample is moved. Scanning in the vertical direction is always done in the piezo mode. Galvo scan offers an advantage in higher writing speed of about two orders of magnitude compared to piezo scan.

While there are resists optimized for use with the Nanoscribe PPGT, the authors opted to continue the use of SU-8 as a negative tone photostructurable epoxy polymer. Despite its most challenging properties for successful microfabrication, that is, the internal stress to which swelling during development is an important contribution, SU-8's superior resistance against harsh environments makes it a proven material for microfluidic applications.[23] One of the major beneficial properties of SU-8 is its chemical inertness. It is resistant to prolonged exposure to ionic liquids. Furthermore, currently, experiments under space-like conditions are conducted to verify if SU-8 is a suitable material for this application. SU-8 has a long heritage in high aspect ratio microlithography, and there is considerable knowledge regarding the optimization of the microlithography processes.[24]

3D lithography offers the possibility of creating undercut structures, which will become more important once the integration of the extraction electrodes or even more complex ion optics are considered.[25] At the present stage, the main objective of fabrication is to create well-defined single emitters with capillaries with a diameter as small as possible, integrated with a base plate with an edge length of a few millimeters that allows the handling of the emitter structure in the characterization setup. Mechanical stability and minimum warping of the base plate is a design target that needs to be

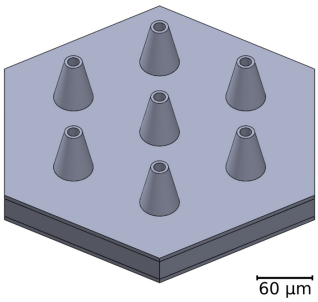

FIG. 2. 3D rendering of a CAD file defining an emitter array featuring seven individual volcano emitters and (a part of the) base plate.

traded-off against the requirement to keep writing times within reasonable bounds.

The basic shape of an individual emitter is that of a volcano.[26] One of the most important functions of the volcano shape is the mitigation of wetting of the area around the orifice by the ionic liquid.[20,21] Another benefit is the extension of the capillary's length and hence the hydraulic resistance without unduly extending the writing time. In addition, the volcano shape allows a good control of the electric field around the orifice and a strong enhancement of the electric field at that point. Figure 2 shows the CAD rendering of a small array of seven volcano microemitters on a base plate.

The volcano shape is not unique to emitters manufactured by two-photon lithography. Devices with lateral dimensions on the order of hundreds of micrometers made by 3D printing methods have been reported.[18,19]

The Nanoscribe PPGT works by writing lines. Areas are written by placing lines closed to each other (hatching). The optimum distance between lines (hatching distance) has to be determined by trading off the quality of writing against the writing time. Whether two neighboring hatching lines are written in the same direction or in opposite directions has been found to play no significant role in the projects presented here.

In the vertical (z) direction, subsequent layers are written at a fixed distance (slicing). As in hatching, the optimum slicing distance has to be determined as a compromise between the writing quality and time required. Since the structures to be written are larger than the areas that the galvo scan can cover in a single run, they have to be stitched together from the so-called chunks whose shape and arrangement are also subject to optimization. Careful chunking is critical for keeping the base plate warp as low as possible. Large volumes do not have to be written in their entirety. It is usually sufficient to write the outer surfaces and a number of support structures inside the volume. This technique is called "shell and scaffolding."

There are several routes to the set of line coordinates that are finally processed by the Nanoscribe PPGT:

- Sets of line coordinates can be produced by an external program and transferred as ASCII files.
- Lines can be algorithmically defined in the Nanoscribe-specific programming language (GWL files) that is interpreted by the NanoWrite software delivered with the instrument.
- The NanoWrite software can import standard 3D lithography CAD files, notably in the widespread STL format.

The latter approach is the most convenient one at the start of a project, and there are a number of options to control the behavior of the system in hatching, slicing, and chunking, but the control is nevertheless limited. Writing the GWL code allows for easy systematic variations of parameters and gives detailed control of the writing parameters for the most critical structures. Using an external programming language usually implies the generation of very large files that are inconvenient when rendering a visualization. In practice, a mix-and-match approach between CAD and import of STL files on the one hand and dedicated GWL code for the critical structures on the other hand has proven to be both convenient and economical. The typical process, design parameters for the volcano emitters, and writing parameters for the Nanoscribe PPGT system are listed in Table I.

The SU-8 resist (SU-8 50 from microchemicals.com) is spin-coated on a silicon wafer and pre-exposure-baked according to the manufacturer's specifications. To ensure good adhesion of the SU-8 to the wafer, an oxygen plasma cleaning of the wafer immediately before the coating is recommendable. When plasma cleaning is not available, a hydrofluoric acid dip of the wafer can be used instead.

When emitters are created by planar lithography, the silicon wafer acts as a sacrificial substrate, that is, it is removed at the end

TABLE I. Design parameters and process parameters for the fabrication of volcano emitters with the Nanoscribe PPGT 3D microlithography system.

Parameter	Value
Si wafer orientation	1-0-0
SU-8 resist thickness	≈130 μm
Surface offset	15 μm
Slicing distance	0.3 μm
Hatching distance	0.3 μm
Scanning speed, areas	100 000 μm s^{-1}
Scanning speed, details	50 000 μm s^{-1}
Relative laser power	35%
Base plate shape	Hexagonal
Base plate lateral size	5 × 5 mm^2
Base plate height	35 μm
Emitter height (height over base plate)	50 μm
Emitter diameter at base plate	(20 . . . 40) μm
Emitter diameter at top	(15 . . . 20) μm
Capillary diameter	(8 . . . 20) μm
Chunk shape	Honeycomb/hexagonal
Chunk side length	180 μm
Exposure time	≈12 h per complete unit
Post-exposure bake 65/95 °C	1/10 min
Development time	≈15 min

of the processing chain by wet chemical etching in warm potassium hydroxide solution. In this case, it is important that the wafer's surface orientation is 1-0-0, since a surface with that orientation can be attacked by the etchant.

In 3D microlithography with the resists optimized for this purpose, it is important to have a good contact between the written structure and the substrate. The writing process is therefore started at a certain distance below the substrate's surface as detected by the Nanoscribe system. This (negative) distance is known as the interface position. SU-8, however, turns out to be so viscous when processed as described above that the writing can actually be carried out entirely within the resist film at a fixed (surface) offset from the interface position. This implies that in the development step, the written structures are automatically detached from the substrate and that the wafer does no longer have to be dissolved. The wafer's surface orientation is then no longer important.

The post-exposure bake consists of two steps, first a hot plate bake for 60 s at 65 °C, then another bake for 10 min at 95 °C on a second hot plate. The samples are then developed in mr-Dev 600 (from www.microresist.de). Several developer baths may be used in series to minimize the risk of residues. Optionally, the development can be sped up by placing the beaker with the developer in a water bath with low power ultrasonic excitation. With the assistance of ultrasound, typical development times are on the order of 15 min. If "shell and scaffold" writing has been used, a flood exposure step has to be inserted in order to start the crosslinking of any resist remaining inside the shells. Flood exposure was carried out in a SUSS MA-56 mask aligner with a mercury high pressure vapor lamp (fly's eye not removed) and an exposure time of 10 s.

B. Characterization of the emission behavior

The experimental setup for the electrical characterization (both time-resolved and DC) is shown in Fig. 3. The emitter structures are glued to a PEEK holder with a two-component epoxy glue. At this stage, the quality of the glue connection and the continuity of the capillary are checked by filling the holder with deionized water and confirming under a microscope that a droplet occurs at the volcano tip only. Once the emitter has passed the quality check, the holder is mounted inside the vacuum chamber and connected to the propellant feed system. The propellant feed rate is controlled by a high precision infuse-withdrawal syringe pump (type KDS 900 OEM from www.kdscientific.com) with a mounted 25 μl syringe controlled by a computer. The ionic liquid is put at a high electric potential, whereas the annular shaped extraction electrode and the collector plate are grounded. The ion current impinging on the collector plate is passing a custom-built amplifier circuit whose output can be captured by digital multimeters for DC measurements and with an oscilloscope for time-resolved measurements. The cut-off frequency of the amplifier circuit is ~2 kHz due to the filter used. The custom-made electronics have the capability to resolve currents in the single nA range. No axial data can be acquired, such as the beam shape or the impact position on the detector plate, as the detector only features one collector plate.

III. RESULTS

A. Imaging of the emitter structures

The emitters fabricated as described above were characterized by scanning electron microscopy (SEM) and, in a destructive way, by milling with a focused ion beam (FIB) followed by SEM

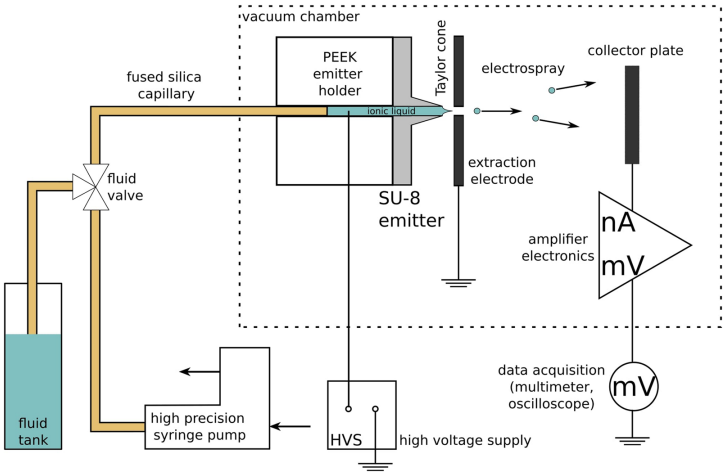

FIG. 3. Measurement setup for the characterization of the emission behavior.

inspection. Figure 4 shows two SEM images of a volcano emitter, taken at a slightly oblique angle from the top side (left panel) and from the back side (right panel).

The emitter has a height of 50 μm above the base plate whose thickness is 35 μm, and diameters of 35 and 16 μm at the base plate level and top, respectively. The actual capillary diameter is 10 μm, while the design diameter was 12 μm, which indicates that the voxel width in the lateral direction was about 1 μm. This emitter test structure was written on a single hexagonal chunk whose edges are visible at the right-hand side of the image in the left panel. The high surface quality of the SU-8 structures is obvious from the SEM image. The line extending from the cone at the center to the right results from scan lines starting and ending here. It can be neglected as the defect only affects the surface, with a height/depth in the nanometer range, thus not influencing the structural stability; it nevertheless could be avoided by redesigning the code for this part of the base plate, namely, by having the lines start and end at different, possibly random, angular positions. The SEM image taken from the back side in the right-hand panel of Fig. 4 shows that the diameter at the lower end of the capillary is the same as that at the top and that the capillary surface has the same high quality there; this is where the capabilities of SEM inspection end as far as the capillary is concerned.

The quality and reproducibility of 3D microlithography in SU-8 are also demonstrated by the SEM image in Fig. 5, which depicts a five by five array of volcano emitters with a height of 50 μm above the base plate each, arranged on a square lattice with 40 μm pitch.

Removing unexposed resist from the whole length of the capillary is a well-known challenge even in 3D printing on a larger scale.[18,19] While a continuity check at the end of the fabrication process can confirm that there is a fluidic path through the capillary, the homogeneity of the capillary diameter and quality can only be confirmed by destructive testing. Figure 6 shows the top of a volcano emitter (left panel) and a volcano emitter at the height of the base plate top (right-hand panel), respectively, both milled laterally by a focused ion beam (FIB) to about the center of the capillary.

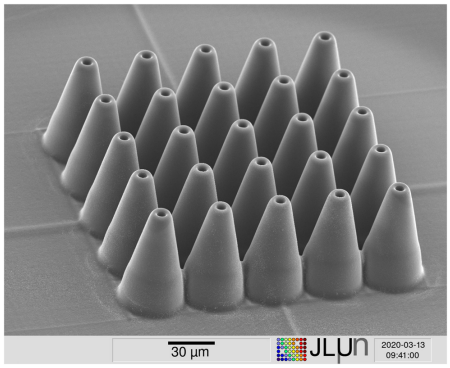

FIG. 5. SEM image of a five by five emitter array.

The FIB inspection shows no signs of incomplete development inside the capillary and suggests that the quality of writing is consistent throughout the entire capillary's length. It is obviously safe to state that capillaries with 10 μm diameter can be reliably fabricated; reducing the diameter further will be the subject of ongoing process optimization.

B. Electric characterization of the emission behavior

Time-resolved current signals from an array of seven microemitters are shown in Fig. 7. The propellant flow rate was kept at a low level, namely, at 0.05 μl min^{-1} for the measurement shown in the top panel and 0.1 μl min^{-1} for the bottom panel, respectively. The data were taken with an oscilloscope (top) and a digital multimeter (bottom). In both cases, the ionic liquid was put at negative

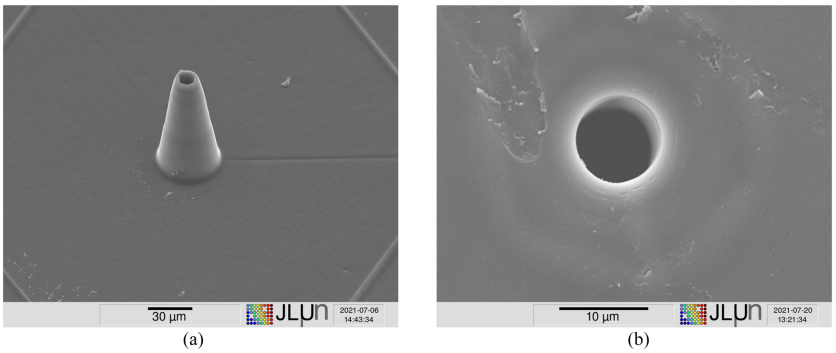

(a) (b)

FIG. 4. SEM images of a single volcano emitter from the (left) top and (right) bottom side.

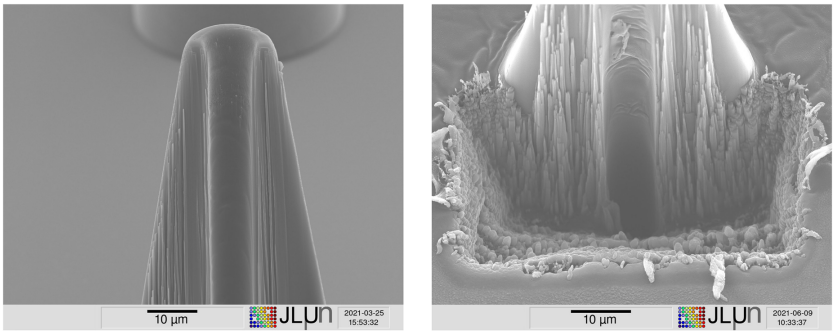

(a) (b)

FIG. 6. SEM images of an FIB milled volcano emitter at the tip (left) and at the base plate height (right).

potentials of 2–2.5 kV, and the annular ring extraction electrode with an inner diameter of 1.5 mm and an outer diameter of 3.5 mm was placed at a distance of ~2 mm from the emitters. A caveat at this time is that the geometry of the emission characteristics is not well-known, and it cannot be ruled out that significant portions of the emitted ionic liquid end up on other parts of the (grounded) chamber than the collector plate.

In the low flow regime that data are available for at this time, the emission obviously occurs in the form of single peaks, most likely resulting from rather large droplets that are emitted from one or several of the seven microemitters in the array.

The capillary cross sections realized here with 3D microlithography are more than an order of magnitude lower than those realized by planar and stacked planar photolithography reported earlier by the authors.[11]

Consequently, the currents are comparatively small, and very likely pulsed as there was no stable emission. The experiments revealed that the time resolution of the DC voltmeter (~800 ms) is insufficient to resolve such small pulsed currents. The resolution is primarily limited by the communication with the PC. We were able to resolve such currents on these time scales with the oscilloscope, but it was not possible to record the corresponding data, as the writing speed was too low. Therefore, only single events could be resolved. A ToF setup with improved accuracy is in progress at this time. The new setup features a multi-channel-plate detector, able to resolve even single ion events, with a time resolution in the

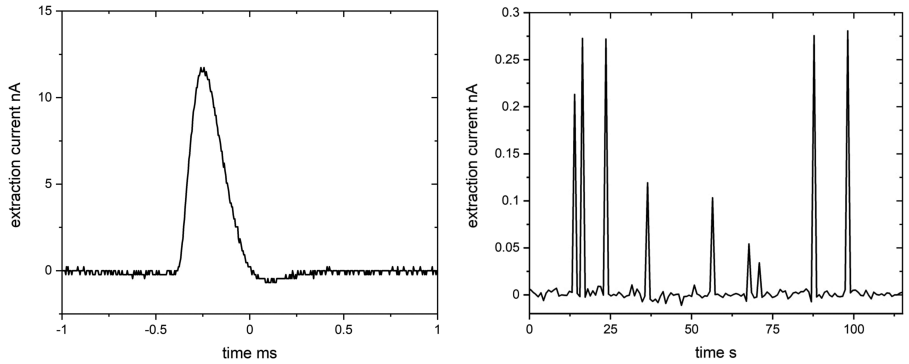

FIG. 7. Extraction current as a function of time for a seven microemitter array: on a short time scale, taken with an oscilloscope (top panel), on a longer time scale, taken with a digital multimeter (bottom panel).

nanosecond range. The detector also features a delay line function giving us access to an axial resolution, revealing the beam spread. Using this new detector, ToF data become available and velocity and mass distributions of the extracted charged species may be determined. We anticipate significant improvement in the beam characterization of our miniaturized emitters using the new equipment.

The emission regimes attainable with the high precision syringe pump controlled flow rate remain to be mapped for the microemitters with 10 μm capillary diameter. In particular, it will be interesting to see how the transition from individual droplets to a continuous emission will be affected by the small capillary diameters, and if individual microemitters arranged in an array indeed are operating independently from each other.

IV. CONCLUSION

The microemitters that are the subject of this report were for the first time made entirely with 3D microlithography, that is, without substrates pre-fabricated with planar photolithography. 3D microlithography is thus proven to be a suitable tool for microemitter fabrication, and the output of more than one finished (ready for measurement) structure per day shows that the Nanoscribe PPGT may even be suitable as a production tool for small series rather than just as a research tool. The overall production cost per unit is lower compared to other fabrication methods, as one unit only requires some readily available photo epoxy, given the necessary infrastructure is available. Furthermore, a rapid prototyping cycle makes this fabrication method rather interesting for commercial and scientific applications.

Currently, there are few other fabrication methods capable of producing emitters of the same quality and size. An example capable of doing so is a silicon-based fabrication method with deep reactive ion etching at its core.[25] Compared to our fabrication method, deep reactive ion etching is incapable of producing undercut profiles and is harshly limited in its freedom of design. Furthermore, this fabrication technique lacks the high resolution of 3D lithography for very small details and has longer production and prototyping cycles.

The newly won design freedom will allow the creation of fluidic structures with increased hydraulic resistance in a well-defined way, which would justify extending the research on miniaturized electrospray emitters to the internally wetted capillary type as an alternative to the successfully established porous emitter type, offering the prospect of further miniaturization by at least one order of magnitude.

The flow regimes across the multiparameter space spanned by flow rate, capillary dimensions, and extraction voltage, to name the most important, need to be mapped both for single emitters and for emitter arrays. Finally, to characterize the composition of the emitted species, an improved ToF setup tailored to the low signal levels needs to be established. Under these circumstances, internally wetted capillary electrospray microemitters still have the potential to become a useful tool in the arsenal of micropropulsion alongside the established porous emitters.

ACKNOWLEDGMENTS

The authors gratefully acknowledge funding by the federal state of Hessen and the European Regional Development Fund (ERDF/EFRE 2014–2 020) (Vorhaben: "Innovationslabor: Physik unter harschen Bedingungen" FKZ: FPG991 0002/2 019). The time-of-flight setup with improved resolution will be funded by the German Federal Ministry for Economic Affairs and Energy under Contract No. (FKZ) 50RS2101.

NOMENCLATURE

The following abbreviations are used in this manuscript:

AOC	attitude and orbit control
DLP	digital light processing
EMIM-BF4	1-ethyl-3-methylimidazolium tetrafluoroborate
FEEP	field emission electric propulsion
FIB	focused ion beam
GWL	NanoScribe specific file format
HVS	high voltage source
IR	infrared
LIS	liquid ion source
PEEK	polyether-ether-ketone
PPGT	type of NanoScribe instrument
SEM	scanning electron microscope or microscopy
SLA	stereo-lithography apparatus

AUTHOR DECLARATIONS

Conflict of Interest

The authors have no conflicts to disclose.

DATA AVAILABILITY

The data that support the findings of this study are openly available in Justus Liebig University's open access data portal JLUpubat at http://dx.doi.org/10.22029/jlupub-117.[27]

REFERENCES

[1] D. R. Lev, G. D. Emsellem, and A. K. Hallock, "The rise of the electric age for satellite propulsion," New Space **5**, 4–14 (2017).
[2] D. Lev, R. M. Myers, K. M. Lemmer, J. Kolbeck, H. Koizumi, and K. Polzin, "The technological and commercial expansion of electric propulsion," Acta Astronaut. **159**, 213–227 (2019).
[3] S. Mazouffre, "Electric propulsion for satellites and spacecraft: Established technologies and novel approaches," Plasma Sources Sci. Technol. **25**, 033002 (2016).
[4] K. Lemmer, "Propulsion for CubeSats," Acta Astronaut. **134**, 231–243 (2017).
[5] K. Holste, P. Dietz, S. Scharmann, K. Keil, T. Henning, D. Zschätzsch, M. Reitemeyer, B. Nauschütt, F. Kiefer, F. Kunze, J. Zorn, C. Heiliger, N. Joshi, U. Probst, R. Thüringer, C. Volkmar, D. Packan, S. Peterschmitt, K.-T. Brinkmann, H.-G. Zaunick, M. H. Thoma, M. Kretschmer, H. J. Leiter, S. Schippers, K. Hannemann, and P. J. Klar, "Ion thrusters for electric propulsion: Scientific issues developing a niche technology into a game changer," Rev. Sci. Instrum. **91**, 061101 (2020).
[6] I. Levchenko, S. Xu, S. Mazouffre, D. Lev, D. Pedrini, D. Goebel, L. Garrigues, F. Taccogna, and K. Bazaka, "Perspectives, frontiers, and new horizons for plasma-based space electric propulsion," Phys. Plasmas **27**, 020601 (2020).
[7] I. Levchenko, S. Xu, Y.-L. Wu, and K. Bazaka, "Hopes and concerns for astronomy of satellite constellations," Nat. Astron. **4**, 1012–1014 (2020).
[8] D. Krejci and P. Lozano, "Space propulsion technology for small spacecraft," Proc. IEEE **106**, 362–378 (2018).

[9]J. Mueller, "Thruster options for microspacecraft—A review and evaluation of existing hardware and emerging technologies," AIAA Paper No. 97-3058, 1997.
[10]G. I. Taylor, "Disintegration of water drops in an electric field," Proc. R. Soc. London, Ser. A **280**, 383–397 (1964).
[11]T. Henning, K. Huhn, and P. J. Klar, "Characterisation of electrospray microemitters fabricated by planar and 3D photolithography," in 36th International Electric Propulsion Conference, IEPC-2019-2344, Vienna, 2019.
[12]B. D. Prince, B. A. Fritz, and Y.-H. Chiu, "Ionic liquids in electrospray propulsion systems," in *Ionic Liquids: Science and Applications* (ACS Publications, 2012), Chap. 2, pp. 27–49.
[13]J. A. Nabity, G. Mason, J. E. Engel, J. W. Daily, R. S. Lagumbay, and D. Kassoy, "Studies of MEMS colloid thrusters," AIAA Paper No. 2006-5007, 2006.
[14]B. S. Peter, R. A. Dressler, Y.-h. Chiu, and T. Fedkiw, "Electrospray propulsion engineering toolkit (ESPET)," Aerospace **7**, 91 (2020).
[15]E. Gustan-Gutierrez and M. Gamero-Castaño, "Microfabricated electrospray thruster array with high hydraulic resistance channels," J. Propul. Power **33**, 984–991 (2017).
[16]D. Courtney, H. Li, P. Lozano, P. GomezMaqueo, and T. Fedkiw, "On the validation of porous nickel as substrate material for electrospray ion propulsion," in *46th AIAA/ASME/SAE/ASEE Joint Propulsion Conference & Exhibit* (AIAA, 2010).
[17]D. Krejci, A. Reissner, B. Seifert, D. Jelem, T. Hörbe, F. Plesescu, P. Friedhoff, and S. Lai, "Demonstration of the IFM nano FEEP thruster in low earth orbit," in 4S Symposium, Sorrento, Italy, 2018.
[18]D. V. M. Máximo and L. F. Velásquez-García, "Additively manufactured electrohydrodynamic ionic liquid pure-ion sources for nanosatellite propulsion," Addit. Manuf. **36**, 101719 (2020).
[19]D. Olvera-Trejo and L. F. Velásquez-García, "Additively manufactured MEMS multiplexed coaxial electrospray sources for high-throughput, uniform generation of core–shell microparticles," Lab Chip **16**, 4121–4132 (2016).
[20]K. Huhn, T. Henning, P. J. Klar, and S. Hengsbach, "Colloid emitters in photostructurable polymer technology: Fabrication and characterization progress report," in 34th International Electric Propulsion Conference, IEPC-2015-120, Kobe, 2015.
[21]K. Huhn, M. Piechotka, T. Henning, and P. J. Klar, "Investigation of the emission behavior of miniaturized SU-8 based colloid emitters," in 33rd International Electric Propulsion Conference, IEPC2013-141, Washington, DC, 2013.
[22]Y.-H. Chiu and R. A. Dressler, *Ionic Liquids for Space Propulsion* (ACS Publications, 2007), pp. 138–160.
[23]R. Martinez-Duarte and M. Madou, *Su-8 Photolithography and its Impact on Microfluidics* (CRC Press, 2011), pp. 231–268.
[24]A. del Campo and C. Greiner, "SU-8: A photoresist for high-aspect-ratio and 3D submicron lithography," J. Micromech. Microeng. **17**, R81–R95 (2007).
[25]S. Dandavino, C. Ataman, C. N. Ryan, S. Chakraborty, D. Courtney, J. P. W. Stark, and H. Shea, "Microfabricated electrospray emitter arrays with integrated extractor and accelerator electrodes for the propulsion of small spacecraft," J. Micromech. Microeng. **24**, 075011 (2014).
[26]J. A. Nabity, "The miniaturization of the colloid thruster to the micro scale," Ph.D. thesis, University of Colorado at Boulder, 2007.
[27]F. L. Kunze, "Data for 'taking internally wetted capillary electrospray emitters to the sub-ten-micrometre scale with 3D microlithography,'" https://doi.org/10.22029/jlupub-117 (2021).

3.2 Publication II: Space Propulsion Conference 2022

This conference publication marks a significant advance in the characterisation of SU-8 polymer and the analysis of micro 3D-printed electrospray emitter arrays. This publication focuses on the significant improvements to the 3D printing process and 3D design for the previously presented emitters. The characterisation of emitter arrays comprising six emitters was conducted through the implementation of a series of experiments. The results are presented in this publication. Moreover, radiation hardness tests were conducted on the SU-8 polymer. It is imperative to conduct such tests in order to ascertain the suitability of polymer-based emitters for the harsh environment of space. Infrared absorption experiments were conducted on irradiated SU-8 polymer samples. The results demonstrated that the polymer exhibited no adverse effects following exposure to high-energy gamma radiation.

F. Kunze wrote the first draft of the manuscript. The manuscript underwent revision by all of the contributing authors. The experiments and data acquisition were conducted by F. Kunze. Furthermore, P. Klar and T. Henning provided supervisory and project management oversight.

VALIDATION OF MICRO 3D PRINTED ELECTROSPRAY THRUSTERS

ESTORIL, PORTUGAL | 09 – 13 MAY 2022

Fynn L. Kunze [1,2,3], Torsten Henning [1,2], Peter J. Klar [1,2]

[1] Institute of Experimental Physics I, Justus Liebig University, Giessen, Germany
[2] Center for Materials Research ZfM/LaMa, Justus Liebig University, Giessen, Germany
[3] Email: fynn.kunze@physik.uni-giessen.de

KEYWORDS: electrospray, miniaturisation, micro 3D printing, two-photon-polymerisation

ABSTRACT:

Highly miniaturised capillary type electrospray emitters fabricated by micro 3D printing using two-photon-lithography are presented. The emitters are as small as 10 micrometres in lateral dimensions, which makes them more than one order of magnitude smaller than comparable emitters fabricated by 3D technology. Furthermore, extraction data and operation parameters for a six emitter cluster operating in different extraction modes are presented. Additionally, irradiation experiments on SU-8 were performed with the conclusion that SU-8 is resistant to radiation and suitable for space applications.

1. INTRODUCTION

Miniaturisation is a very prominent aspect of spacefaring endeavours. By reducing the size of the satellites more can be deployed per launch and with a higher degree of integration these satellites can perform more tasks at the same time. A main component for satellites is the thruster system, which is most likely an electric propulsion system [1,2]. Such systems take a considerable portion of the total satellite's payload. One approach to improve the miniaturisation is to develop thruster systems from existing technologies and make them smaller. The other approach we follow is to improve already small systems. Electrospray emitters fall into the second category, as they are inherently small. Furthermore, they scale favourably upon miniaturisation and have low power requirements. Additionally, if ionic liquids are used as propellant, electrospray emitters can be operated in ambipolar mode, thus making them self-neutralising. Electrospray emitters operate by applying a static voltage between a fluid and an extraction electrode. Under the influence of the electric field the exposed fluid is deformed and a so called Taylor cone forms. At the tip of the cone the electric forces are so large that fluid molecules can overcome the coherent forces and exit the fluid as a spray [3]. There are already electrospray thrusters of the porous emitter type with flight heritage [4,5]. Our goal is to explore the usage of novel 3D printing technology to manufacture and further miniaturise internally wetted capillary type electrospray emitters. We aim for capillary orifices at the same size or even smaller than the pores of porous emitters, thus eliminating any randomness and guaranteeing well defined emitter dimensions. This approach allows for highly customisable thruster systems with a scaling-up-by-numbering-up scheme resembling the principle of modern displays with a highly variable number of pixels. Furthermore, a high degree of miniaturisation and integration of the whole system can be achieved [2,6].

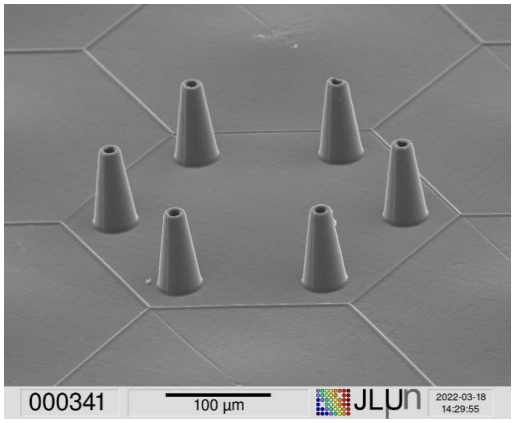

Figure 1. SEM image of a six emitter cluster. The emitters are placed in a ring configuration with 100 µm spacing. All emitters are identical with a capillary diameter of 10 µm and a height of 70 µm over the base.

2. MICRO 3D PRINTING OF ELECTROSPRAY EMITTERS

Internally wetted capillary type emitters with lateral dimensions in the single digit micron range are hard to fabricate. To achieve a high degree of miniaturisation, fabrication methods from micro-systems technologies such as photolithography are necessary. Our previous work focused on planar photolithography. The approach used layers of SU-8, a negative tone photo epoxy with photosensitivity in the UV range, stacked together to generate simple 3D structures, so called 2.5D emitters [6,7]. The layers had holes which were used to extract propellant from underneath the emitter assembly. Our manufacturing method connects to the planar lithography and improves the 3D capabilities for emitter fabrication with 3D micro lithography, or two-photon-lithography, at its core. This allows for reliable 3D micro printing with sub-micrometre resolution. For the emitter fabrication we use a batch process with optimised parameters.

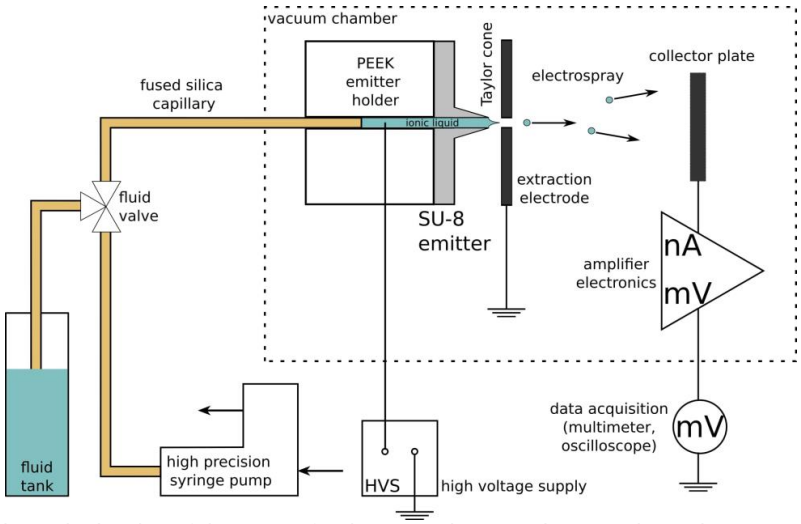

Figure 2. Schematic drawing of the set-up for the extraction experiments. The emitters are placed in the middle inside the vacuum chamber with a moveable electrode in front. A high precision syringe pump supplies the propellant to the emitters via a fused silica capillary. A collector plate catches all the extracted ions and an amplifier electronics translates the current signal into a voltage signal which is than captured.

SU-8 is spin coated onto a silicon wafer with a resist thickness of more than 100 µm. Afterwards the wafer is mounted into the 3D lithography device, PPGT from NanoScribe™ and the desired structures are printed into the resin. The device uses a 780 nm femtosecond laser which is focused through a microscope optics. While unfocused the laser can pass through the resin without triggering a photochemical reaction due to the low photon energy, however, in the area around the focal point of the optics the intensity is high enough to trigger two-photon-absorption processes. Two 780 nm photons provide the same energy as an UV photon, thus triggering a photochemical. Scanning the focus through the resin by changing the laser path with mirrors (galvo scan) or moving the sample (piezo scan), arbitrary 3D structures may be manufactured. Our fabrication process allows for the batch processing of more than ten emitter clusters in one manufacturing step. The whole fabrication process in detail was reported by the authors in 2021 [8]. For the experiments described a cluster of six identical emitters with a capillary diameter of 10 µm was used. The cluster was orientated in a ring shape to yield the same emission environment for each of the six emitters. Fig. 1 shows a scanning electron microscope (SEM) image of such a cluster. The whole emitter cluster as well as the base plate are manufactured from pure SU-8 photopolymer. Inside the volcano shaped emitter a capillary extends through the emitter and the base plate, thus allowing propellant to be fed to the emitter tip from below. The capillary diameter, length and even the shape can be freely customised for the desired application.

3. ELECTROSPRAY EXTRACTION

We used the experimental setup previously reported for the characterization of the emission behaviour [8]. An external copper ring with an inner diameter of 2 mm and an outer diameter of 4 mm serves as extraction electrode. The current signal was acquired via a high precision amplifier with a gain factor of 10^7 V/A. A schematic drawing of the experimental set-up is shown in Fig. 2. Extraction voltage, distance to the extraction electrode and propellant flowrate can be adjusted during the experiment. The voltage can be adjusted with a computer controlled high voltage source, the distance can be adjusted using a high precision piezo stage and the feed rate is controlled with a

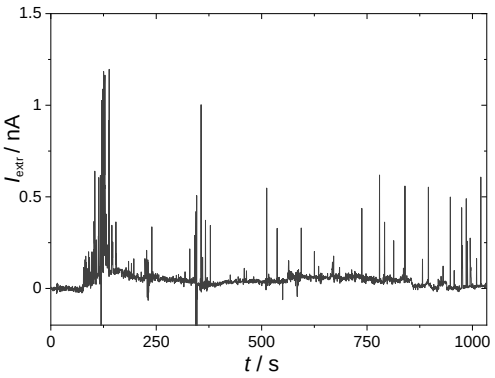

Figure 3. Current extracted from a six emitter cluster operating at 3000 V extraction voltage, 2 mm distance to the electrode and 0.1 µl/min feed rate. The signal indicated the operation in droplet spray mode, with distinct single peaks and a low base current.

high precision syringe pump. The syringe pump is able to work in infuse and withdrawal mode, thus allowing to fine tune the feed rate. By systematically changing these three parameters, different points of operation were found. Fig. 3 shows data of the emitters operating in droplet spray mode. The operation parameters were 3500 V extraction voltage, 2 mm distance of the electrode to the emitter and 0.1 µl/min feed rate. The signal fits the 'droplet spray mode' described in the literature [9]. Multiple peaks are visible on top of a constant current. The low constant current can be explained by smaller droplets or single ions which are extracted at a constant rate Additionally the bigger droplets are extracted at irregular intervals, thus creating the peaks. In the beginning of the extraction around 100 s, more peaks at a higher rate are visible, which indicates, that the start-up conditions vary from the continuous operation conditions. We suspect, that in the beginning, the build-up of fluid or a higher voltage are influencing the Taylor cone formation. Once a stable cone is established less voltage and fluid may be necessary to maintain it. We further suspect that not all emitters of the cluster are active for the data sown in Fig. 3. Data shown in Fig. 4 was acquired in a repeated experiment with a similar emitter cluster. Operation parameters for this experiment were 4000 V extraction voltage, 2 mm distance of the electrode to the emitter and 0.05 µl/min feed rate. The extraction is at a higher level compared to the extraction displayed in Fig. 3. and exhibits more stable sections. Particularly in the time frame from 430 s till 580 s very stable extraction with a constant current of 1.2 nA can be observed. In this time frame the emitter cluster is most likely operating in a cone jet mode [9]. In the following sections the extraction is also relatively stable, but with more dominant droplet peaks. Over the whole time period of 1800 s no alterations of the extraction parameters were made, yet the extraction behaviour changed over time. We conclude, that either the parameters need to be adjusted during the extraction process or the external parameters like the electrode geometry need to be changed to achieve a more consistent extraction. Though only semi stable, we achieved an extraction of least 1 nA over a time period of 1800 s. The behaviour can be reproduced with different emitter clusters under the same operation parameters.

4. RADIATION HARDNESS OF SU-8

The emitters are fabricated from pure SU-8 polymer and therefore have to fulfil multiple criteria to be used under space conditions. They have to be vacuum compatible. This is not an issue as SU-8 has been used in a high vacuum conditions without outgassing and deterioration due to low pressure. Another important aspect is the exposure of the emitters to cosmic radiation. To determine the influence of high energy radiation on SU-8 we conducted multiple experiments where emitters or emitter like structure fabricated from SU-8 were exposed to a ^{60}Co source. The used ^{60}Co source emits gamma radiation with 1.17 MeV and 1.33 MeV with an activity of 982 MBq. The sample was placed at a distance of 1 m to the source and was exposed for 144 hours. To determine any changes in the morphology or the material composition we used an infrared (IR) transmission characterisation. The transmission spectrum of the exposed sample was compared to a reference sample prepared in the same fabrication batch. Fig. 5 shows the two graphs for the reference and the irradiated sample. Both graphs show identical locations for the local maxima. The absorption modes fit very well to the organic compounds which SU-8 is composed of. There are clearly absorption modes for the benzene rings as well as the epoxide groups [10]. The small difference in intensity are measurement uncertainties due to the sample exchange. As both graphs show exactly the same absorption modes, we conclude that there is no obvious change to the structure and composition of

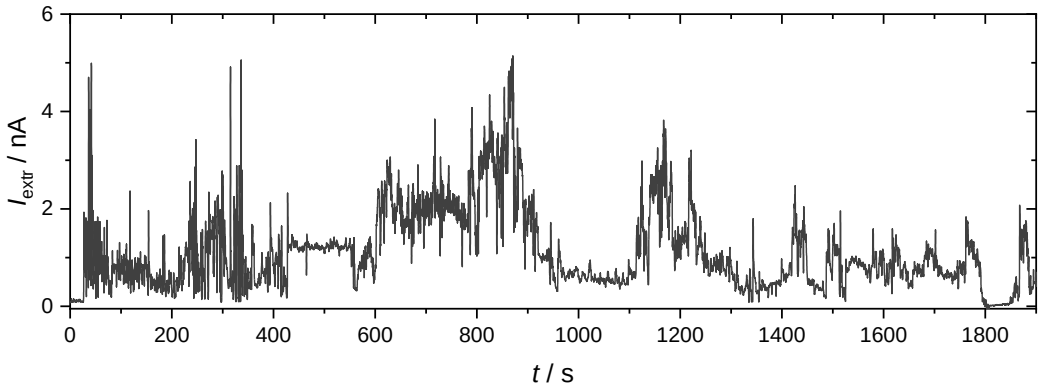

Figure 4. Extracted ion current over time for a six emitter cluster operating at 4000 V extraction voltage, 2 mm distance to the electrode and 0.05 µl/min feed rate. The emission is semi stable with some stable parts and unstable periods. The extraction behaviour changes over the shown timeframe without any changes to the extraction parameters.

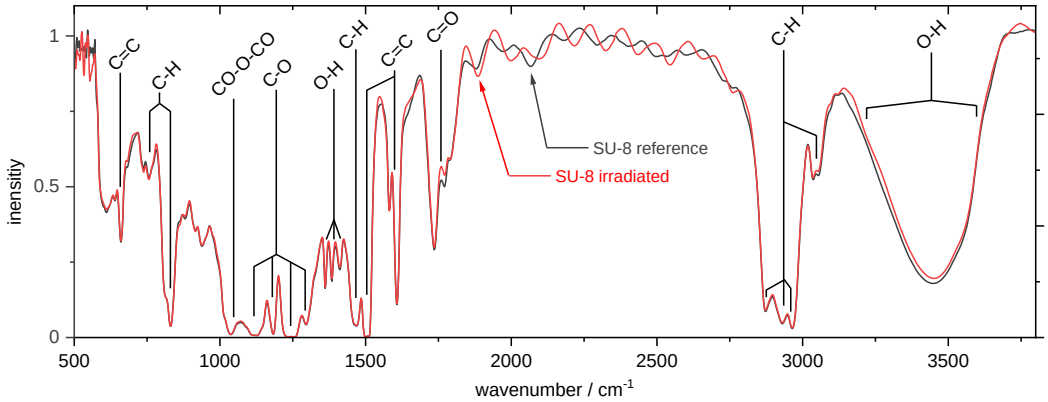

Figure 5. Infrared transmission spectrum for 20 µm thick SU-8 plates. The prominent absorption modes were labelled according to their corresponding compound.

the SU-8. New modes for reaction products should be visible in the IR absorption curve if there was any reaction due to the radiation. A different experiment used a high energy neutron source with comparable results reported in literature [11]. The SU-8 showed minimal structural change due to radiation exposure. From these results we conclude that SU-8 is highly resistant to high energy electromagnetic and particle radiation and therefore, is suitable for space applications.

5. CONCLUSION AND FUTURE WORK

Internally wetted capillary type electrospray emitters with capillary diameters as small as 10 µm were fabricated from pure SU-8 photopolymer with a two-photon-polymerisation device. SU-8 structures were exposed to high energy electromagnetic radiation to test the radiation hardness of SU-8. Data for infrared transmission for SU-8 exposed to gamma radiation was shown and from the data we conclude no morphology changes of the SU-8 due to the radiation exposure. Furthermore, we presented extraction data for 3D micro printed emitter clusters operation in droplet spray mode and cone jet mode. The obtained data shows that stable emission from such emitters is possible, but has yet to be optimised. In the future we want to improve the stability of the extraction. Further, we want to characterise the influence of the variation of extraction parameters on the emission behaviour. We also intend to obtain time of flight data as well as an estimate for the specific impulse for such emitters. For the time of flight measurements, a high resolution delay line detector is currently integrated into the experimental set-up. To further improve upon the miniaturisation aspect, we want to integrate the extraction electrode into the emitter assembly. Some prototypes were already fabricated but not yet ready for use. This should reduce the necessary extraction voltage by an order of magnitude and opens up the use for ion optics to increase the specific impulse.

6. ACKNOWLEDGMENTS

The authors gratefully acknowledge funding by the federal state of Hessen and the European Regional Development Fund (ERDF/EFRE 2014–2020), Vorhaben: “Innovationslabor: Physik unter harschen Bedingungen” FKZ: FPG991 0002/2019.

7. REFERENCES

1. Lemmer, K. (2017) Propulsion for CubeSats. *Acta Astronautica* **134**, 231–243
2. Holste, K. & others (2020) Ion thrusters for electric propulsion: Scientific issues developing a niche technology into a game changer. *Review of Scientific Instruments* **91**, 061101
3. Taylor G. I. (1964) Disintegration of water drops in an electric field, *Proceedings of the Royal Society of London*. Series A. Mathematical and Physical Sciences **280**, 383–397
4. Courtney, D. & others (2010) On the validation of porous nickel as substrate material for electrospray ion propulsion, In Proc. *46th AIAA/ASME/SAE/ASEE Joint Propulsion Conference & Exhibit*
5. Krejci, D. & others (2018) Demonstration of the IFM nano FEEP thruster in low earth orbit, In Proc. *4S Symposium*, Sorrento, Italy
6. Huhn K., Henning T., Klar P.J. & Hengsbach S. (2015), Colloid emitters in photostructurable polymer technology: Fabrication and characterization progress report, In Proc. *34th IEPC ‘Int. Electric Propulsion Conf.*, Kobe, IEPC-2015-120
7. Henning, T.; Huhn, K.; Klar, P.J. (2019) Characterisation of electrospray microemitters fabricated by planar and 3D photolithography, In Proc. *36th IEPC Int. Electric Propulsion Conf.* Vienna, IEPC-2019-344
8. Kunze F. L., Henning T. & Klar P. J. (2021) Taking internally wetted capillary electrospray emitters to the sub-ten-micrometer scale with 3D microlithograph, *AIP Advances* **11**, 105315
9. Peter B. S., Dressler R. A., Chiu Y.-h, & Fedkiw T. (2020), *Electrospray Propulsion Engineering Toolkit (ESPET)*, Aerospace **7**

10. Socrates G. (2001) Infrared and Raman Characteristic Group Frequencies - Tables and Chats, **3rd** edition
11. Key M.J., Cindro V., Lozano M. (2004) On the radiation tolerance of SU-8, a new material for gaseous microstructure radiation detector fabrication, *Radiation Physics and Chemistry* **71**(5), 1003-1007

3.3 Publication III: IEPC 2022

This publication presents a significant advancement in the characterisation capabilities of electrospray emitters, as well as an advancement in the fabrication of arrays. A time-of-flight mass spectrometry method was implemented in the existing characterisation setup. This configuration enables the precise measurement of the flight time of ions and ion clusters. A Bradbury-Nielsen ion gate was redesigned, optimised and tested for use in this application. The data obtained from the time-of-flight experiments enables the calculation of supplementary information regarding the ion emission of the micro-emitters. The data obtained allows for the calculation of specific impulse, droplet distributions and overall efficiency. This constitutes a requisite step towards a comprehensive characterisation of the 3D micro-printed electrospray emitters. Moreover, improvements in the fabrication process have enabled the production of emitter arrays comprising over 250 individual emitters. Furthermore, the fabrication errors were reduced in order to enhance the reliability of the printing process.

F. Kunze wrote the first draft of the manuscript. The manuscript underwent revision by all of the contributing authors. The experiments and data acquisition were conducted by F. Kunze. K. Holste and J. Zorn provided support during the planing and implementation of the time of flight experimental set-up. Furthermore, P. Klar and T. Henning provided supervisory and project management oversight.

3D micro printed internally wetted capillary type electrospray emitters on the single micrometer scale

IEPC-2022-175

Presented at the 37th International Electric Propulsion Conference
Massachusetts Institute of Technology, Cambridge, MA, USA
June 19-23, 2022

Fynn Kunze[1], Jana Zorn[2], Torsten Henning[3], Kristof Holste[4] and Peter J. Klar [5]
Justus-Liebig-University Giessen, Heinrich-Buff-Ring 16, 35392 Giessen, Germany

Internally wetted capillary type electrospray emitters arrays fabricated by 3D micro printing are presented. The emitter arrays consist of more than 200 individual emitters in different configurations. Fabricated from pure SU-8 photo epoxy the emitters show very high mechanical, chemical and radiation resistances. Furthermore, a time of flight set-up for the characterization of the emission from such emitter arrays is presented and preliminary time of flight data is shown.

I. Nomenclature

EMIM-BF_4	=	1-Ethyl-3-methylimidazolium tetrafluoroborate (an ionic liquid)
E_{el}	=	Electric energy
E_{kin}	=	Kinetic energy
g_0	=	Gravitational constant of the earth
I_{sp}	=	Specific impulse
L	=	Flight path length
m	=	Ion mass
q_{sp}	=	Ion charge
T_{flight}	=	Particle flight time
U_{extr}	=	Extraction voltage
v_{ion}	=	Ion velocity

II. Motivation and introduction

The ESA prognoses the number of small space craft already and to be launched to increase exponentially by the year. Already more than 1000 satellites will be launched by 2022 and up to 50 000 small spacecraft will be in orbit by 2030 [1]. Driving factor for the commercial interest are massive constellations such as Starlink and OneWeb as well as the more easily accessible rides. Highly integrated thruster systems with as small as possible mass and lateral dimensions for the application on small, micro and nano satellites are in high demand, Furthermore, with the already sparse Xenon supplies, plasma based thrusters may not be the optimal choice in the future, which leads to the development of new innovative thruster solutions. Electrospray emitters are an interesting choice as a micropropulsion solution. They offer a very high specific impulse, low power requirements and precise thrust management, which makes them a very good choice for micro and nano satellites [2–4]. Furthermore, they are highly miniaturizable and even scale favorably on

[1]PhD cand., Institute of Experimental Physics I and Center for Materials Research, Fynn.Kunze@physik.jlug.de
[2]MSc cand., Institute of Experimental Physics I, Jana.Zorn@physik.jlug.de
[3]Senior staff scientist, Institute of Experimental Physics I and Center for Materials Research, Torsten.Henning@physik.jlug.de
[4]Senior staff scientist, Institute of Experimental Physics I, Kristof.Holste@physik.jlug.de
[5]Director of Institute of Experimental Physics I and Center for Materials Research, Head of EP-group, Peter.J.Klar@exp1.physik.uni-giessen.de

miniaturization. Additionally they may be operated with liquid metal or ionic liquids, two readily available propellants. Liquid metal based thrusters from e.g Enpulsion have flight heritage [5] and are currently in high demand with over 100 units of the EnpulsionNano sold in 2022 [6]. This indicates a high interest in electrospray propulsion systems and the need to develop novel electrospray systems, such as the micro 3D printed emitters presented here.

Electrospray emitters operate by applying a static electrical voltage between an extraction electrode and a liquid propellant. Most commonly used are liquid metals or ionic liquids, which are easy to ionize or are already ionized. The propellant exposed to the electrical field forms a conic shape towards the extraction electrode, a so called Taylor cone [7]. The electrical field at the tip of the cone is amplified to a degree where the propellant is ionized and already existing ions are able to leave the propellant forming a spray of ions or droplets. Electrospray emitters can operate in different spray modes, each having its own characteristics. For example, droplet spray mode extracts mass rich heavy droplets at comparably low velocities, while ion spray mode extracts single ions at high speed [8]. Currently there are three dominant emitter types used. Porous emitter types supply the propellant through their porous structure to the surface where it can interact with the electrical field [8]. An example are the emitters manufactured by Enpulsion which use a tungsten sponge as base material to form conic emitter structures. These emitters rely on the the statistical distribution of the pores to evenly supply the propellant to the surface an thus are limited regarding their size and shape by the characteristics of the porous material. There are approaches to manufacture uniform porous materials by sintering silica pearls, however, this is part of ongoing research [9]. The second emitter type is the externally wetted emitter type [8]. These emitters supply the propellant over the surface of an emission structure, like a cone or an edge. The challenge of this emitter type is to get the right amount of propellant onto the surface. If to much liquid is supplied, unwanted interaction may occur and impede or influence the formation of an controlled ion spray. Last type of emitter are internally wetted capillary type emitters [8, 10, 11]. For this kind of emitter the propellant is fed through thin capillaries and is extracted from the orifice at the end of the capillary. Challenging for this type of emitter is the low hydraulic resistance, which may easily lead to propellant spilling out of the capillary and wet the structures around the orifice, thus impeding intended operation [12]. A way to approach this challenge is the application of a 3D micro printing technology, the two photon lithography. This manufacturing method allows the additive manufacturing of high aspect ratio capillaries with a high degree of freedom The freedom of design also includes the fluid paths where flow inhibiting structures may be included. Thus the hydraulic resistance can be tailored to the specific application intended for the emitters. This is also our approach to a novel electrospray design, which uses a photo sensitive polymer, called SU-8, as base material and is fabricated by two photon lithography.

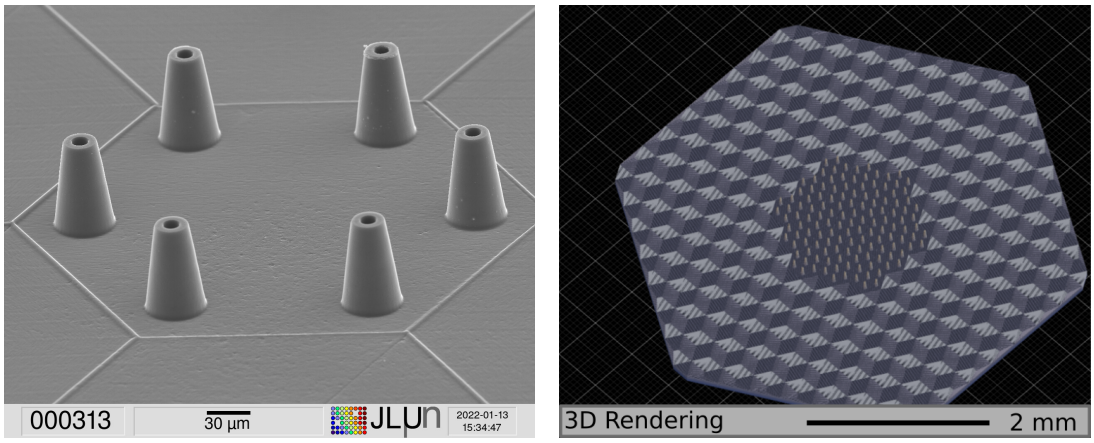

(a) **(b)**

Fig. 1 (a) SEM image of a 3D printed cluster of six individual emitters and (b) a 3D rendering of an advanced emitter array with more than 200 individual emitters

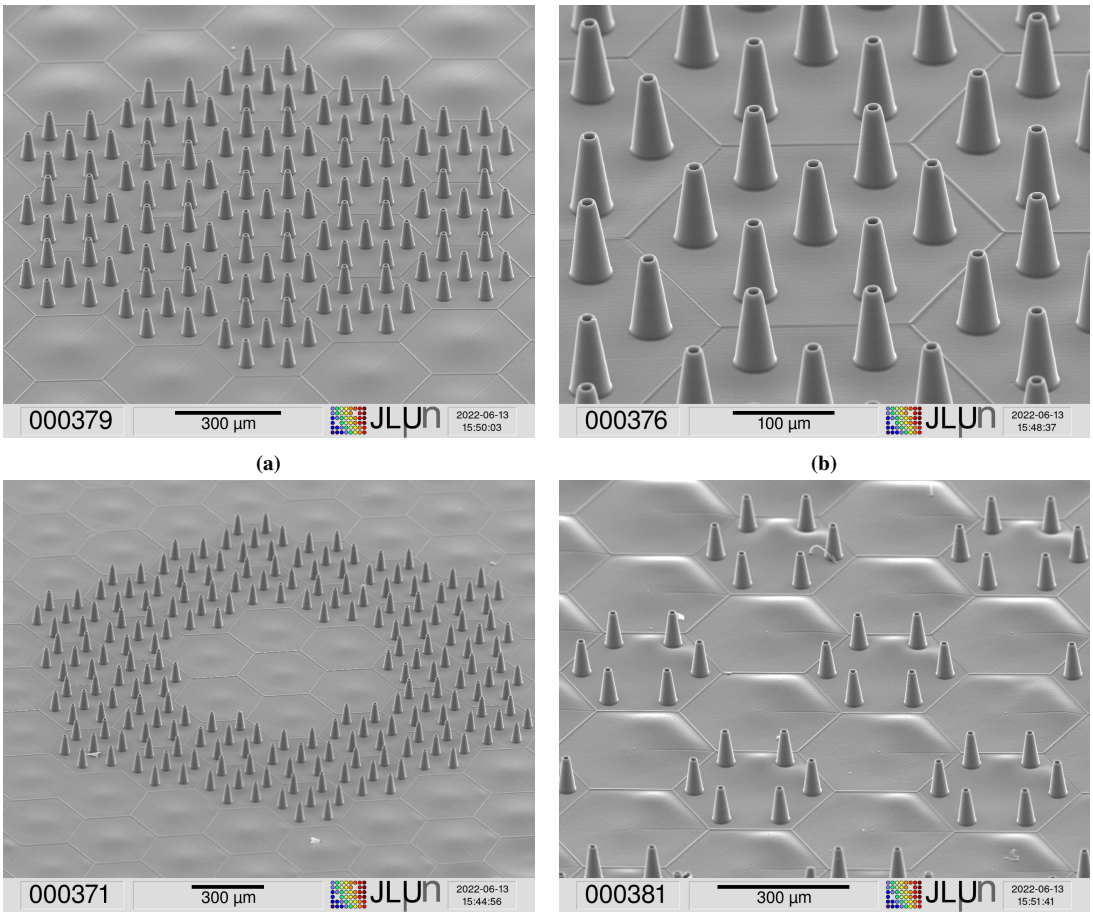

Fig. 2 SEM images of multiple array configurations with (a) the emitter array from Fig. 1b with more than 200 emitters evenly distributed emitters, (b) a close up shot of the same array, (c) an array in ring configuration and (d) an array in cluster configuration.

III. Manufacturing of emitters and arrays

The feasibility of the manufacturing of electrospray emitters by photo lithography has already been proven by the authors. Emitter and even some arrays have been manufactured by 2D planar [13–15] and 3D lithography (two photon lithography) [10, 11]. A process to reliably micro 3D print capillary type electrospray emitters with capillary diameters in the singe micrometer range has been reported by the authors in 2021 [10]. The core of this manufacturing method is the application of the two photon lithography. Two photon lithography uses a near infrared pulsed laser, which is focused through a microscope objective into a layer of photoresist. The photons emitted by the laser have on their own too little energy to trigger a photo chemical reaction in a typical photo sensitive resin, in our case SU-8. Only at the focal point of the laser the intensity is sufficiently high to trigger two photon absorption processes at a very high rate, while the unfocused part of the laser beam just passes through the photoresist. While one photon carries to little energy, two photons, however, provide a similar energy as an ultra violet photon, thus triggering the photo reaction in the resin. By scanning the focal point through the resin in all three dimensions, any 3D structure can be written to the resin layer. If used with an negative tone photoresist, like SU-8, the exposed areas harden and can be washed out of the unexposed resin after the process. The exact process parameters were reported by the author in 2021 [10]. SU-8 is

already validated as a suitable material for space applications. It shows high mechanical and chemicals stability and is very resistant to electromagnetic and particle radiation [11, 16]. A resulting emitter cluster with six emitters is shown in Fig. 1a as well as a selection of arrays are shown in Fig. 2.

The 3D lithography further allows the fabrication of advanced emitter arrays. As the individual emitters are very small and only provide a fraction of a nanonewton of thrust, usable thrust levels can be achieved by increasing the number of emitters. The authors have proven, the reliability and print quality over a large printing area [10, 11]. This allows the fabrication of emitter arrays consisting of hundreds of individual emitters. Furthermore, due to the high freedom of design the emitter arrays can also be tailored according to the user's wishes. The individual emitter shape, structure and position in the array can be chosen freely. Figure 1b shows a render of an evenly distributed emitter array and Fig. 2a shows a SEM image of the finished array. The individual emitters are identical in form and spaced equidistant, thus representing one of the simpler array configurations. A close up shot shown in Fig. 2b of the center part of the array shows the high reprinting precision and overall print quality. It is possible to use the same program code, which resulted in the even distribution array in Fig. 1b to fabricate ring arrays or arrays of smaller grouped clusters, which are shown in Fig. 2c and Fig. 2d. These arrays are more complex and show the advantages of this fabrication method. All of the presented arrays were fabricated in the same batch process using the same printing program, with a printing time of less than 7 h per whole emitter array, including the emitters as well as a supporting base around them. One complete emitter array measures about 5 mm in diagonal, with the active emitter area as small as 1 mm to 1.5 mm in diameter.

IV. Time of flight experiments

Time of flight experiments (ToF) are a necessary step to determine the performance and the extraction behavior of electrospray thrusters. Depending on the type of extraction mode emitters can output ions, droplets, or a mixture of both in varying ratios. Depending on the spray mode, either more thrust by extracting heavy droplets or higher specific impulse I_{sp} by extracting pure ions can be achieved. Time of flight experiments give insight into plume composition, ion velocity and mass distribution at a given point of operation of the emitter array.

The concept of time of flight measurements stems initially from nuclear physics, which focuses on single particles or atoms and the occurring reactions at high energies. At its core ToF relies on the law of energy conservation to gain information about the kinetic energy E_{kin} of a given particle by sending it along a predetermined path of a certain length L and measuring the time it needs to travel one way. The flight time T_{flight} in conjunction with the path length L gives information about the velocity v_{ion} of the particle.

$$v_{ion} = \frac{L}{T_{flight}} \tag{1}$$

If either the mass m or the starting energy E_{start} of the particle is known, one can calculate the missing information from Eq. (2).

$$E_{kin} = \frac{1}{2} m v_{ion}^2 = E_{start} \tag{2}$$

For our purpose of extraction from electrospray emitters, the energy at which the particles start is given by the extraction voltage U_{extr} and the charge of the particle q, thus can be described by Eq. (3).

$$E_{start} = E_{el} = qU_{extr} \tag{3}$$

By combining Eq. (1), Eq. (2) and Eq. (3) we can calculate the mass m of a detected particle for a fixed set-up with a path length L.

$$m = \frac{2qU}{v_{ion}^2} = 2qU_{extr} \frac{T_{flight}^2}{L^2} \tag{4}$$

Furthermore, the specific impulse I_{sp} can also be calculated from Eq. (1) by dividing the velocity v_{ion} by the gravitational constant of the earth g_0.

$$I_{sp} = \frac{v_{ion}}{g_0} = \frac{L}{g_0 T_{flight}} \tag{5}$$

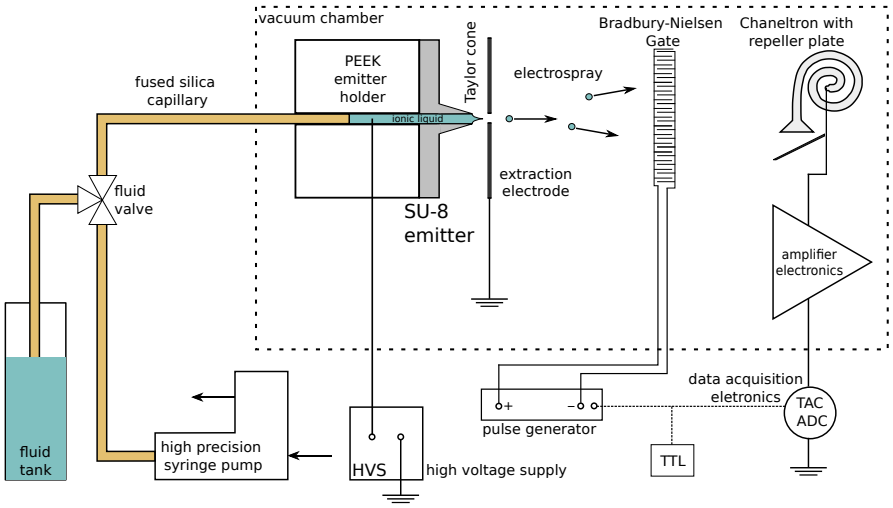

Fig. 3 Schematic drawing of the set-up for the time of flight experiments.

A. Experimental set-up

For the time of flight experiments we use the previously reported experimental set-up for the characterization of electrospray emitters at the JLU [10, 11]. Additionally to the set-up already in use, a Bradbury-Nielsen ion gate was integrated into the flight path to control the ion beam. Furthermore, the collector plate from the previous DC characterization set-up was exchanged for a channeltron detector with a much higher detection sensitivity. A schematic drawing of the set-up is shown in Fig. 3.

To acquire time of flight data from ion sources operating at constant or semi constant emission mode, the ion beam has to be chopped into small packages which do not overlap, meaning one whole package can reach the detector before next package is sent on its way. If the time frame of a single package is to o long, very fast ions from the next package can interfere with measurement of the previous package. Is the time frame too short few ions can pass the gate and result in very low detection rates and thus long measurement times. Therefore, an ion gate is necessary to reliably control the ion intake to the detector. We opt for an Bradbury-Nielsen gate, which will be discussed in more detail below. The gate is controlled by two independent DEI PVX-4130 ±6kV pulse generators. One is connected to an controllable positive HV source, the second is connected to a negative HV source. Both pulse generators are gated by a 5V square-wave transistor-transistor-logic (TTL) signal provided by a ROHDE & SCHWARZ HM8150 programmable function generator. Due to an electrical restriction of the pulse generators, which allows one only to switch from a lower potential to a higher potential, the pulse generator connected to the positive HV source has to be controlled by an inverted TTL signal. We use a single inverter gate to invert the TTL signal provided by the function generator. The data signal obtained from the channeltron is fed into an ORTEC VT120 fast preamplifier and afterwards passed through a ROENTDEK CFD1x constant fraction discriminator to eliminate time delays due to different pulse heights. Both the TTL signal and the signals from the CFD are fed into a CANBERRA MODEL 2043 time analyzer, with the TTL signal connected to the start input and the CFD signal to the stop input. The time analyzer translates the time delay between start and stop into a voltage signal ranging from 0 to 10 V, sorted from short to long. This 0 to 10 V signal is output from the time analyzer via the time to amplitude converted (TAC) output, which connects to an analog to digital converter ADC/ND-560 from NUCLEAR DATA . The ADC converters the TAC signal into 1024 or 2048 channels, depending on the device settings, and send these to an external computer to save the data. The fight time T_{flight} can be calculated using Eq. (6) from the time analyzer range T_{max}, the channel number C_{i} and the maximum number of channels C_{max}.

$$T_{\text{flight}} = \frac{T_{\text{max}}}{C_{\text{max}}} C_{\text{i}} \tag{6}$$

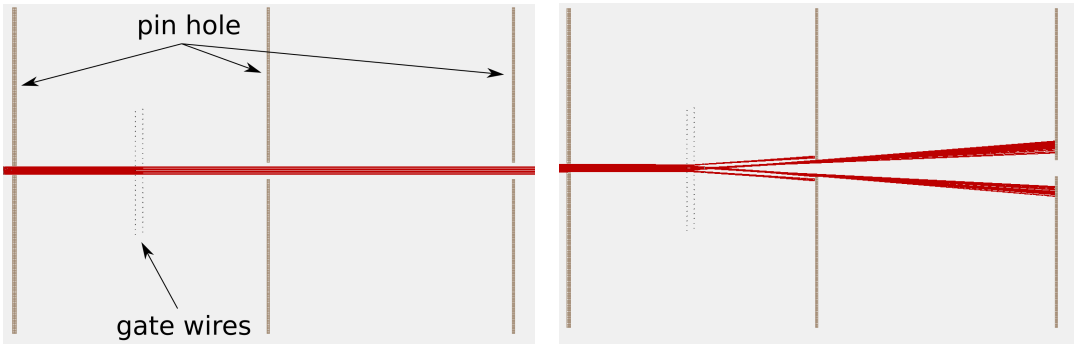

(a) (b)

Fig. 4 SIMION simulation of the flight path of ions through a Bradbury-Nielsen gate in (a) the open state and in (b) the closed state

B. Bradbury-Nielsen-Gate

In mass spectroscopy experiments ion gates are commonly used to deflect and steer ion beams. The gate is necessary in flight time experiments to control when ions may pass through to the detector. A widely used ion gate is the Bradbury-Nielsen ion gate [17]. Due to its comparably easy structure, fast reaction times and high precision, Bradbury-Nielsen gates are a logical choice for such experiments. The gate consists of two isolated wire grids placed in the same plane. The wires are alternated in such a way that neighboring wires are not connected, but the second neighbors are. The wires are commonly wound up on an external structure similar to guitar strings or are etched out very thin metal sheets. To operate the ion gate, one set of wires is placed at a negative potential while the other set is placed at an positive potential. This leads to local strong fields between the wires. However, if the potentials are applied symmetrically no far field is generated. If an ion comes near the wires while the voltages are applied to the wires the electrical attraction and repulsion from the positive and negative wires deflect the ion, independent of the type of charge, outwards. Therefore, no ions could pass the plane the wires are positioned without getting deflected. If coupled with a set of pinholes, no ions may reach the detector of the set-up while the voltage is applied [17]. This translates to a closed gate state. To open the gate one has to simply stop applying a voltage to the wires. The open close cycle, thus is only dependent on the speed at which the voltage can be applied. With the right electronics the switch between opened and closed state of the gate can be achieved in few a nanoseconds.

We opt to build our own Bradbury-Nielsen gate and therefore started with a simulation of the flight path of the expected ions in SIMION, a simulation software commonly used in nuclear physics to simulate ion flight paths, to compare different gate configurations. The simulation uses the ion masses of EMIM-BF_4, an ionic liquid commonly used in electrospray applications with the compound masses of 86.8 u for the anion BF_4^- and 111.37 u for the cation $EMIM^+$ as well as a kinetic energy of 4 keV for both ion species. The gate is simulated using a wire diameter of 0.2 mm, a wire distance of 0.6 mm and two pinholes at a distance of 30 mm in front and behind the gate with a through hole diameter of 4 mm. As gate voltages ±500 V were applied to the wires. The results from the simulation of 1000 ions are shown in Fig. 4, with a open gate in Fig. 4a and a closed gate in Fig. 4b. We further simulated a complete open-close cycle of the whole gate driven by a square wave voltage signal simulated using the Gibbs phenomenon from 0 to ±500 V and calculated transmission coefficient from the results. The results show no transmission for the EMIM-BF_4 ions if the gate in closed and a transmission of approximately 72 % for an open gate. The 30 % loss can be explained by the collision of ions with the wires while the gate is open. Nevertheless, these results are very promising for the ion gate, as a low ion rate can be beneficial for the detection, especial for very sensitive detectors, where one can compensate for a low rate by prolonging the measurement time.

We manufactured the gate according to the parameters used for the simulation. A 3D CAD drawing of the gate alongside a picture of the finished product is shown in Fig. 5. We decided to go with a single tension wire instead of an etched wire mesh as manufacturing and necessary repairs are more facile. The gate consist of two individual wire holders, with each holding one wire mesh. In Fig. 5b both holders are screwed together to from the complete gate. A spring steel wire with a diameter of 0.2 mm is wound around small steel pins embedded in a PEEK holder on one side

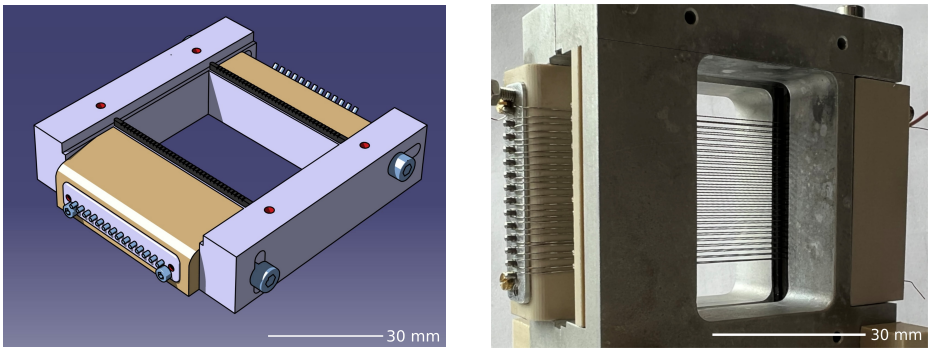

(a) **(b)**

Fig. 5 (a) CAD rendering of one half of the Bradbury-Nielsen gate alongside (b) a picture of the finish product

and an steel holder inserted in a PEEK casing on the other side. The two screws at the top and bottom of the steel holder visible in the picture define the attachment points for the wire. It is possible to control the tension of the wire by two grub screws which can move the whole steel holder outward. To guarantee a perfect spacing the wire is run trough a plastic spacer with conic grooves cut into at fixed distances of 1.2 mm. With both wire holders screwed together at an small offset, a wire mesh with a wire distance of 0.6 mm is generated. Both wire spools are completely electrically insulated from each other as no physical contact is possible. The small offset between both wire sets perpendicular to the plane due to the distance between both holders is negligible and does not impact the operation of the gate. We integrated the gate into the set-up described in Fig. 3 tested its performance. The gate performed as expected with no transmission while closed and high transmission while opened.

V. Preliminary ToF results

We started preliminary time of flight measurements with EMIM-BF_4 as an ion source extracted from a steel capillary at different extraction voltages. For the experiments we used the set-up described in Sec. IV with the aforementioned Bradbury-Nielsen gate and operated the set-up under the condition listed in Table 1.

We obtained the flight time data for EMIM-BF_4 shown in Fig. 6. Two spectra are shown from two independent measurements, with different settings for the time analyzer. The flight time was derived from the raw data obtained from the ADC following Eq.(6) and thus is only based on the assumption about the conditions listed in Table 1. further validation is required. This preliminary estimation will not result in the true flight time data, as we cannot exclude any unwanted interactions of the ions, but it should suffice to estimate the range of the flight time and mass of the detected ions. For measurements shown in Fig. 6a a time range of 20 µs was selected for the device. To get a closer look at the

Table 1 Experimental conditions for ToF experiment

Propellant	EMIM-BF_4
Emitter	Steel capillary ∅ 100 µm
Electrode	Copper ring ∅ 5 mm
Electrode distance	6 mm
Extraction voltage	-5 kV
Feed rate	0.1 µl/min
Gate voltage	±1000 V
Gate open time	1 µs
Gate switching frequency	100 Hz
Flight path length	0.8 m
Time analyzer range	20 µs and 10 µs
ADC channels	2048

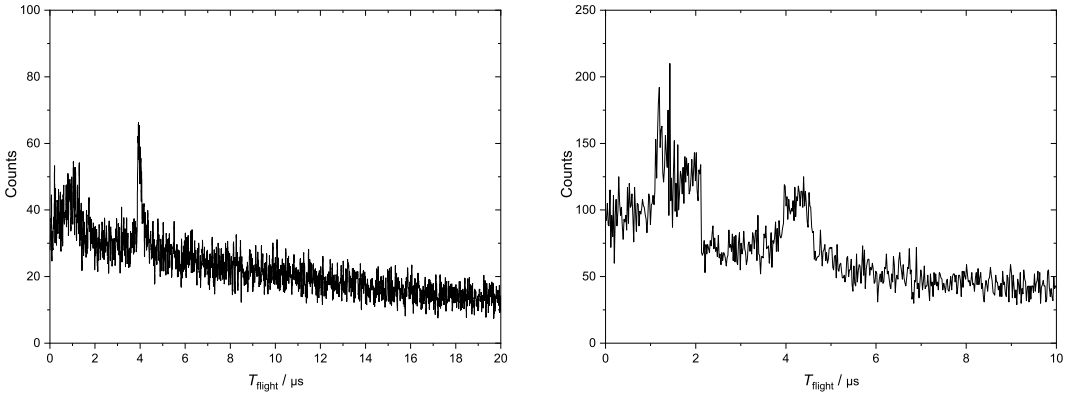

Fig. 6 Results from the preliminary time of flight measurements with the assumed (a) flight time and a time range of 20 µs and (b) a second flight time spectrum with a time range of 10 µs at 5 kV extraction voltage and EMIM-BF_4 as source

local maxima in the left part of the spectrum we repeated the measurements a second time, with a time range of 10 µs. The corresponding results are shown in Fig. 6b.

Both spectra show similar local maxima at the same flight times, at 1.2 µs, 1.8 µs and 4.5 µs. The reproducibility indicates that the data obtained truly show ions and not some electrical noise. Furthermore, no signal occurs when a physical valve in the beam path is closed, thus physically separating the source from the detector. A similar effect on the signal is achieved by permanently closing the Bradbury-Nielsen gate. No ions may reach the detector if the gate voltages are applied constantly. We also observed the difference in signal with a pulsed gate and a permanently open gate. For a permanently open gate the signal is constant over the whole time range, while a pulsed gate results in the signal shown above. The spectrum shown in Fig. 6a exhibits a small exponential decay, witch can be accounted to not optimized electronic settings and the set-up itself. The holder of the pins holes used to collect the ions deflected by the Bradbury-Nielsen gate are maybe too small and some defected ions may still pass around them, thus leading to free ions in the vacuum chamber with a exponential velocity distribution. For the more focused spectrum in Fig. 6b this effect is a lot less dominant due to the smaller time frame. The distribution is closer to a linear offset and has overall less impact on the results. These assumed flight times translate with a path length of 0.8 m to a I_{sp} range from $6.7 \cdot 10^4$ s for the 1.2 µs flight time to $1.78 \cdot 10^4$ s for the flight time of 4.5 µs.

We also estimate the mass from the flight times by applying Eq. (4) under the same assumptions as before. For a more precise interpretation of the obtained data we need to calibrate the device beforehand with a known spectrum, from which we can reference the data. The assumed masses of the ions responsible for the local maxima observable in the spectra are approximately 2 u for the 1.2 µs fight time, 6 u for the 1.8 µs flight time and 23 u to 31 u for the broad maximum at 4.5 µs flight time. Like stated before, the spectrum is not calibrated and therefore, could display the maxima at the wrong position. In the current uncalibrated state we can olay make an educated guess which peak correlats to whihc ion. As EMIM-BF_4 is used with a negative voltage applied to the ionic liquid BF_4^- are expected to be extracted, but the mass correlating to the maximum at 23 u is to low. We assume that due to some electrical discharges the BF_4^- ion is fractured in BF_3 and F^-. The fluorine ion F^- has a mass of 19 u and could be responsible for the maximum visible in the spectrum. Like stated before, this is only based on assumptions and need further validation. We have to improve on the calibration possibilities of the set-up to obtain meaningful information. Nevertheless the data obtained serves as prove of concept for our time of flight set-up and is acceptable as preliminary data.

VI. Conclusion

Multiple internally wetted capillary type emitters fabricated by 3D lithography were presented. Furthermore, the advanced array processing capabilities of the manufacturing method has been displayed, a completely customizable array consisting of more than individual 200 emitters can be manufactured. The emitters exhibit a high printing quality,

high aspect ratio capillaries and well defined features. Individual emitters of an array are almost indistinguishable and are precisely placed. Also presented were simulations for a Bradbury-Nielsen ion gate for time of flight experiments on the manufactured emitters with EMIM-BF_4 as propellant. Based on the simulations the gate was designed in CAD and fabricated afterwards. Preliminary time of flight data obtained from the set-up with the newly integrated Bradbury-Nielsen ion gate was also shown, with a prove of concept for the intended application of characterizing electrospray emitters.

Acknowledgments

The authors gratefully acknowledge funding by the federal state of Hessen and the European Regional Development Fund (ERDF/EFRE 2014 – 2020), Vorhaben: "Innovationslabor: Physik unter harschen Bedingungen" FKZ: FPG991 0002/2019. The time-of-flight setup with improved resolution is being funded by the German Federal Ministry for Economic Affairs and Climate Action under contract (FKZ) 50RS2101.

References

[1] European Space Agency, "ESA's Space Environment Report 2022," *ESA Reports*, 2022. URL `https://www.sdo.esoc.esa.int/environment_report/Space_Environment_Report_latest.pdf`.

[2] Holste, K., Dietz, P., Scharmann, S., Keil, K., Henning, T., Zschätzsch, D., Reitemeyer, M., Nauschütt, B., Kiefer, F., Kunze, F., Zorn, J., Heiliger, C., Joshi, N., Probst, U., Thüringer, R., Volkmar, C., Packan, D., Peterschmitt, S., Brinkmann, K. T., Zaunick, H.-G., Thoma, M. H., Kretschmer, M., Leiter, H. J., Schippers, S., Hannemann, K., and Klar, P. J., "Ion thrusters for electric propulsion: Scientific issues developing a niche technology into a game changer," *Review of Scientific Instruments*, Vol. 91, No. 6, 2020, p. 061101. https://doi.org/10.1063/5.0010134.

[3] Lemmer, K., "Propulsion for CubeSats," *Acta Astronautica*, Vol. 134, 2017, pp. 231–243. https://doi.org/10.1016/j.actaastro.2017.01.048.

[4] Lev, D., Myers, R. M., Lemmer, K. M., Kolbeck, J., Koizumi, H., and Polzin, K., "The technological and commercial expansion of electric propulsion," *Acta Astronautica*, Vol. 159, 2019, pp. 213–227. https://doi.org/https://doi.org/10.1016/j.actaastro.2019.03.058, URL https://www.sciencedirect.com/science/article/pii/S0094576518319672.

[5] Krejci, D., Reissner, A., Seifert, B., Jelem, D., Hörbe, T., Plesescu, F., Friedhoff, P., and Lai, S., "Demonstration of the IFM nano FEEP thruster in low earth orbit," *4S Symposium, Sorrento, Italy*, 2018. URL https://www.researchgate.net/publication/325486881.

[6] Schönherr, T., "Presentaion for the Space Propulsion conference 2022," *8th internatinonal conference on space propulsion, Estoril*, 2022.

[7] Taylor, G. I., "Disintegration of water drops in an electric field," *Proceedings of the Royal Society of London. Series A. Mathematical and Physical Sciences*, Vol. 280, No. 1382, 1964, pp. 383–397. https://doi.org/10.1098/rspa.1964.0151.

[8] Peter, B. S., Dressler, R. A., Chiu, Y.-h., and Fedkiw, T., "Electrospray Propulsion Engineering Toolkit (ESPET)," *Aerospace*, Vol. 7, No. 7, 2020. https://doi.org/10.3390/aerospace7070091.

[9] MacArthur, J., Colicci, V., Barrios, A. T., Kutina, K., and Lozano, P., "Sintered silica ceramics for electrospray propulsion emitters," *8th internatinonal conference on space propulsion, Estoril*, 2022.

[10] Kunze, F. L., Henning, T., and Klar, P. J., "Taking internally wetted capillary electrospray emitters to the sub-ten-micrometer scale with 3D microlithography," *AIP Advances*, Vol. 11, No. 10, 2021, p. 105315. https://doi.org/10.1063/5.0066619, URL https://doi.org/10.1063/5.0066619.

[11] Kunze, F. L., Henning, T., and Klar, P. J., "Validation of pure SU-8 micro 3D printed internally wetted capillary type electrospray mircoemitters for thruster applications," *8th internatinonal conference on space propulsion, Estoril*, 2022.

[12] Gustan-Gutierrez, E., and Gamero-Castaño, M., "Microfabricated Electrospray Thruster Array with High Hydraulic Resistance Channels," *Journal of Propulsion and Power*, Vol. 33, No. 4, 2017, pp. 984–991. https://doi.org/10.2514/1.B36268.

[13] Henning, T., Huhn, K., and Klar, P. J., "Characterisation of electrospray microemitters fabricated by planar and 3D photolithography," *36th International Electric Propulsion Conference (IEPC), Vienna*, 2019. URL http://electricrocket.org/2019/344.pdf.

[14] Huhn, K., Henning, T., Klar, P. J., and Hengsbach, S., "Colloid emitters in photostructurable polymer technology: Fabrication and characterization progress report," *34th International Electric Propulsion Conference, Kobe*, 2015. URL http://electricrocket.org/IEPC/IEPC-2015-120_ISTS-2015-b-120.pdf.

[15] Huhn, K., Piechotka, M., Henning, T., and Klar, P. J., "Investigation of the emission behavior of miniaturized SU-8 based colloid emitters," *33rd International Electric Propulsion Conference, Washington DC*, 2013. URL http://electricrocket.org/IEPC/nl5kwbt2.pdf.

[16] Key, M., Cindro, V., and Lozano, M., "On the radiation tolerance of SU-8, a new material for gaseous microstructure radiation detector fabrication," *Radiation Physics and Chemistry*, Vol. 71, No. 5, 2004, pp. 1003–1007. https://doi.org/10.1016/j.radphyschem.2004.03.002.

[17] Bradbury, N. E., and Nielsen, R. A., "Absolute Values of the Electron Mobility in Hydrogen," *Phys. Rev.*, Vol. 49, 1936, pp. 388–393. https://doi.org/10.1103/PhysRev.49.388, URL https://link.aps.org/doi/10.1103/PhysRev.49.388.

3.4 Publication IV: Journal of Electric Propulsion

This publication represents a second significant milestone, analogous to the preceding publication. The incorporation of an extraction electrode at the emitter level signifies a substantial advancement for this technology, exemplifying a significant fabrication achievement. The integration of the electrode into the emitter assembly resulted in a notable reduction in the size of the thruster head. Moreover, the electrode is micro 3D printed and exhibits the same high precision and reproducibility as the emitters. In order to achieve this, the photo resin was replaced with IP-Q. IP-Q is a specifically developed three-dimensional lithography resin that enables the fabrication of structures at the meso- and macro-scale using a two-photon lithography apparatus. The use of IP-Q, a liquid resin, allows for the realisation of larger emitter designs, thereby offering significantly greater freedom of design. The extractor's modular design facilitates the rapid prototyping and development of the 3D-printed electrospray concept. Moreover, the characterisation setup was enhanced with the incorporation of an optical feedback system. Two cameras permit the in-situ observation of the emitter structures and the extractor electrode. The video feed provides insight into the fluid distribution within the emitter or emitter array, thus enabling the identification of the underlying causes of success or failure. Such modifications to the emitter and extractor design may be implemented in order to address the aforementioned challenges.

F. Kunze wrote the first draft of the manuscript. The manuscript underwent revision by all of the contributing authors. The experiments and data acquisition were conducted by F. Kunze. Furthermore, P. Klar and T. Henning provided supervisory and project management oversight.

Kunze *et al. Journal of Electric Propulsion* (2024) 3:3
https://doi.org/10.1007/s44205-023-00066-7

Journal of Electric Propulsion

RESEARCH Open Access

3D micro printed capillary electrospray thruster with a fully modular integrated extraction electrode

Fynn L. Kunze[1*], Torsten Henning[1] and Peter J. Klar[1]

*Correspondence: Fynn.Kunze@physik.uni-giessen.de

[1] Institute of Experimental Physics I and Center for Materials Research ZfM/LaMa, Justus Liebig University, Heinrich-Buff-Ring 16, DE-35392 Giessen, Germany

Abstract

An internally wetted capillary-type electrospray thruster design is presented. The capillary emitters are optimized for fabrication using 3D micro lithography and can achieve sub 10-micrometer capillary diameters with an aspect ratio of over 20. Also provided is a design for a completely modular integrated extraction electrode that comprises an electrode carrier produced by 3D micro lithography and a thin metal film. The electrode orifices, distance to emitters, and size are all customizable thanks to the modularity of the design, which is compatible with any electrospray thruster type. The design provides alignment precision within 5 micrometers of the emitter tip and electrode orifice. While our new electrode achieved reproducible extraction, instability is still present. The data on emission from these emitter-electrode stacks is presented, as well as in situ microscopic optical observation of individual emitters. The images demonstrate emission in multiple extraction modes, microfluidic behaviour of the capillaries in space-like conditions, and interactions of the emission modes with the integrated electrode.

Keywords: Micropropulsion, Electrospray, 3D Microlithography, Additive manufacturing

Introduction

Electrospray thrusters belong to the electrostatic thruster family [1]. They are a promising option for micro propulsion applications, such as on CubeSats. Their scalability is a key factor driving the interest in these thrusters for micro and nano satellites [2–4]. Electrospray thrusters can be easily downscaled and even benefit from it, which sets them apart from more traditional electric propulsion systems like Hall thrusters [5]. Another reason is that depending on the system configuration a neutraliser can be omitted from the propulsion system, thus reducing the already low power requirements further [2]. Additionally they provide precise thrust and impulse bits, making them ideal for high precision manoeuvres like constellation flight. Another advantage is their use of liquid or semi-solid propellants. This property renders them highly manageable during launch and integration and the accessibility of the propellants is appealing for commercial applications such as mega constellations [5].

Electrospray thrusters operate by extracting ions or droplets from a liquid propellant using a static electric field. The fluid is deformed due to the electrical field and grows into a conical shape called Taylor-cone as the field strength is increased [2, 6]. At the Taylor-cone tip, the electric field density is sufficiently high to forcibly extract ions or droplets of the propellant from the fluid, causing them to accelerate alongside the electric field [7]. To function properly, the fluid must either be conductive or have a polar component such as water [6]. For most types of elctrospray thrusters, either liquid metal or ionic liquids are typically utilized as propellant. Liquid metal must first be heated to its melting point before use. Indium is commonly used due to its relatively low melting point of 150°C [8]. Ionic liquids, on the other hand, are salts that remain in a liquid state below room temperature [9–11]. Additionally, these liquids have very low vapour pressure, allowing them to remain stable in vacuum conditions [11]. Their composition of pure ions results in high electrical conductivity, making them an ideal propellant for electrospray thrusters. Moreover, the use of ionic liquids permits extraction of both positive and negative ion species, eliminating the need for an external neutraliser [12].

An electrospray thruster typically comprises three main components: the propellant intake, emitter structure, and extraction electrode. The propellant intake, which can be either a tubing system in actively fed thrusters or a reservoir in passively fed systems, provides the necessary propellant for the emitter structure. Once the fluid reaches the emitter structure, it is exposed to an electrical field, which facilitates ion extraction. There are three variations in the structure of the emitter, distinguished by the method of supplying propellant to the emission sites. The general operating principle remains the same for all three variations [13]. One type of emitter is the porous emitter, which delivers propellant through a porous base material from which the emitter structure is formed. Usually, a conical structure is used, although wedges or edges may also be effective for facilitating ion emission [12]. Another type of emitter is the external emitter, where the propellant is supplied to the base of an emission structure and is drawn up to the emission point by surface forces [13]. Similar to porous emitters, the conical shape is usually preferred. Another approach is the capillary emitter, also known as the internally wetted emitter [13, 14]. This type employs a capillary system to convey the propellant to the emission site. Each approach presents distinctive challenges. For instance, the arbitrary pore size and distribution of porous emitter structures render their reliable production almost impracticable. External emitters may have reduced emission predictability due to the extraction of secondary ions from the fluid between emitter structures. Capillary emitters are susceptible to overflow as a result of the capillaries' low hydraulic resistance [18]. The extraction electrode is the final component required for ion extraction. It functions as the liquid's ground reference and is essential for creating the electric field necessary for extraction. Typically, a metal lattice is used as the extraction electrode, which is positioned above the emitter structure [2].

In our work we focus on the additive manufacturing of miniaturised capillary type electrospray thrusters. We utilize a micro 3D printing technique, two photon lithography, to fabricate high aspect ratio capillary emitters structures as well as a newly developed fully modular extraction electrode.

Methods

In this paper, we present a fully modular design of an electrospray thruster and report on the results obtained from testing these emitters. The included data comprise scanning electron microscope images, optical images, and extraction data. In this section we want to focus on the fabrication and characterisation methods used to obtain the result presented later on.

Additive manufacturing

3D micro printing and capillary designs

Our new design builds upon our previous work [14, 16, 17], which employs the technique of two-photon laser lithography, an additive manufacturing process. As the name suggests, this method utilizes two-photon interactions to initiate chemical reactions in a photosensitive resin [14, 15]. A single photon carries too little energy to trigger a photochemical reaction, thus passes right through the photo resist without being absorbed. A reaction can occur only if two photons are simultaneously absorbed, which necessitates a sufficiently high intensity. Such intensities are attained by focusing the laser through microscope optics [14, 15]. At the lens' focal point, the beam is compacted into a minute volume, producing very high photon densities. Inside this small volume, referred to as a 3D pixel or voxel, two photon absorption can occur [14, 15]. By using negative tone photoresist, a hardened piece of epoxy is produced inside the voxel through photochemical reactions. A 3D structure can be created by scanning the voxel through the resist, either by moving the substrate with the resin or by changing the laser path via mirrors. This process closely resembles standard 3D printing. Depending on the photoresist and microscope lens used, lateral resolutions as low as 100 nm can be attained. In comparison to other micro mechanical fabrication techniques such as micro machining or etching, two-photon lithography presents significantly fewer constraints in terms of shape and structure possibilities [15]. Under-cut, asymmetric, and even hollow structures can be manufactured using this microfabrication technique, which is often difficult or outright impossible with other microfabrication techniques. Another advantage is the ability to fabricate structures with a high aspect ratio (width to height ratio). In our previous work, we demonstrated that it is possible to fabricate structures with capillary diameters of less than 10 μm and an aspect ratio larger than 20. This possibility is directly related to the capillary design employed for the emitters [14, 16, 17]. One of the major challenges with capillary type emitters is their hydraulic resistance [18]. If the emitters possess insufficient resistance, they are prone to overflowing or producing large droplets instead of a fine ion spray. To enhance the hydraulic resistance, one solution is to increase the aspect ratio of the capillary. The flow rate through a finite capillary is described by the Hagen-Poiseuille law.

$$\dot{V} = \frac{\pi \cdot r^4}{8 \cdot \eta \cdot l}(\Delta p). \tag{1}$$

The volume flow rate $\dot{V}$ is dependent on the capillary radius r, the viscosity of the fluid η, the length of the capillary l, and the pressure gradient between the input side

and output side $\Delta p = p_{\text{in}} - p_{\text{out}}$. For our purposes, we can generalize that the pressure on the output side p_{out} is nearly equal to zero since it is open to space.

This results in two categories of variables: those dependent on the emitter design, namely the radius and capillary length, and the system variables, such as fluid viscosity and input pressure. The radius exerts the greatest influence on flow rate, as it is proportional to the 4th power. Increasing the length of the capillary would also result in an increase in resistance. However, compared to the impact of the radius, the linear increase in length has a much smaller effect. The dependence on both the radius and the capillary length is the reason why a high aspect ratio is needed to achieve low flow rates, as both a smaller radius and a longer capillary decrease the flow rate.

IP-Q Material system

In our previous work, we utilized SU-8, a photoresist, as the base material for our emitter structures. SU-8 is renowned for its mechanical stability, high resistance to solvents and chemicals, and stability under space-like conditions [16]. We employed the NanoScribe™ PPGT, a 3D lithography device, to fabricate emitters and emitter arrays with aspect ratios ranging from 5 to 20. One of the significant drawbacks of working with SU-8 is resist preparation. SU-8 needs to be applied onto a silicon wafer by means of a spin coater, resulting in very smooth but rather thin resist films. The maximum attainable layer thickness with SU-8 is about 400 µm, which imposes a limitation on the maximum height of the emitter or any other structures. Consequently, we opted to use IP-Q resist, which was specially developed by NanoScribe™ for 3D lithography with their 'large feature solution' set. With IP-Q, structures up to 10 mm in height can be fabricated. IP-Q provides comparable mechanical and chemical properties to SU-8 and performs similarly as a base material for microfluidic applications. However, there are some variations in wetting angle and surface properties which require further investigation to arrive at a comprehensive comparison.

In addition, it is necessary to verify the radiation hardness of IP-Q for future applications. For now, IP-Q serves as a suitable replacement for SU-8. Another benefit of utilizing IP-Q is the significantly faster process time as a result of using a 10× objective instead of the previously used 20× objective. The process time has been reduced from 12 hours per emitter array to 4 hours per array. It should be noted that the higher printing speed is achieved at the expense of increased voxel dimensions. With the 10× objective, the lateral voxel size is about 1.5 µm, and the longitudinal size is about 25 µm. Although the lateral size is comparable to that of the 20× objective, the longitudinal size is approximately five times larger. This enlargement of the voxel size reduces the print resolution, resulting in a slight loss of print quality. However, this effect is negligible once accounted for. Figure 1 illustrates a capillary emitter example made with the 10× objective in IP-Q. The capillary has a diameter of 40 µm and a length of 300 µm. However, a change in material system from SU-8 to IP-Q necessitated a new examination of printing parameters and structure designs to obtain equivalent results to those previously achieved using SU-8. All in all, we can now manufacture emitters that have greater height and capillary length compared to the SU-8 process.

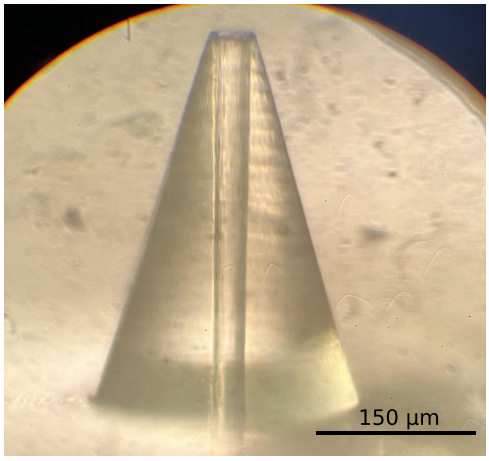

Fig. 1 Image taken through a optical microscope with a 50x magnification. The emitter is fabricated using 3D lithography in the large feature configuration and IP-Q resin. This design features a 30 µm diameter capillary with a length of 300 µm. Due to the parallax the capillary seems wider at the top, however SEM imaging shows a uniform capillary diameter over the whole length. We also included an image of an emitter with a 10 µm diameter capillary in Fig. 9 in the Appendix

Fully modular integrated extraction electrode

The decrease in printing time is a favourable outcome, but the primary incentive for transitioning to IP-Q was the increased structure height that could be achieved. Considering IP-Q, we developed and constructed an integrated extraction electrode for the emitter arrays. The integration of the electrode into the emitter design presents numerous advantages, such as enhancing the alignment accuracy between the emitter orifice and electrode, thus lessening the intercepted ion current. 3D printing the electrode further reduces fabrication errors. Such errors can result in differences in the extraction behaviour of emitters, due to the interaction of the emitters with the electrode. The compact design itself is another benefit, as the integrated electrode requires far less support material. The 3D lithography method ensures a manufacturing of multiple extraction electrodes that are nearly identical in size and shape and offers high flexibility to adapt the design of the electrode in any desired way.

One option for integration involves incorporating the electrode into the emitter array's design and printing them together in a single fabrication step. This approach yields optimal alignment and structural integrity at the cost of flexibility. Another consideration here is the metallization of the electrode. As the base material is the insulating IP-Q polymer, a secondary metallization process is necessary to produce a functional electrode. Directly printing the electrode onto the array can complicate this process. An alternative approach is to create a modular electrode that can be added to the emitter in a subsequent step. We chose this option because it is easier to incorporate into our current design and offers more flexibility.

In Fig. 2, a scanning electron microscope (SEM) image depicts the electrode mounted on an emitter. The image shows the design we developed for the electrode, which comprises three parts: the bottom layer, placed atop the emitter; several pillars, creating the

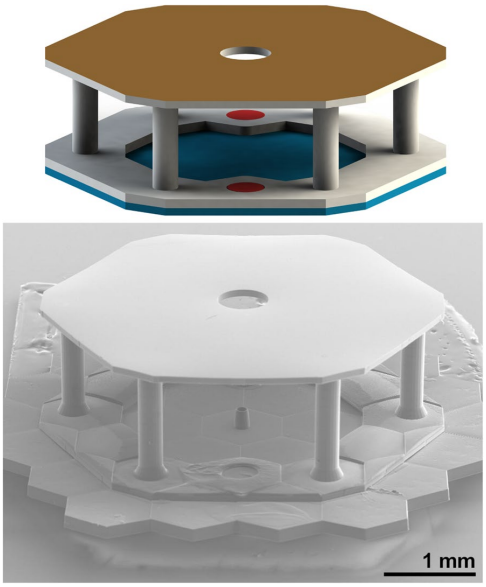

Fig. 2 A 3D rendering of the electrode structure and a scanning electron microscope (SEM) image depicting an emitter with the newly developed integrated extraction electrode. The 3D rendering is based on the same schematic used to fabricate the presented electrode, but does not include any emitter structure. In the rendering, the emitter base (blue), the alignment cones (red), and the electrode structure (white) are highlighted. The modular electrode is composed of the bottom layer, the spacer layer and the top layer which holds the metal film (yellow) that acts as the extraction electrode for the emitters. The SEM image gives an isometric view of the emitter-electrode pair based of the schematic presented above, revealing the electrode's placement on the emitter surface. In the forefront is one of two alignment cones visible that are affixed within the base of the electrode. The minor distortion adjacent to the cone is a result of the adhesive resin employed to fasten the electrode to the emitter

space between the emitter and the top layer; and the top layer, which carries the metal part of the electrode. Each layer is described in more detail below, starting with the top layer.

The top layer is 75 μm thick and contains emission apertures, with each aperture having a 500 μm diameter and centred on an emitter position. The number of apertures can be customized as per user requirements. Figure 3 depicts a single aperture, while Fig. 4 exhibits a design with seven apertures. The layer itself is composed of IP-Q polymer and is non-conductive; therefore, the top of the electrode needs to be metallized. Metallisation is carried out after the printing of the whole electrode structure and is done using a thermal evaporation apparatus. Such a device is advantageous for metallizing as it solely coats one side with metal, keeping the other sides essentially metal-free which evades short circuits.

This method is commonly used in semiconductor manufacturing to apply metal coatings to microelectronic wafers. A piece of the chosen metal is placed in a tungsten carrier and heated under vacuum conditions until it evaporates, releasing metal vapour into the surrounding. The metal vapour's origin is positioned at such a distance from the structure that the particle flux can be assumed parallel when it reaches the sample, where it solidifies on the sample surface. The deposition produces

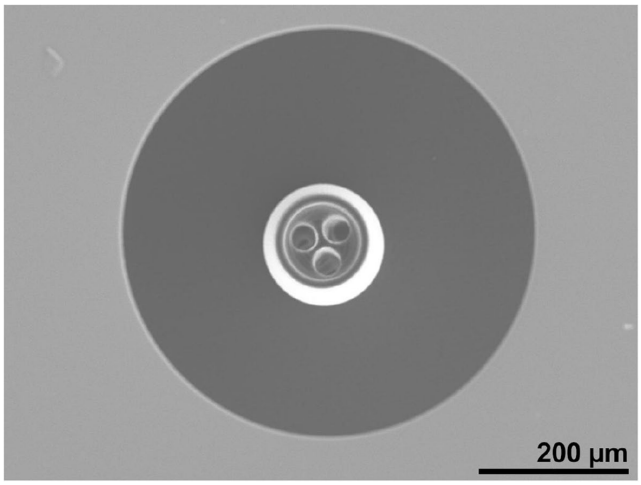

Fig. 3 Scanning electron microscope image giving a top-down view of the emitter and the electrode aperture with a highly aligned appearance. The emitter, in this case a three-capillary design, is centred on the aperture with very little divergence from the center position

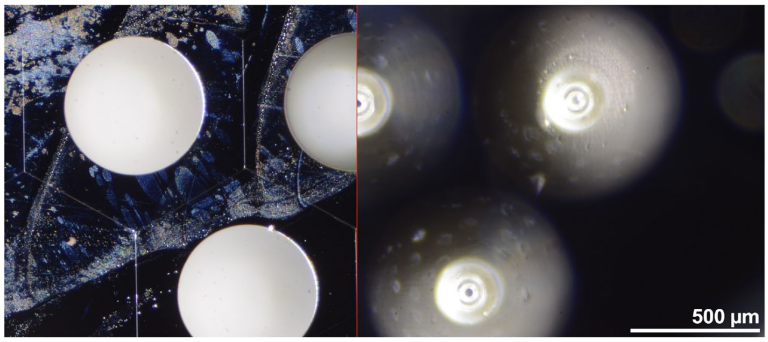

Fig. 4 The two optical microscope images depict the same emitter array with an integrated electrode. The images were taken without moving the sample and only adjusting the focal plane. For clarity, the two images are superimposed on top of each other, displaying only a portion of each image. In the left section of the image, the surface of a metallized electrode is in the focal plane, and the aperture through which ions exit the thruster is prominently visible. In the right portion of the image, the emitter tips are situated in the focal plane. Small black dots in the center of the emitter tip indicate the visible capillary openings. The near-perfect alignment between the emitter and the electrode is observable due to the stacking of the two images. The capillary orifice is precisely centered on the electrode aperture

a shadow-casting effect similar to a light source, resulting in only the surface facing the vapour's origin being coated. This is one reason why a modular system was chosen, because with a modular design it is possible to coat the electrode structure separately, thus avoiding an unintentional coating of the emitters through the extractor holes. Such a metal coating on the emitters may affect their wetting behaviour and increase the chance of propellant overflow to the surface or short circuits due to the conductive metal layer. Another factor to consider is the slight variation in the

thickness of the metal coating. While these variations are negligible in case of the extraction electrode since they are very small compared to the distance to the emitter, they may result in significant variations in wetting behaviour and interaction with the liquid propellant near the emitter making the emitters less comparable even within the same production batch. Masking the emitters under the extractor to avoid uncontrolled coating would be a significant challenge, but the modular design circumvents this challenge. For enhancing the metal's adherence to the polymer, we initially incorporate a thin layer of chromium measuring 2-5 nm, succeeded by a silver layer measuring 150-250 nm. The metal layer is sufficiently thick to cover the entire surface, and the high conductivity of silver guarantees a uniform electrical field.

The spacer layer is the second layer that provides mechanical stability and secures the metallized layer in place. It comprises several round pillars with a 300 μm diameter, ensuring the necessary stability while enabling nearly unobstructed observation of the emitter. Although the stability could be enhanced by using full walls, we opted for a visually open design. The visual open design was chosen for the in-situ observations. Full walls would indeed increase the mechanical stability, however, would also block any view to the emitter structures. For a finalised design a full wall adaptation would surely be beneficial. The added mechanical resilience would be useful for the strong forces and vibrations on launcher start. The height of the pillar can be adjusted to determine the distance between the emitter tip and metal electrode. This flexibility in height allows for customization of the electrical field distribution between the emitters and electrode, and the maximum extraction voltage, to meet the specific needs of the application.

The bottom layer serves as the connection point between the emitter and the electrode, determining their alignment. For optimal alignment, we have incorporated a self-aligning feature consisting of two conical markers printed on the emitter array surface. These markers are added after the printing of the emitter structure and possess no impact on the emitters themselves. There are two openings in the bottom layer of the electrode that securely fit onto the surface markings of the emitter, which makes the integration process straightforward, resembling the use of building blocks. The conical shape of the markers and the extremely precise tolerances result in a perfect alignment of the electrode with the emitters, as shown in Figs. 3 and 4. These images illustrate the exceptional level of alignment attainable at an individual scale, however, the moment, we do not have enough data for providing meaningful statistical data concerning the coaxiality deviation after assembling extraction electrode and emitter structure. For a more detailed image of the alignment we refer to Fig. 10 in the Appendix.

The design of the extraction electrode is completely modular and can be applied to any of our manufactured emitter arrays. It provides a wide range of options, thanks to its adjustable number of apertures, aperture diameters, and height, for matching the electrode design to the emitter array or specific applications. Alignment of the openings to the emitters is ensured by the conical indicators and can be accurately replicated. In addition, the ability to observe the emitters during operation is facilitated by the high visibility in the space between the emitter and electrode. Furthermore, the electrode design is not directly linked to the emitter design, indicating its suitability also for externally wetted or porous type emitters. With its modular design it can be easily adapted to other types of electrospray thrusters.

In situ microscopical optical observation

Miniaturization is advantageous for electrospray thrusters, as previously stated [5]. Nevertheless, this creates challenges in characterizing the fabricated emitters. Due to their small size and the vacuum environment in which they are tested, standard optical observation is not always feasible for gaining insight into functionality and extraction behaviour on a microscopic scale. There are numerous variables that may influence emitter emission behaviour, such as extraction voltage, feed rate for actively fed systems, emitter geometry, and electrode spacing, among others. Determining the influence of emitter design is particularly difficult by electrical characterization alone.

For better understanding of the interplay between variables, we will be employing two optical cameras. One camera, a basic optical USB camera with adjustable focus, is employed to capture real-time footage of the entire emitter stack. Its purpose is to record the fluid intake and the interaction between extracted ions and the electrode as a whole. The second camera is a high-resolution black and white camera with an interchangeable adapter for a microscope objective. We can fit objectives that magnify 5× to 50× on the camera to focus on specific parts of the emitter. Using 10× magnification, we can observe multiple emitters of the array while still being able to resolve the emitter tip with the extraction site. With this dual camera set-up, we can observe the emitter stack at both macro and micro levels in real-time. This facilitates correlation of optical data obtained from the cameras with the emission data obtained from electrical characterization. One significant benefit of utilizing a camera set-up with capillary-type emitters is the ability to observe the microfluidic behaviour of capillaries. As fluidic resistance presents a major challenge for capillary-type emitters, observing capillarity in situ helps significantly in designing the emitters to meet desired parameters. Moreover, these capabilities are not limited to capillary-type emitters exclusively. For example real-time optical observation can assist in pinpointing the root causes of secondary emission site formation between emitters or the interaction between the fluid and the electrode in external wetted designs. This type of observational method has numerous applications, beside the already discussed ones.

Active fluid feeding under vacuum conditions

To achieve a representative simulation of space-like conditions, we utilize a vacuum chamber to test the emitter arrays. However, the fluid supply under such conditions present a significant challenge. Various methods exist for vacuum liquid propellant feeding. One such method involves utilizing capillary forces in porous materials to passively pull liquid from a reservoir to the extraction sites [13, 19]. Passively-fed systems are low in complexity and contain no moving parts. The material's self-regulation is due to capillary forces that contain the propellant. However, it does not provide control over fluid intake and distribution. It was reported, that the thruster performance correlates with the reservoir fill levels, resulting in loss of performance over time with less liquid remaining inside the tank [19]. Additionally, manufacturing the emitters to achieve equal liquid distribution along the emitter array is complex and costly. Unequal distribution would also negatively impact the performance [19].

One way to actively control fluid feeding is by using a gas-powered system. The system includes a reservoir with one open side that is placed in a pressure container, which

can be evacuated or flooded with a gas. A capillary is connected to another side of the reservoir, leading to the electrospray thruster [20–22]. The pressure inside the container can be controlled to regulate the fluid's flow rate into the capillary. Though effective, this method is complex. The regulation of pressure must be exact requiring high pumping power for rapid pressure relief. Additionally, precise control of the gas used to increase the pressure is required [20]. A further concern is the potential for gas to dissolve into the liquid and degas inside the thruster later on.

A second means of precisely managing flow rate is utilizing a precision pump. We already have successfully utilized this methods in the past, achieving favourable outcomes [14, 16, 17]. Utilizing a high-precision syringe pump enables us to effectively regulate the input rate via pump throttling. We can calibrate the flow rate, which corresponds to the pump throttle, using a mass flow meter. This guarantees that the appropriate amount of fluid is delivered to the emitter, providing full control over the feeding process. However, there remains a pressure difference issue when the pump holding the syringe is at ambient pressure. A minor leak of fluid from the outside into the emitter due to this pressure difference was detectable by the mass flow meter. To address this issue, a shut-off valve was utilized. Another issue that arose over time was the accumulation of air in the system, despite the use of gas-tight fittings and syringes. This led to spontaneous degassing within our emitter arrays, which disrupted testing. Therefore, we adapted our pump to function under vacuum conditions and relocated the entire feeding system to the inside of the vacuum chamber. A schematic diagram of the modified arrangement is presented in Fig. 5. A second modification was made to the syringe in order to allow gas to escape during vacuum chamber evacuation.

This involved shortening the syringe to enable complete plunger extraction during pump down, which exposes the fluid inside the syringe to the chamber. Once a pressure of less than $1 \cdot 10^{-4}$ Pa was reached, the plunger could be pushed back into the syringe, effectively sealing it. A special guiding attachment ensures correct plunger insertion. This arrangement allows for precise feeding rate control during operation, while also guaranteeing that no gas is fed to the emitter.

Results

Optical images and videos of emitter operation and in-situ observation as well as emission data are presented. In all experiments, the electrode is grounded and then either a positive or negative high voltage is applied to the ionic liquid, 1-ethyl-3-methylimidazolium tetrafluoroborate (EMIM-BF_4). All data including the video files and the corresponding extraction data, is available according to the FAIR regulations in our data repository [23]. The data presented here is for three emitter designs with different geometries. The individual characteristics of each design can be found in Table 1 and are further discussed in more detail in the corresponding section. For each design, a 3D render showing a cross-section of the capillary structure is available in our data repository [23].

The emitter designs and the corresponding data presented here were chosen from multiple experiments conducted on samples with similar or identical geometries. All results are reproducible for emitters of identical capillary configuration and of each design.

Figure 6 displays multiple images captured from a video segment spanning approximately one second in time as well as the correlating emission data. The three optical

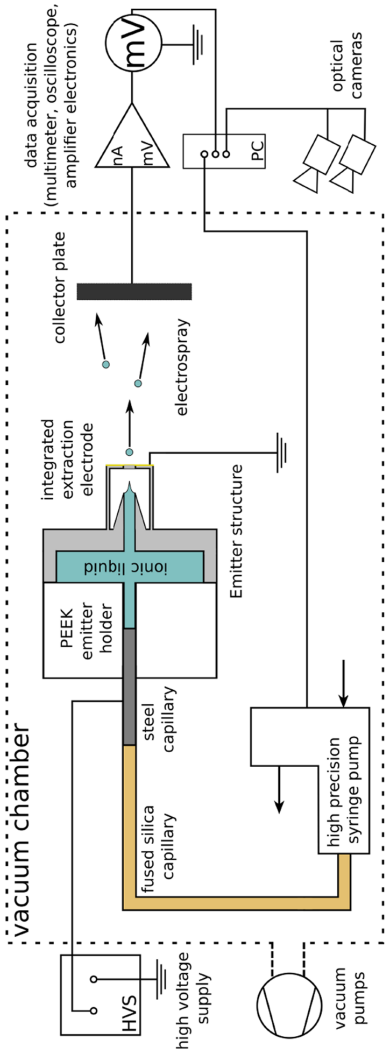

Fig. 5 Schematic diagram of the measurement setup used. The setup resembles the one reported earlier [17], but with a few adjustments. The lower right portion of the diagram illustrates the recently integrated optical observation with two cameras. Furthermore, the fluid feeding system, including the tubing and pump, has been placed inside the vacuum chamber, hence is exposed to the vacuum

Table 1 Design parameters for the presented emitter structures

	Capillary type	Capillary length	Capillary diameter	Special notes
Design 1	straight circular	100 µm	20 µm	conical opening at
		200 µm	max. 40 µm	the emitter tip
Design 2	straight circular	300 µm	30 µm	
Design 3	straight rectangular	300 µm	15 µm×30 µm	five capillaries

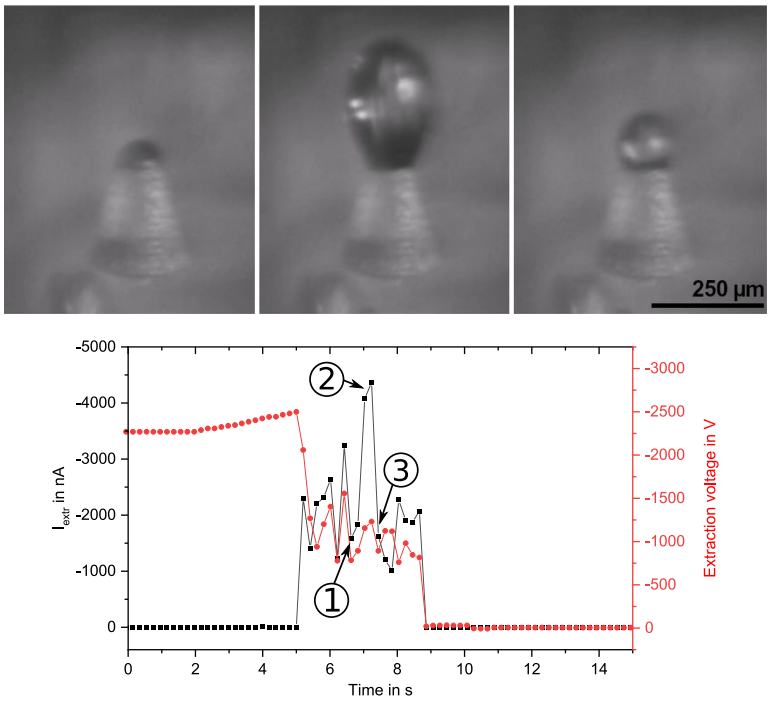

Fig. 6 Three optical images captured from a live video of an emitter array as well as the correlating emission data is shown. The pictures are arranged in chronological order, with the first one being on the left and the latest on the right. The time elapsed between the left and right image is estimated to be about one second. For this emitter, we opted for a design featuring a straight capillary that opens conically at the tip. The diameter measures 20 µm at the narrowest point and 40 µm at the tip. The image on the left depicts the droplet formation on the emitter tip while the capillary in the center of the emitter supplies the required fluid. In the middle image, the droplet is drawn towards the integrated extraction electrode while remaining connected to the emitter, taking on a raindrop-like shape. The right image depicts the same droplet, which has now significantly reduced in size and returned to the emitter tip, forming a spherical shape. Below the optical images the correlating emission data is plotted. On the horizontal axis is shown the time, which was normalized to improve the readability of the time frame of the extraction event. The time origin was arbitrarily chosen to fit the image data and set to 0 for visualisation reasons. The applied high voltage (red dots) and the converted extraction current (black squares) are plotted on the Y-axis. The emission correlating the images is represented by the numbers plotted into the graph, with 1 corresponding the left most picture and 3 to the right one

images are arranged in chronological order from left to right. The images show a single emitter of an emitter array, which features a straight, round capillary with a diameter of 20 μm and which opens conically at the tip to a diameter of 40 μm. The conical opening at the tip allows fluid to build up in this area.

The capillary's length totals 300 μm with 100 μm having a diameter of 20 μm. The correlating electrical emission data taken at the same time frame is plotted below the images. In the graph the extraction voltage and collected currents are plotted versus time. For visibly reasons the staring time was arbitrarily set to 0. The data shown confirms an extraction event happening in the time frame depicted by the optical images. During the experiment, a voltage was applied once a droplet was observed at the emitter tip. The point in time when the voltage was first applied lies outside the presented time frame. Slow, incremental increases in voltage were made until extraction was detected. This process took place over several minutes to allow the system to adjust accordingly. At the 2-second mark, a new voltage target was set, and the extraction voltage was slowly increased to reach the new target. For this experiment a negative voltage was applied to the ionic liquid. The extractor electrode and collector plate were at ground potential.

From the left to the right, one can see the formation of a small droplet in the cone shaped tip of the emitter. It is not visibly deformed and sits close to the tip. In the middle image, the droplet is significantly enlarged and seems to be drawn towards the extraction electrode. Compared to the previous image, the droplet has greatly increased in volume, and a significant portion of the fluid is suspended in the vacuum above the tip, while only a small part remains attached to the emitter. The droplet then returns to a smaller size, comparable to the droplet seen in the first image. This change can be observed in the right picture. However, there is still an apparent attraction exerted on the droplet, as it maintains a spherical shape rather than collapsing into a meniscus. The numbers plotted in the bottom section of Fig. 6 correlate with the chronological order of optical images with 1 denoting the left picture and 3 the right. The three images only capture a brief interval of the complete extraction process while the extraction data gives a complete overview of the extraction event spanning over seven seconds. The extraction

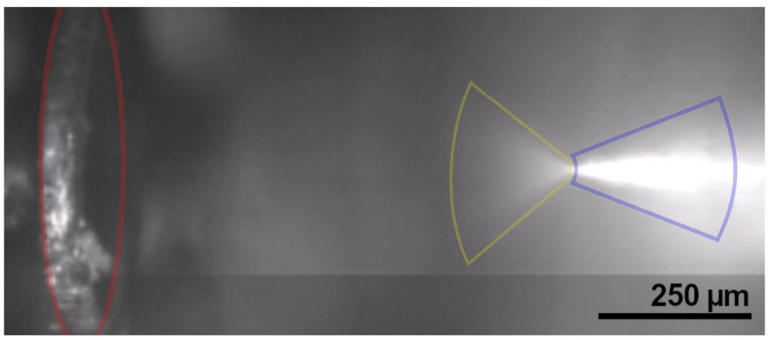

Fig. 7 One optical image obtained from live footage of an emitter array and the correlation extraction data. The integrated extraction electrode (marked in red) is visible on the left side and an emitter (marked in blue) in the right portion, which features a straight capillary with a diameter of 30 μm and a length of 300 μm. The image portrays the extraction of EMIM-BF_4 from the tip of the same emitter in the form of a fine spray (marked in yellow)

event was ultimately terminated when the ionic liquid overflowed onto the emitter surface, which was accompanied by multiple arc hits on the emitters.

The second dataset consists of a single optical image extracted from live footage. This picture shows a fine mist being extracted from an emitter, displayed in Fig. 7. The emitter on the right produces an ion spray aimed at the extraction electrode situated on the left side of the image. For this experiment we utilized an emitter featuring a straight capillary with a fixed diameter of 30 μm and a length of 300 μm. The emission data that was collected is not available due to a device error in the amplifier electronics. The high currents from the extraction event caused a safety shut-down of the amplifier. The emission was terminated by violent arcing which caused damage to the emitter. We believe that the reason for the termination in this case was a combination of the significant currents, the clearly visible spray in Fig. 7, and too high extraction voltages. This combination most likely caused the arcing we observed.

The last dataset consists of one optical image and the correlation emission data of the extraction event. The optical image in Fig. 8 displays an emitter and extraction electrode on the right and left, respectively. The emitter design incorporates five rectangular capillaries arranged in a star shape pattern. Each capillary has dimensions of 15 μm x 30 μm x 300 μm for length, width, and height, respectively. The image shows a fully formed Taylor-cone.

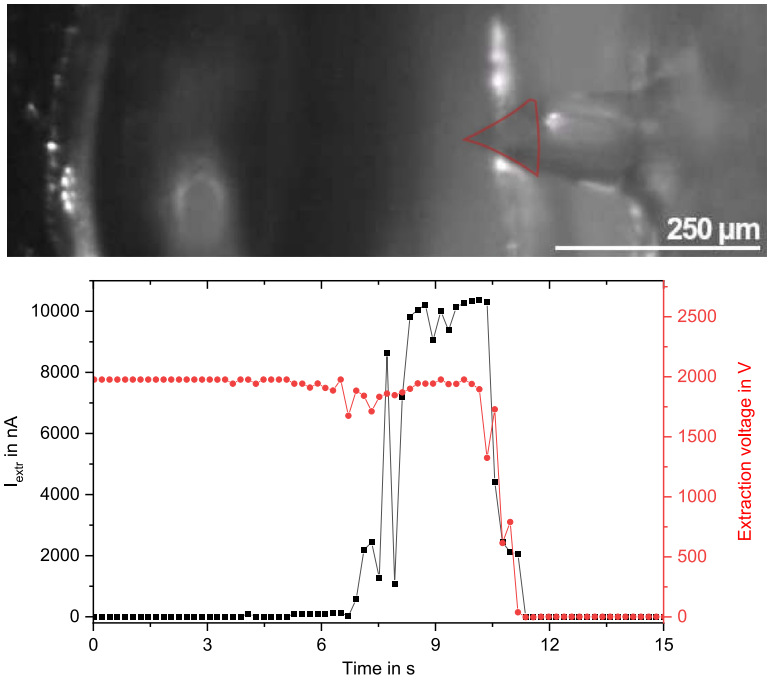

Fig. 8 An optical image captured from a live video of an emitter array, which shows an emitter and an extraction electrode aperture. The emitter consists of five rectangular capillaries arranged in a star pattern, each measuring 15 μm x 30 μm . The image displays a fully formed Taylor-cone positioned over the one of the emitters and oriented towards the extraction electrode. For better visualisation the outline of the Taylor-cone was retraced by a red line. Additionally, the Taylor-cone is observed to be centred to the electrode aperture. In the bottom half the extraction data is presented, with the normalized time plotted on the X-axis and the applied high voltage and the converted extraction current plotted on the Y-axis

For visibility purposes the outline of the Taylor-cone was enhanced with an red line in Fig. 8. The Taylor-cone in the image is positioned on the emitter such that it points directly at the extraction electrode. A slight reflection at the edge of the emitter tip reveals the bottom part of the Taylor-cone. Figure 8 also shows the correlated electrical emission data. Similar to the other experiments the extraction voltage was applied once the presence of fluid in the reservoir behind the emitter was confirmed in the camera image. The voltage was then slowly raised over the span of several minutes and after each incremental increase the system was given time to adjust to the new voltage. During this experiment a positive voltage was applied to the ionic liquid. The extractor electrode and collector plate were both at ground potential. The extraction event plotted in Fig. 8 took place in the adjustment process. The image shown in Fig. 8 can be placed around the nine second mark. The data exhibits very high emission with a maximum of 10 μA, which remains relatively stable from eight seconds to ten seconds. The extraction voltage is also stable at approximately 1.7 kV during this period. After ten seconds of emission, instability occurred which resulted in an arcing. This is reflected by the fluctuations observed in the high voltage and the exaction current.

Discussion

From the data obtained we can identify different extraction behaviour for the three emitter designs. The images and data in Fig. 6 strongly imply a droplet extraction mode featuring large droplets. This can also be seen in the emission data plotted in Fig. 6, which shows multiple peaks. It can be inferred from the images that significant portions of the droplet are detached during the process of being attracted towards the electrode. After losing a considerable amount of volume, the droplet descends back towards the emitter, possibly due to an imbalance of positive and negative ions within the fluid. This may also account for the reduced attraction observed following the droplet's split. Subsequently, new negative ions are attracted through the capillary, resulting in the formation of a new, large droplet. The video demonstrates the repetition of the cycle depicted in the three images. The extraction was stopped after a significant amount of fluid overspilled onto the surface of the emitter structure, wetting the complete space between the individual emitters. The observed behaviour suggests that the fluid resistance of the design presented, is still too low which is very likely also the cause of the overflow. The capillary is capable of drawing a significant amount of fluid in a short period of time, which favours droplet formation. Another inference can be made in regard to the design featuring a conical opening at its tip. Its intended purpose was the creation of a buffer zone for the fluid, thus reducing the chance of overspilling. However, it appears to have a detrimental effect on extraction behaviour since it promotes droplet formation at the tip. A notable observation can be made from the correlated video and emission data. The droplets appear to have significant mass but low charge. The level of extraction current in the emission data in Fig. 6 does not match the mass loss of the droplet. This phenomenon may be explained by the size of the droplet, which likely contains nearly equal amounts of negative and positive ions, with one type being slightly more dominant. As a result, there is enough attraction towards the electrode, but the measured currents are low. From the observations, one can gain significant insight into the interaction between the ionic liquid, emitter, and electrical field. The influence of the emitter design is also apparent from the images and the emission data. Unrelated to the emitter

design, the image sequence proves that the integrated electrode design is working as intended. The droplet is pulled towards the electrode aperture and shows very little tilt. This indicates a stable and well defined electrical field between emitter and electrode. Furthermore, the droplets are able to exit the emitter stack and reach the detector plate.

This influence is also evident in Fig. 7. The emitters implement a revised design that omits the conical buffer zone at the tip. A comparison of the emission behaviour depicted in Figs. 6 and 7 reveals the effect. The latest design shown in Fig. 7 does not exhibit droplet extraction, but instead shows a fine spray. This spray is indicative of a fine droplet emission or even purely ionic emission. Further validation of the emission data is necessary. As previously described, data collection was unsuccessful due to over-current in the amplifier electronics. However, the high currents, which are typical for pure ionic extraction, support this interpretation. This image also demonstrates the successful application of the recently developed electrode design. The spray pattern visible at the emitter tip exhibits symmetrical behaviour towards the aperture and points precisely at the opening. This observation further strengthens our hypothesis about the electric field distribution between the emitter and the electrode. Additionally, substantial currents were able to exit the electrode and reach the detector, even overpowering the electronics. The picture suggests a need for further investigation of the influence of the capillary on the emission. A white flash seen inside the emitter prompts uncertainty whether it reflects light from another emitter or if the spray is generated inside the capillary and, thus, glows. The implications for the design and the thruster as a whole are significant, depending on the circumstances.

As evidenced by the preceding images, Fig. 8 shows a clear Taylor-cone and confirms again the successful implementation of the electrode design. In this case, the ionic liquid is also pulled toward the electrode, even forming a complete Taylor-cone. The accompanying emission data corroborates this, as a substantial current was collected during cone formation.

As stated in "Results" section, the emission was terminated by instabilities which resulted in arcing. We hypothesise from the image data captured, that in this case too much fluid was pulled from the reservoir and caused an overflow. The extraction data also suggest that the Taylor cone collapsed rather spontaneously, thus terminating the extraction. Another explanation could be residual gas inside the reservoir which exited the array through one of the emitters. While rare, we observed that some gas may be captured inside the reservoir and may be extracted by the moving fluid. A spontaneous decompression of the gas could also lead to a collapse of the Taylor cone and cause arcing.

The data shown in Fig. 8 serves as an example of fluid-induced start-up, where voltage is applied before the fluid can reach the emitter tip. Investigations of fluid-induced versus voltage-induced start-ups reveal significant differences [24]. In certain situations, one method of starting a the thruster may be more advantageous than the other. Another important factor to consider is the design of the emitter. The rectangular capillary approach was used in this case, which is exclusive to this manufacturing method. This highlights the importance of innovative thinking when designing emitters. Exploring the various shapes and design features possible through 3D lithography could lead to unforeseen outcomes and benefits.

Conclusion

We introduced a completely modular design for extraction electrodes and its manufacturing process, which can be personalized to fulfil the requirements of the users while remaining compatible with any electrospray emitter. Moreover, we displayed the self-aligning ability of our design and demonstrated its implementation and integration into our electrospray emitter arrays through SEM and optical images. Additionally, we presented a new technique for acquiring in-situ video data of electrospray emitters and showcased the outcomes. We modified and created various emitter designs that utilized the IP-Q resin. These emitters were then subject to characterization by using optical videos and electrical emission data. Although emission behaviour remains unsteady, we are optimistic that stable emission will be achieved by refining our techniques in accordance with the IP-Q material system and adjusting the emitter designs. Once stable emission is confirmed, time-of-flight data will be collected to analyse the performance of the thruster. We also want to investigate the influence of different ionic liquids on the emission behaviour.

Appendix A Additional figures

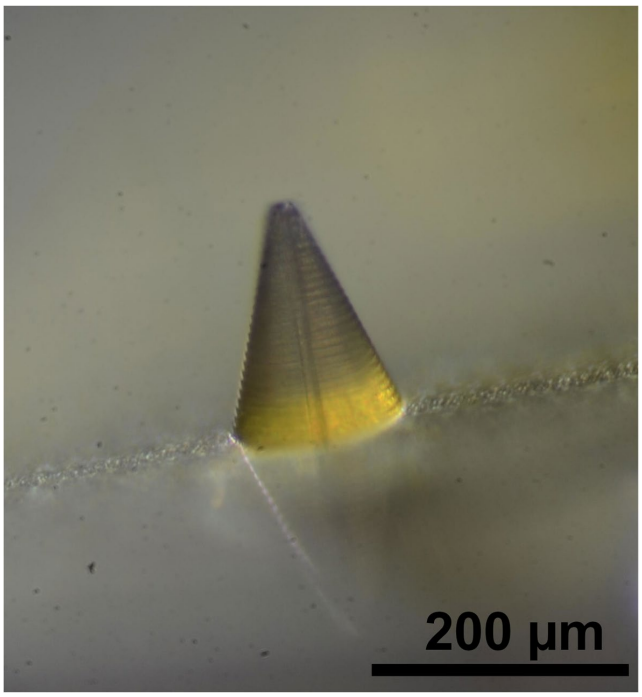

Fig. 9 A microscope image of an IP-Q emitter. The emitter features a 10 µm capillray diameter over a hight of 300 µm. The lower part of the emitter is obscured by the emitter base and only a 200 µm secton of the capillary is visible

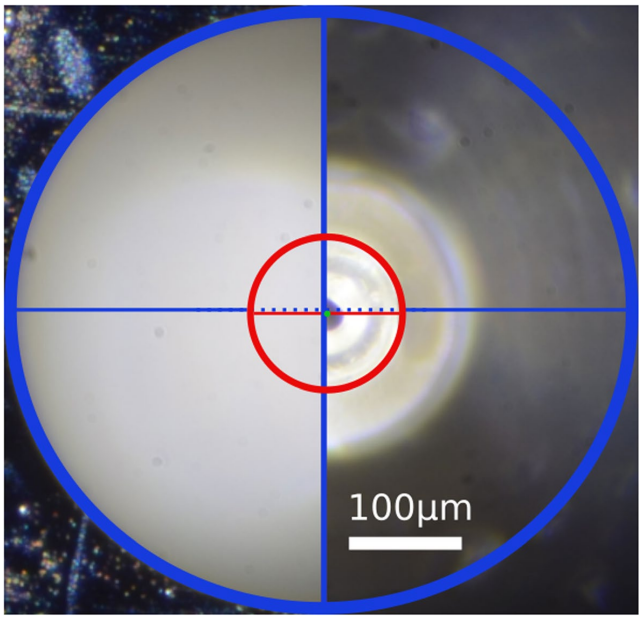

Fig. 10 Supplementary for Fig. 4. The picture shows a magnified section of the microscope image presented in Fig. 4 with additional markings. The blue cross-hair is aligned to the extractor orifice and the red cross-hair to the emitter structure. The small green dot in the center of the image marks the center of the capillary opening. From this picture the alignment quality of the emitter-extractor combination can be determined. The deviation of the center of the capillary from the center of the extractor orifice measures approximately 5 µm

Acknowledgements
The authors gratefully acknowledge funding by the German Federal Ministry for Economic Affairs and Climate Action under the contract (FKZ) 50RS2203.

Authors' contributions
F.L.K. collected the data used for the manuscript, wrote the main manuscript, prepared the figures. P.J.K. and T.H. acquired funding and supervised the project. All authors reviewed the manuscript.

Funding
Open Access funding enabled and organized by Projekt DEAL. The research leading to this work was funded by the German Federal Ministry for Economic Affairs and Climate Action under the contract (FKZ) 50RS2203.

Availability of data and materials
All data is publicly available under the FAIR regulations for data availability [23].

Code availability
Not applicable.

Declarations

Competing interests
The authors declare no competing interests.

Received: 27 September 2023 Accepted: 27 December 2023
Published online: 12 January 2024

References

1. Lozano PC, Martínez-Sánchez M, Hruby V (2010). Electrospray Propulsion. https://doi.org/10.1002/9780470686652.eae121
2. Lemmer K (2017) Propulsion for CubeSats. Acta Astronautica 134:231–243. https://doi.org/10.1016/j.actaastro.2017.01.048
3. Holste K, Dietz P, Scharmann S, Keil K, Henning T, Zschätzsch D, Reitemeyer M, Nauschütt B, Kiefer F, Kunze F, Zorn J, Heiliger C, Joshi N, Probst U, Thüringer R, Volkmar C, Packan D, Peterschmitt S, Brinkmann KT, Zaunick HG, Thoma MH, Kretschmer M, Leiter HJ, Schippers S, Hannemann K, Klar PJ (2020) Ion thrusters for electric propulsion: scientific issues developing a niche technology into a game changer. Rev Sci Instrum 91(6):061101. https://doi.org/10.1063/5.0010134
4. Lev D, Myers RM, Lemmer KM, Kolbeck J, Koizumi H, Polzin K (2019) The technological and commercial expansion of electric propulsion. Acta Astronautica 159:213–227. https://doi.org/10.1016/j.actaastro.2019.03.058
5. Gomez Jenkins M, Krejci D, Lozano P (2018) Cubesat constellation management using ionic liquid electrospray propulsion. Acta Astronautica 151:243–252. https://doi.org/10.1016/j.actaastro.2018.06.007
6. Taylor GI (1964) Disintegration of water drops in an electric field. Proc R Soc Lond Ser A Math Phys Sci 280(1382):383–397. https://doi.org/10.1098/rspa.1964.0151
7. Liu X, Deng H, Sun Y, Kang X (2022) Simulation of liquid meniscus formation in the ionic liquid electrospray process. Plasma Sci Technol 24(7):074008. https://doi.org/10.1088/2058-6272/ac61c0
8. Krejci D, Reissner A, Seifert B, Jelem D, Hörbe T, Plesescu F et al (2018) Demonstration of the ifm nano feep thruster in low earth orbit. In: 4S Symposium, Sorrento, Italy. https://www.researchgate.net/publication/325486881. Accessed 20 Sept 2023
9. Holbrey J, Seddon K (1999) Ionic liquids. Clean Prod Process 1:223–236. https://doi.org/10.1007/s100980050036
10. Rebelo LPN, Canongia Lopes JN, Esperança JMSS, Filipe E (2005) On the critical temperature, normal boiling point, and vapor pressure of ionic liquids. J Phys Chem B 109(13):6040–6043. https://doi.org/10.1021/jp050430h. PMID: 16851662
11. Chiu YH, Dressler R (2007) Ionic Liquids for Space Propulsion, vol 975. pp 138–160. https://doi.org/10.1021/bk-2007-0975.ch010
12. Guo Y, Sun W, Sun Z, Wu Z, He J, Yang C, Wang N (2023) Direct thrust test and asymmetric performance of porous ionic liquid electrospray thruster. Chin J Aeronaut 36(4):120–133. https://doi.org/10.1016/j.cja.2022.09.007
13. Peter BS, Dressler RA, Chiu Yh, Fedkiw T (2020) Electrospray propulsion engineering toolkit (ESPET). Aerospace 7(7). https://doi.org/10.3390/aerospace7070091
14. Kunze FL, Henning T, Klar PJ (2021) Taking internally wetted capillary electrospray emitters to the sub-ten-micrometer scale with 3D microlithography. AIP Adv 11(10):105315. https://doi.org/10.1063/5.0066619
15. Harinarayana V, Shin Y (2021) Two-photon lithography for three-dimensional fabrication in micro/nanoscale regime: a comprehensive review. Opt Laser Technol 142:107180. https://doi.org/10.1016/j.optlastec.2021.107180
16. Kunze FL, Henning T, Klar PJ (2022a) Validation of pure SU-8 micro 3D printed internally wetted capillary type electrospray mircoemitters for thruster applications. 8th internatinonal conference on space propulsion, Estoril (SP2022-082)
17. Kunze FL, Henning T, Klar PJ (2022b) 3D micro printed internally wetted capillary type electrospray emitters on the single micrometer scale. 37th International Electric Propulsion Conference (IEPC), Boston (IEPC-2022-175)
18. Gustan-Gutierrez E, Gamero-Castaño M (2017) Microfabricated electrospray thruster array with high hydraulic resistance channels. J Propuls Power 33(4):984–991. https://doi.org/10.2514/1.B36268
19. Chen C, Chen M, Zhou H (2020) Characterization of an ionic liquid electrospray thruster with a porous ceramic emitter. Plasma Sci Technol 22(9):094009. https://doi.org/10.1088/2058-6272/ab9528
20. Ma C, Messina V, Ryan C, Rovey JL, Putnam ZR, Lembeck MF et al (2022) Emission characterization of porous electrospray thrusters with actively controlled flow rate. https://eprints.soton.ac.uk/474346/. Accessed 14 Sept 2023
21. Demmons NR, Wood Z, Alvarez N (2019) Characterization of a high thrust, pressure-fed electrospray thruster for precision attitude control applications. AIAA 2019–3817. https://doi.org/10.2514/6.2019-3817
22. Zhang K, Kuang S, Suo X, Huang X, Li Z, Wang D, Jia H, Tu L, Song P (2022) Analysis of beam currents under an oscillating cone-jet mode for developing high-precision electrospray thrusters. J Appl Phys 131(9):094501. https://doi.org/10.1063/5.0083210. https://pubs.aip.org/aip/jap/article-pdf/doi/10.1063/5.0083210/16505945/094501_1_online.pdf
23. Kunze FL (2023) Data for '3D micro printed capillary electrospray thruster with a fully modular integrated extraction electrode'. JLUpub. https://doi.org/10.22029/jlupub-17893
24. Uchizono NM, Collins AL, Thuppul A, Wright PL, Eckhardt DQ, Ziemer J, Wirz RE (2020) Emission modes in electrospray thrusters operating with high conductivity ionic liquids. Aerospace 7(10). https://doi.org/10.3390/aerospace7100141

Publisher's Note

3.5 Publication V: Space Propulsion Conference 2024

This publication represents a minor milestone in the design and fabrication of the modular extractor electrode. Notable enhancements were implemented to the electrode's structural framework. The electrode was divided into three distinct modular components. This permits additional modularity and freedom during the assembly of the electrospray thruster. The electrode carrier, which serves as the electrically active component, can now be coated with additional metals or via sputter coating technology. This provides greater flexibility in the selection of coatings and simplifies the metallisation process. This is made possible by the introduction of the micro-click connector. The aforementioned connectors facilitate friction-fit assembly of the entire thruster head, obviating the necessity for adhesives. The self-aligning feature improves the precision of the assembly process by enabling the different parts to be clicked together. In conclusion, the enhancements to the extractor design facilitate more reproducible assessments of the emitter structures.

F. Kunze wrote the first draft of the manuscript. The manuscript underwent revision by all of the contributing authors. The experiments and data acquisition were conducted by F. Kunze. Furthermore, P. Klar and T. Henning provided supervisory and project management oversight.

DESIGN AND MICRO 3D PRINTING OF ELECTROSPRAY EMITTERS WITH AN INTEGRATED MODULAR EXTRACTION ELECTRODE

Fynn L. Kunze [(1)], Torsten Henning [(1*)], Peter J. Klar [(1)]**

[(1)] Institute of Experimental Physics I,
Justus Liebig University, Giessen, Germany
[(1)] Email: Fynn.Kunze@physik.uni-giessen.de
[(1)] Email: Torsten.Henning@physik.uni-giessen.de*
*[(1**)] Email: Peter.J.Klar@exp1.physik.uni-giessen.de*

KEYWORDS: micropropulsion, electrospray, additive manufacturing, micro fabrication

ABSTRACT:

A design of an integrated extraction electrode for electrospray thrusters is presented. The design features a modular composition and is completely fabricated by additive manufacturing methods. The main components are micro 3D printed using two-photon-laser-lithography, which allows for a high degree of customizability. This design approach can be adopted for any kind of electrospray thruster, including internally wetted, externally wetted and porous emitter types. The very high precision of the manufacturing process also allows for a self-aligning mechanism to improve and insure precise positioning of the electrode above the emitter structures. Alongside the electrode design some emitter designs are presented, as well as preliminary emission data of emitters using the newly developed extraction electrode.

1. INTRODUCTION

Electrospray thrusters, categorized under the electrostatic thruster family [1], hold significant promise for micro propulsion applications such as CubeSats. Their adaptability to scaling down is a primary factor of interest, particularly for micro and nano satellites [2–4]. Unlike traditional electric propulsion systems like Hall thrusters, electrospray thrusters can be downsized with ease and even benefit in terms of performance [5]. Moreover, depending on the system configuration, the need for a neutralizer in the propulsion setup can be eliminated, further reducing power requirements [2]. Their ability to provide precise thrust and impulse bits makes them particularly suitable for high-precision manoeuvres like constellation flight. Additionally, their use of liquid or semi-solid propellants renders them highly manageable during launch and integration, which is appealing especially to commercial applications such as mega constellations [5].

Electrospray thrusters operate by extracting ions or droplets from a liquid propellant via a static electric field. The electric field deforms the fluid, forming a conical shape known as a Taylor-cone as the field strength increases [2, 6]. At the tip of the Taylor-cone, the electric field density is high enough to extract ions or droplets from the propellant, causing them to accelerate along the electric field direction. For proper function, the fluid must either be conductive or possess a polar component such as water [6]. Common propellants for electrospray thrusters include liquid metal or ionic liquids. Liquid metal requires heating to its melting point before use, with indium being a popular choice due to its relatively low melting point of 150°C [7]. On the other hand, ionic liquids, being salts, remain liquid below room temperature, with minimal vapour pressure, making them stable in vacuum conditions [8–10]. Their composition of pure ions results in high electrical conductivity, making them ideal propellants for electrospray thrusters. Furthermore, ionic liquids enable the extraction of both positive and negative ion species, eliminating the need for an external neutraliser.

Typically, an electrospray thruster comprises three main components: the propellant intake, emitter structure, and extraction electrode. The propellant intake, either a tubing system in actively fed thrusters or a reservoir in passively fed systems, provides the necessary propellant for the emitter structure. Once the fluid reaches the emitter structure, it is exposed to an electrical field, facilitating ion extraction. There are three variations of emitter structures, differing in how propellant is supplied to the emission sites, though the general operating principle remains consistent [11]. These variations are porous emitters, externally wetted emitters, and capillary emitters, each presenting unique challenges [11, 12].

In our research, we concentrate on the additive manufacturing of miniaturized capillary-type electrospray thrusters. We employ a micro 3D printing technique based on two-photon lithography to fabricate high aspect ratio capillary emitter structures as well as a newly developed fully modular extraction electrode. We further are branching out to externally wetted designs and 3D printed porous materials.

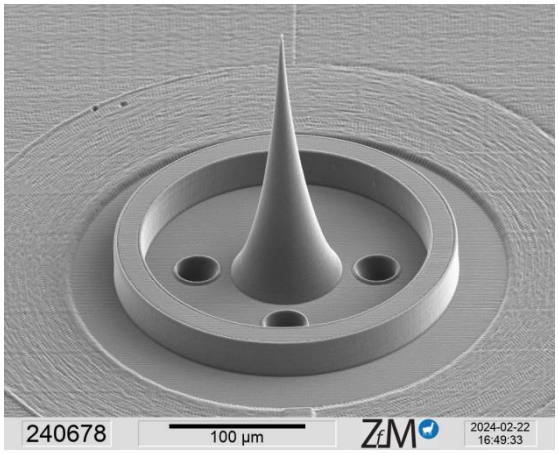

Figure 1. Scanning electron microscope (SEM) image of an externally wetted emitter design. The design features four propellant feeding capillaries (three are visible) and a fluid retention ring around the emitter structure.

2. ADDITIVE MANUFACTURING

For the additive manufacturing we utilise a 3D micro-printing technology based on two-photon-laser-lithography. This method allows the printing of polymer structures with feature sizes down to 100 nm at high speeds and precision [12-14]. Similar to conventional 3D printing this technique inherits the freedom of design to fabricate hollow, under-cut or free floating structures. This sets it apart from the established micro-fabrication technologies used in semiconductor fabrication or micro-machining. A more detailed description of the principle behind this fabrication method can be found in our previous works [13-15].

2.1. New material system IP-Q

In our most recent work we adapted the material IP-Q, a special resin developed by NanoScribe for 3D lithography applications [12]. IP-Q is a suitable replacement for the previously used SU-8 resin, which is known for its mechanical stability, solvent resistance, and durability under space-like conditions [12,13]. We made this change due to the major drawback of SU-8's preparation process, which involves applying it onto a silicon wafer using a spin coater, resulting in thin resist films. The maximum layer thickness achievable with SU-8 is only approximately 400 µm, limiting the height of structures such as emitters.
With the IP-Q resist, which was devolved for NanoScribe's 'large feature solution set', structures up to 10 mm in height can be fabricated, while still offering comparable mechanical and chemical properties to SU-8. It also performs similarly as a base material for microfluidic applications.
However, slight variations in wetting angle and surface properties between IP-Q and SU-8 warrant further investigation for a comprehensive comparison. Furthermore, we need to assess the radiation hardness of IP-Q for future applications. Presently, IP-Q serves as a suitable alternative to

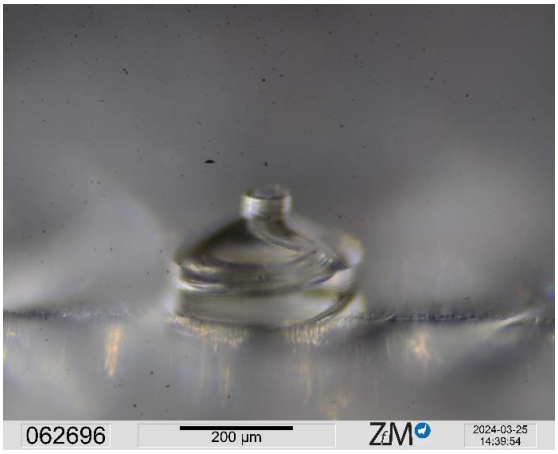

Figure 2. Microscope image of a capillary type emitter with spiral capillary.

SU-8. Another advantage of IP-Q is the significantly faster processing times achieved by using a 10× objective instead of the previously employed 20× objective. This transition has reduced the process time from 12 hours to 4 hours per array. Notably, the higher printing speed is achieved at the expense of increased voxel dimensions. With the 10× objective, the lateral voxel size is approximately 1.5 µm, and the longitudinal size is around 25 µm, representing a fivefold increase in longitudinal size compared to the 20× objective. While this enlargement reduces print resolution slightly, the impact is negligible when considered carefully beforehand. We have succeeded in manufacturing emitters of different types with greater height, capillary length and structural features with IP-Q than possible with SU-8 as base material [12]. Fig. 1 depicts an example of an externally wetted emitter design fabricated by 3D lithography and Fig. 2 shows a capillary type emitter.

2.2. Emitter structures

Fig. 1 and Fig. 2 show structures fabricated by 3D lithography. Fig. 1 especially reveals the high precision which the fabrication method allows, with the very sharp tip in the sub micrometre range.
It allows to fabricate all three common types of emitters, namely externally wetted, capillary type and porous emitters. We already reported on the manufacturing of capillary type emitters [12-15]. Recently we added external and porous emitter designs for test proposes to our design library. The porous emitters fabricated by 3D lithography have a more structured pore composition, free from any kind of randomness with precise and uniform pore sizes. However, using computer code which can simulate authentic porous materials it should be possible to generate 3D CAD models which can be used to print a porous structure which reflects "authentic" porous materials very closely.

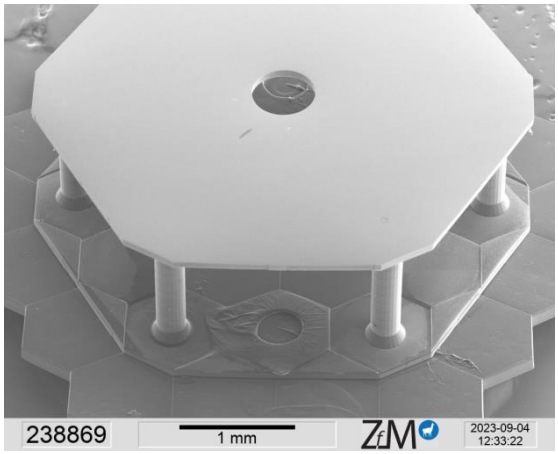

Figure 3. SEM image of a modular integrated extraction electrode alinged to an emitter structure. This design features a single piece, composed of a connector plate with alignment holes, six spacer pillars and the metallised carrier at the top.

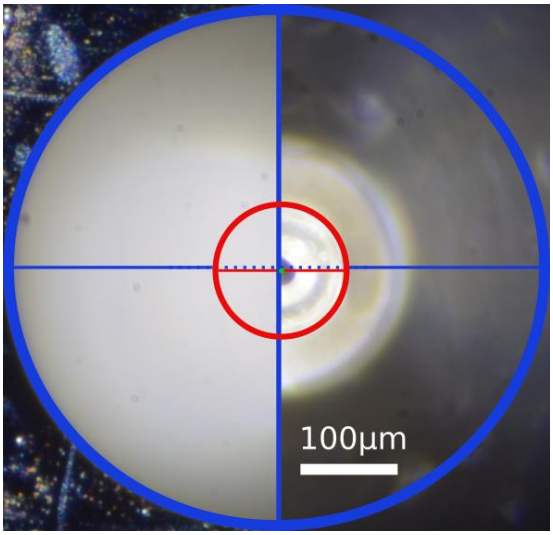

Figure 4. Two microscope images side by side. The images were taken at the same lateral sample position, only at different focus planes. The left image is focused on the electrode carrier and the extractor hole in it. The right image is focused on the emitter structure placed beneath the extractor hole. To better visualise the alignment a blue and red crosshair is overlaid. The blue circle is aligned to the extractor hole and the red circle to the extraction structure. The cross hair indicates the centre of the capillary of the emitter structure. This is an example of the incredible alignment capabilities of the electrode design.

2.3. Modular extraction electrode

The extraction electrode or extraction grid is an essential part of any electrospray thruster. The electrode causes the ion extraction and their acceleration as it allows the electrical field to be contained around the emitters.
The extractor can take shape in a wide variety of types. It can be a metal plate with finely cut or etched holes, a fine wire mesh, or even sintered porous material shaped to a grid.
As we are already fabricating emitter structures via additive manufacturing we also opted to include an electrode in the process. For this purpose, we devolved a modular electrode design, which can be fitted to our emitter structure. It is highly customisable and self-aligning. Fig. 3 shows the result of the design process. The image depicts an integrated extraction electrode aligned to an emitter structure. This design features a completely 3D printed body and a metallised top layer. The body is made up from three distinct sections. The bottom section (visible in the lower third of Fig. 3) is the connection ring. The connection ring's function is to connect the emitter structure to the electrode. There are two alignment holes present in the ring, which fit to the conical alignment pins printed on the emitter array. Such a combination of alignment pin and alignment hole can be seen in the centre of the lower third of Fig. 3. The very tight tolerances of less than 2 µm ensure the alignment of the electrode to the emitter structures, thus making the design self-aligning. In the assembly process the user only has to place the connector ring over the alignment pins and gently push down. If done correctly the electrode will fit itself to the emitter structure and stay in place. By adding a small droplet of two-component-epoxy glue the electrode can be permanently fixated to the emitter structures.
The second part of the electrode body in the spacer layer. The spacer layer consists of multiple pillars which separate the bottom layer from the top layer. There are six cylindrical pillars with a diameter of 50 µm to 300 µm and a height of 300 µm to 2500 µm depending on the user configuration. We opted for round pillars instead of full walls to keep a high visibility of the emitter structures. This allows for in-situ observation of the emission behaviour. If structural integrity is a concern, full walls are a better option. However, the material is very resilient and even these six small pillars already provide significant mechanical stability.
The third and last part of the electrode body is the top layer, the electrode carrier. This is the actual part of the electrode which is electrically active. The carrier is a thin plate of IP-Q material (~70 µm thick) which features the extraction holes. The number position and diameter of the extraction holes can be adjusted to fit the emitter structures. In Fig. 3 the carrier is the flat surface with a single extraction hole in the centre in the middle of the image. Since IP-Q is a polymer and nonconductive, a thin metal layer has to be deposited onto the carrier to give it its electrode capabilities. The deposition is done by a thermal evaporation process. A corresponding device heats a small sample of metal inside a vacuum chamber up to its evaporation temperature. The hot metal defines a point source. The evaporating metal expands outwards, forming a cloud of metal "gas". The metal "gas" condensates on any surface, thus forming a thin film of metal on surface inline of sight. By placing a sample relatively far away (~0.5 m) from the evaporating metal, thin

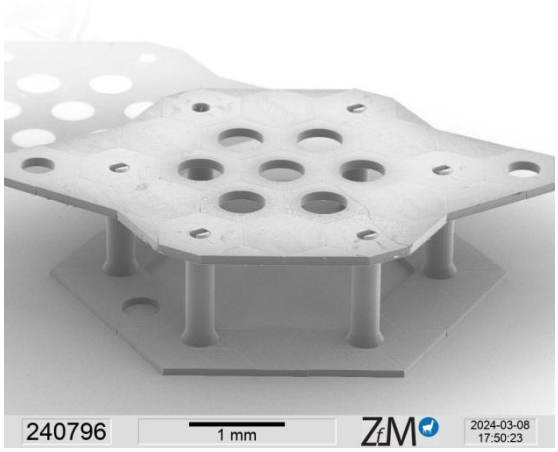

Figure 5. SEM image of the improved modular integrated extraction electrode design. This design features two separate pieces. The bottom part features an improved connection plate and the six spacer pillars. The second part is the carrier plate with the metal layer. In the image the carrier plate is already connected to the bottom part.

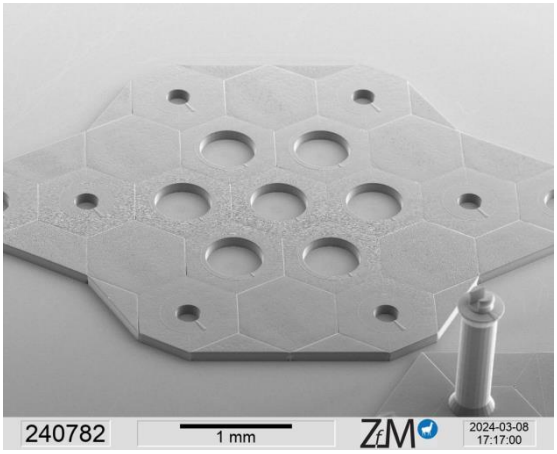

Figure 6. SEM image of the electrode carrier. This part is metallised and functions as extraction grid. The seven holes in the centre are the extractor holes and the smaller holes around are the connection points to the bottom part. At the outer edges there are two holes for wires.

uniform layers of the given metal can be dispositioned precisely. Since the sample is far away compared to the sample dimensions (~3 mm × 3 mm) the trajectories of the incoming metal atoms can be assumed to be parallel. This leads to uniformly thick layers over the sample surface. This method is very directional and only coats the surfaces facing the metal source. Therefore, only the top most layer is coated with metal, which reduces the chance of short circuits occurring between the electrode and the emitter structures.

We typically metallise the carrier with 100 nm of gold. A metal layer of 100 nm is enough to form a continuous conductive layer. Due to the nature of the metallisation process only very little material is needed and multiple electrodes can be prepared simultaneously, making the process highly efficient. We chose gold as carrier material, as it is highly electrically conductive and chemically inert. However, copper, silver and other metals are also viable as substitute for gold. Fig. 4 shows the alignment capabilities of the electrode design. In the image the position of the extractor hole and the emitter structure are compared. The green dot in the middle the cross hair represents the centre of the capillary of the emitter. The dot has only a slight deviation from the centre point of the blue circle, which marks up the extractor hole. The deviation can be estimated to be less than 10 µm. These results were reproduced over multiple samples and are reliable. To connect the electrode to the thruster assembly e.g. to a power supply or a ground connection, a thin wire can be bonded to the metal layer with a ball bonder or by conductive silver paste.

We tested the design with multiple emitters structures. The electrical fields extended from the electrode seem to be strong and provide stable conditions for the extraction of ions. We were able to observe extraction in droplet mode as well as the formation of a Tayler cone in several occasions [12]. Even with all its advantages over a manually placed electrode, its remarkable mechanical stability and easy application, this design still has some drawbacks that need to be addressed.

First and foremost, the unmetallised bottom surface of the carrier layer is an issue. The pure polymer surface does not conduct ions or current, thus acts as a charge trap. Ions extracted from the emitter structure which do not pass through the extractor hole will hit this polymer surface and may stick to it. In the long term a charge up of the layer will occur and distort the applied electrical fields, hindering further extraction or even rendering it impossible.

Another challenge with this design is the connection the external electronic system. Bonding to the surface is possible, but challenging. This method also has a chance to destroy the metal layer by ripping it free from the carrier or the mechanical break the electrode body. A different connection method is necessary to ensure reliable wire connections.

2.4. Improving the electrode design

To overcome the challenges of our design we made multiple improvements. The improved design is shown in Fig. 5.

The first change we made to the design is the separation of the electrode carrier from the rest of the body. This is shown in Fig. 6. This separation allows for the metallisation of the electrode carrier as a separate part. This has multiple advantages. It makes the separate parts easier to print and allows to prefabricate carriers on mass with different metal coatings. However, the major benefit of separating the carrier from the body is the possibility to flip the carrier, that the metal surface now points towards the emitter structures. This completely eliminates

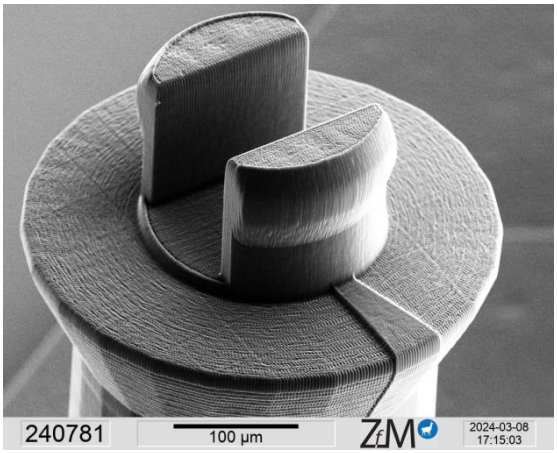

Figure 7. SEM image of the of the top of one pillar. The pillars feature a "click" connection pin. The pin holds the carrier in place once connected and ensures the correct alignment of the electrode carrier to the bottom part.

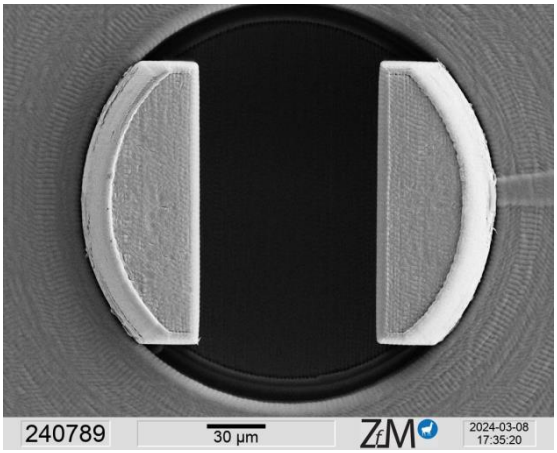

Figure 8. SEM image giving a top view of one connection pin and a connection port of the electrode carrier. The self-alignment properties of the pin system are showcased. The pin tensions the port hole in such a way that is centred around the conical pin.

the charge up challenge and allows any intercepted charge to neutralise to ground. It is also now possible to completely coat the carrier on all surfaces with a metal layer if a need for more conductivity arises. We also added two connection holes for wires to the outside of the carrier. These holes allow wires to be pushed through and to be secured with a small droplet of conductive silver. It is a far safer and easier method of connecting a wire to the electrode compared to the previously used approach. The position of the hole also makes the wire far less intrusive to the whole system.

With the separation of the carrier from the spacer layer, a way to reconnect both was needed. The connection has to be stable, self-aligning and should not impede the functionality of the carrier or the electrode as a whole. For those reasons a manual alignment with gluing it down under a microscope was rejected. The solution was to use the advance 3D printing capabilities of the NanoScribe system. Based on mechanical "click" connection commonly used in automotive industries we designed a "click" pin connection. The "male" pin part of the connection is shown in Fig. 7 and the "female" receiving holes are visible in Fig. 6. These are the six small holes surrounding the extractor holes. The pins feature a cylindrical shaft at the bottom section and expand conically around the half way point. After reaching a maximum circumference they conically reduce their diameter. The holes in the carrier have an about 10 µm larger diameter than the cylindrical portion of the pin, but the hole is about 10 µm smaller than the maximum diameter of the conical pin section. Normally the hole should not be able to fit over the pin, however due to the conical shape at the top of the pin the carrier "slips" over the top part of it and is able to compress the pin inwards. This reduces the diameter of the pin and the hole can fit over the pin. After the hole passes the largest part of the conical portion of the pin, the pin is pushed back outward from the tension of the material. This secures the carrier in place. Furthermore, the conical shape serves as a self-aligning feature. The tension forces on the pin force the electrode carrier down on the pillar. These forces centre the hole to the pin as can be observed in Fig. 8. We estimate from SEM observations like Fig. 8 that the alignment deviation is less than 5 µm. With six pins each centring the carrier, it is aligned to the spacer with very high precision. The connection can be seen in Fig. 5. Although the "click" connection is strong enough to hold the electrode carrier in place against vibrations and movement, it is recommended to permanently lock the electrode carrier in place with small droplets of glue onto the connection pins.

A second change was to redesign the connection plate. The new plate is more sturdy and is placed further away from the emitter structures. These modifications are mostly superficial and do not impact the functionally significantly, but the improved stability is beneficial to the whole design.

3. EMISSION EXPERIMENTS

To verify the performance of the newly developed electrode, we tested it in conjunction with several of our emitter structures. All experiments were carried out in our testing set-up which we described in detail in our previous work [12]. The current design features two optical observing cameras which allow to capture footage of individual emitter structures during operation as well all the other capabilities the set-up had before (time of flight, controlled propellant feeding, flowrate analysis, current measurements).

The feeding system also was moved completely into the vacuum chamber to stop any contamination of the ionic liquid by gases. For the experiments presented here EMIM-Im was used. We previously mostly utilised EMIM-BF_4, but the fluids' habit to form foam and bubbles were a hindrance for the experiments. Therefore, we switched to EMIM-Im, which exhibits a lower surface energy and is in our

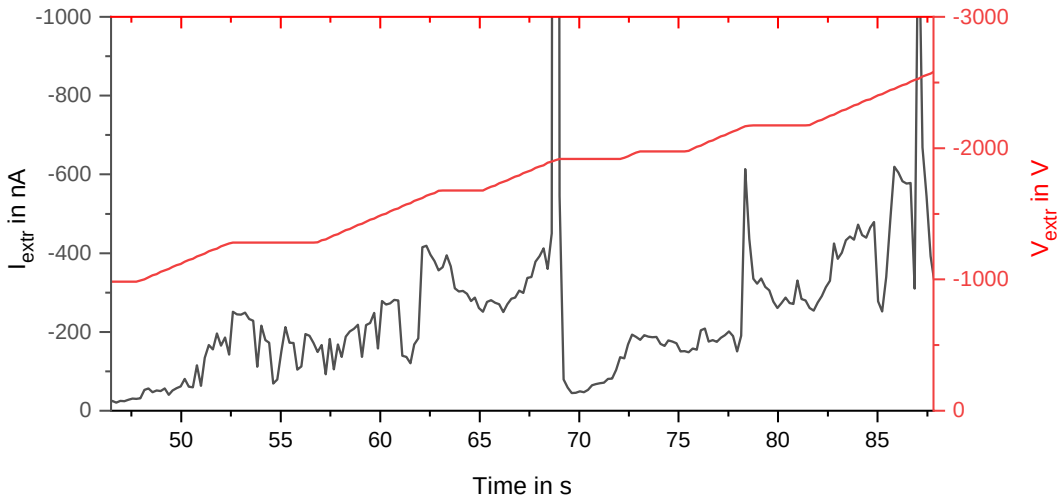

Figure 9. Plotted extraction data from an externally wetted emitter design fitted with a first-generation modular integrated extraction electrode. The data is a selection of 40 seconds of data 45 seconds after the start of the test. On the x-axis the elapsed time is plotted. On the left y-axis (black) the measured extraction current which reached the collector plate is shown. The right y-axis (red) shows the applied extraction voltage between the fluid and the electrode. In the data a clear trend is visible, with rising extraction voltage the extracted current also rises. At around 70 seconds an arcing event occurred, removing a lot of fluid from the emitter structure, thus lowering the current back down until the fluid refilled the expanded volume.

experience less prone to generating bubbles.

With the new extraction electrode, we could reliably extract ions from our emitter structures. The external emitters show the most promise in this regard. Fig. 9 presents a plot of one extraction experiments conducted with an external emitter structure and the new integrated extraction electrode. The emitter structure features seven individual emitters each having its own extractor hole in the electrode.

On the x-axis the elapsed time is plotted, on the left y-axis the measured ion current at the detector is plotted and on the right (red) y-axis the applied extraction voltage to the ionic liquid is plotted. The data presented here comprises a 40 second time frame, which starts 45 seconds after beginning of the experiment. An extraction current starting at 100 nA rising up to 500-600 nA was achieved. Also the extraction current rises alongside the increase in extraction voltage giving it a clear trend. From our optical observation we conclude that not all of the seven emitter structures were involved in the emission and therefore, cannot give an exact value for the current per emitter.

While these are very promising results so far, there are still some challenges that need to be addressed in the future. At the 70 second mark a sharp increase in extraction current can be observed. The maximum reaches about 9000 nA which is far outside the range plotted. This is assumed to be an arcing event. In the video file a bright “flash” can be seen at this moment in time. We assume a large droplet was vaporised by the electrical field and formed a short circuit between the emitters and the electrode. Such events have great destruction potential and are harmful for the metal layer of the electrode. One way to address this challenge could be to change the geometry of the emitter-electrode assembly, thus reducing the possibility of arcing events. Further investigations are being made on which factors influence and cause arcing for our design. Another challenge we are facing is the unstable and erratic extraction. This prevents us from conducting time of flight experiments. Therefore, we cannot estimate the ion energies and the specific impulse for our design yet.

4. CONCLUSION AND OUTLOOK

We presented a newly developed integrated extraction electrode design for electrospray emitters. The electrode is manufactured exclusively by additive manufacturing and is highly modular and adaptive. The design we first introduced as a proof of concept was improved and developed into a stable part of our emitter assemblies. The improved design features a removable electrode carrier, which can be coated with a wide variety of metals and other materials, self-aligning features for the body part as well as the electrode carrier and our newly devolved fast “click” connection system to install the electrode carrier. The alignment deviation of electrode and emitter structure was measured to be less than 5 µm and could be achieved reliably, making its far easier to align and safer to install than conventional electrodes.

We also presented extraction data obtained from electrospray emitters using our new electrode design, verifying its functionally and usability. The experimental results are very promising and imply

that with the use of the integrated electrode emitter assembly the emitter assembly can be miniaturised very effectively.
In the future we will further improve the design using a simulation to calculate the most fitting configuration of electrode carrier and the emitter structure. Such a simulation of the field distribution and fluidic is currently in development. In addition, we want to experiment with surface coatings of the emitters to improve the wettability and electrical conductivity to change the field distribution between electrode and emitter structure. With these improvements we hope to stabilise the emission and conduct time of flight experiments.

ACKNOWLEDGMENTS

The authors gratefully acknowledge funding by the German Federal Ministry for Economic Affairs and Climate Action under the contract (FKZ) 50RS2203.

REFERENCES

1. Lozano, P.C., Martínez-Sánchez, M., Hruby, V.: Electrospray Propulsion, (2010)
2. Lemmer K.: Propulsion for CubeSats: *Acta Astronautica* 134, 231–243 (2017)
3. Holste K, et al.: Ion thrusters for electric propulsion: Scientific issues developing a niche technology into a game changer: *Review of Scientific Instruments* 91(6), 061101 (2020)
4. Lev, D., Myers, R.M., Lemmer, K.M., Kolbeck, J., Koizumi, H., Polzin, K.: The technological and commercial expansion of electric propulsion: *Acta Astronautica* 159, 213–227 (2019)
5. Gomez Jenkins, M., Krejci, D., Lozano, P.: Cubesat constellation management using ionic liquid electrospray propulsion: *Acta Astronautica* 151, 243–252 (2018)
6. Taylor, G.I.: Disintegration of water drops in an electric field: *Proceedings of the Royal Society of London. Series A. Mathematical and Physical Sciences* 280(1382), 383–397 (1964)
7. Krejci, D., Reissner A., Seifert B., Jelem D., Hörbe T., Plesescu F., Friedhof, P., Lai S.: Demonstration of the ifm nano feep thruster in low earth orbit: *4S Symposium*, Sorrento, Italy (2018).
8. Holbrey, J., Seddon, K.: Ionic liquids. *Clean Products and Processes* 1, 223–236 (1999)
9. Rebelo, L.P.N., Canongia Lopes, J.N., Esperan¸ca, J.M.S.S., Filipe, E.: On the critical temperature, normal boiling point, and vapor pressure of ionic liquids: *The Journal of Physical Chemistry B* 109(13), 6040–6043 (2005)
10. Chiu, Y.-H., Dressler, R.: Ionic Liquids for Space Propulsion, *American Chemical Society* vol. 975, pp. 138–160 (2007).
11. Peter, B.S., Dressler, R.A., Chiu, Y.-h., Fedkiw, T.: Electrospray propulsion engineering toolkit (espet): *Aerospace* 7(7) (2020)
12. Kunze, F.L., Henning, T. & Klar, P.J. 3D micro printed capillary electrospray thruster with a fully modular integrated extraction electrode: *Journal of Electric Propul*sion 3, 3 (2024)
13. Kunze, F.L., Henning, T., Klar, P.J.: Taking internally wetted capillary electrospray emitters to the sub-ten-micrometer scale with 3D microlithography: *AIP Advances* 11(10), 105315 (2021)
14. Kunze, F.L., Henning, T., Klar, P.J.: Validation of pure SU-8 micro 3D printed internally wetted capillary type electrospray mircoemitters for thruster applications: *8th international conference on space propulsion*, Estoril (SP2022-082) (2022)
15. Kunze, F.L., Henning, T., Klar, P.J.: 3D micro printed internally wetted capillary type electrospray emitters on the single micrometer scale. *37th International Electric Propulsion Conference (IEPC)*, Boston (IEPC-2022-175) (2022)

3.6 Publication VI: IEPC 2024

This publication represents a significant achievement, arguably more pivotal than previous works in the field. A functional thruster assembly was successfully tested using a modular extraction electrode. A Taylor-Cone was verified through optical observations and the acquisition of video material that documented the emission process. The emission was reproducible, which represents a significant advancement. A series of designs were identified that demonstrate the potential for viability as an electric propulsion system. Further optimisations may be identified that could enhance the emission behaviour. However, a fully 3D-printed electrospray emitter based on polymers has been successfully tested. Based on this publication, the technology has been demonstrated in a laboratory environment, thereby raising its technology readiness level. Additional research may be conducted to improve upon the insights gained, using the results from this publication.

F. Kunze wrote the first draft of the manuscript. The manuscript underwent revision by all of the contributing authors. The experiments and data acquisition were conducted by F. Kunze and P. Carballeira. Furthermore, P. Klar and T. Henning provided supervisory and project management oversight.

Performance characterisation of additive micro fabricated electrospray emitters with an integrated extraction electrode

IEPC-2024-274

Presented at the 38th International Electric Propulsion Conference, Toulouse, France
June 23-28, 2024

Fynn Kunze*
Pedro Carballeira†
Torsten Henning‡
Peter J. Klar§
Justus Liebig University Giessen, Heinrich-Buff-Ring 16, 35392 Giessen, Germany

We present results on micro 3D printed electrospray emitters with an integrated extraction electrode. The fabrication of emitter structures as well as the electrode by two-photon-lithography makes it possible to assemble fully integrated miniaturised thrusters. We conducted emission experiments with such miniaturised emitter assemblies in our electrospray testing facility 'ELEKTRA'. Emission data for three different emitters, an externally wetted emitter, an pseudo-porous emitter and a capillary-type emitter is provided. Each emitter assembly was fully 3D micro printed and features an integrated extraction electrode. In addition, we present image data extracted from live observation of the emitters during operation. Stable emission and the presence of a Taylor-cone is confirmed for the capillary-type emitter.

Nomenclature

JLU	= Justus Liebig University
UV	= ultra violet
IP-Q	= photo resin from NanoScribe
IPx-Q	= photo resin from NanoScribe
EMIM-Im	= 1-Ethyl-3-methylimidazolium bis(trifluoromethylsulfonyl)imide, an ionic liquid
MCP	= multi channel plate
I_{sp}	= specific impulse
V_{extr}	= extraction voltage
I_{ion}	= extraction voltage

* PhD cand., Institute of Experimental Physics I, Fynn.Kunze@physik.uni-giessen.de
† Masters student., Institute of Experimental Physics I, pedro.carballeira.fernandez@physik.uni-giessen.de
‡ Senior staff scientist, Institute of Experimental Physics I, Torsten.Henning@physik.uni-giessen.de
§ Professor and director of Institute of Experimental Physics I, Head of EP-group, Peter.J.Klar@exp1.physik.uni-giessen.de

I. Introduction

With the recent development in the space sector an exponential increase in micro and small satellites launched can be observed. Constellations, earth observation and telecommunication missions in the low earth orbit are some of the most prominent application of such small satellites.[1] With the increased traffic, propulsion capabilities become a necessity for formation flight, collision avoidance and end-of-life de-orbiting. However, most small satellites and cubesats cannot be fitted with a propulsion system due to weight, space, and power constrains. Thus, micro propulsion systems have gathered a lot of attention from various sides.

Electrospray thrusters are an interesting choice for micro propulsion applications.[2] They can be miniaturised to an extreme degree, offer precise thrust and impulse control, require very low power, and can be operated without a neutraliser. These characteristics make them very promising for cubesat missions, constellation flight and precision manoeuvring.

Electrospray thrusters generate thrust by using a static electric field to extract and accelerate ions or droplets from a liquid propellant.[3] The electric field shapes the fluid into a cone known as a Taylor-cone as the field strength increases.[4] At the apex of the Taylor-cone, the electric field density becomes sufficient to draw ions or droplets from the propellant and to accelerate them along the electric field direction. For effective operation, the fluid must be either conductive or have a polar component like water.[4] Common propellants for electrospray thrusters include liquid metals or ionic liquids.[5–7] Liquid metals need to be heated to their melting point before use, with indium being a common choice due to its relatively low melting point of 150 °C. In contrast, ionic liquids remain liquid below room temperature and have minimal vapour pressure, making them stable in vacuum conditions. Ionic liquids are liquid salts and are composed solely of ions, which ensures high electrical conductivity, thus, making them ideal propellants for electrospray thrusters.[5,8] Additionally, ionic liquids allow the extraction of both positive and negative ion species, eliminating the need for an external neutraliser.

An electrospray thruster typically consists of three main components: the propellant intake, the emitter structure, and the extraction electrode. The propellant intake, which can be a tubing system in actively fed thrusters or a reservoir in passively fed systems, supplies the necessary propellant to the emitter structure. Once the fluid reaches the emitter structure, it is subjected to an electric field, enabling ion extraction. There are three types of emitter structures, each differing in how they supply propellant to the emission sites: porous emitters, externally wetted emitters, and capillary emitters.[9] Each type presents its own unique challenges, though the fundamental operating principle remains the same. Figure 1 shows schematic drawings of the different emitter types in operation. The last part of an electrospray thruster assembly is the electrode. It is necessary to shape and apply the electrical field, which extracts and accelerates the ions. Typically a ring-shaped or grid-like electrodes are used. Such electrodes are placed above the emitter structures and are aligned to a cluster of emitters or single emitters.[10]

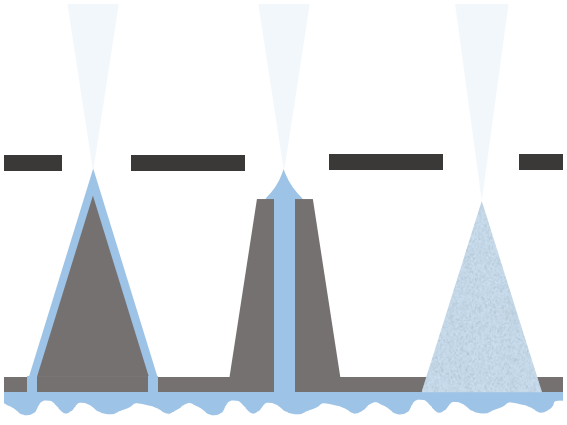

Figure 1. Schematic drawing of the three types of emitter structures. From the left, externally wetted emitters, internally wetted capillary emitters, and porous emitters. The scheme shows the different ways liquid propellant moves to the emitter tip, where it is extracted as a spray of ions or droplets. The structural parts of the emitters are shown in grey, the liquid propellant as light blue, the extraction electrode as dark grey and the ion spray as light grey.

With the miniaturisation of the thruster assembly a set of challenges have to be overcome. The fabrication of miniaturised parts, fluid systems and emitter structures has to be realised. With the shrinking dimensions of the emitter structures, alignment of the electrode to individual emitters has to be more and more precise. The assembly of the thruster head becomes more challenging using the very small parts.

Our approach to take on these challenges stemming from the miniaturisation is the application of high precision additive manufacturing. By using additive manufacturing, it is possible to fabricate micro-fluid systems, emitter structures, micro-connectors for the thruster assembly and more, thus, overcoming multiple challenges posed by the miniaturisation. Our choice of manufacturing method is the two-photon laser-lithography, also called 3D mirco-lithography. Using 3D lithography, we are capable of manufacturing strictures as small as 100 nm in lateral dimensions, making it a good choice for the fabrication of micro-fluid systems. This manufacturing method also inherits most of the advantages associated with classical 3D printing, like the fabrication of hollow, undercut and free floating structures. This opens up the possible design parameters for the emitter structures and the whole thruster assembly.

II. Fabrication and sample preparation

A. Additive manufacturing by two photon lithography

Two-photon lithography or 3D lithography is a micro 3D printing technique closely related to the planar stereo-lithography process in microchip fabrication. Photo lithography in general centred around the photo-chemical interaction of light with a photo resin. By exposing the photo sensitive material to a sufficiently energetic light, typically UV light, a photon is absorbed and the chemical reaction is started.[11,12] The whole process involves multiple steps and transfers a pattern or structure to a substrate. There are two types of photo resits, negative and positive resists. Negative resists harden under the influence of light, while positive resists become more solvable. For additive manufacturing, negative tone resists are used.[11,13]

The primary difference between classical stereo lithography and 3D lithography is the light source. Compared to the UV light used by stereo lithography two-photon lithography utilises a near infra-red laser. The infra-red light passes through the photo-sensitive material without triggering a photo-chemical reaction, as the energy of a single photon is too small. However, by focussing the near infra-red laser through a microscope objective, a small volume of extreme light intensity is generated around the focal point of the optics. In this small volume, also called voxel or volumetric pixel, near the focal point the light intensity is sufficiently high to trigger two-photon absorption processes. Two near infra-red photons carry about the same energy as as single UV photon, thus are able to trigger a photo-chemical reaction.[11,12] By scanning the voxel along a predefined path by either moving the substrate via a stage or by changing the laser path via movable mirrors, any 3D structure can be printed into the material.

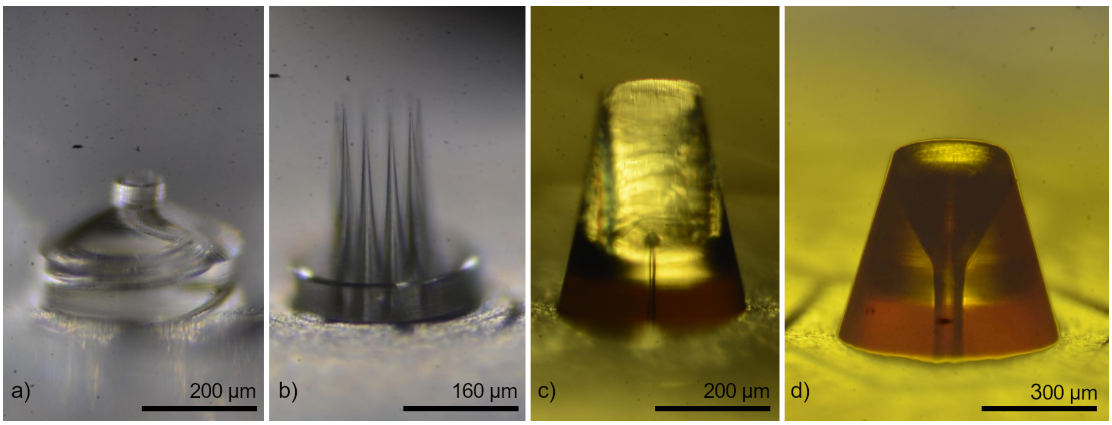

Figure 2. Images of four different emitter structures fabricated by 3D lithography. From left to right a) a capillary-type emitter with a spiral capillary printed in IP-Q, b) a multi-tip externally wetted emitter printed in IP-Q, c) a capillary-type emitter with a very thin 10 µm diameter capillary printed in IPx-Q and d) a internally wetted emitter featuring a large diverging nozzle with a diameter of 300µm at the tip also printed in IPx-Q.

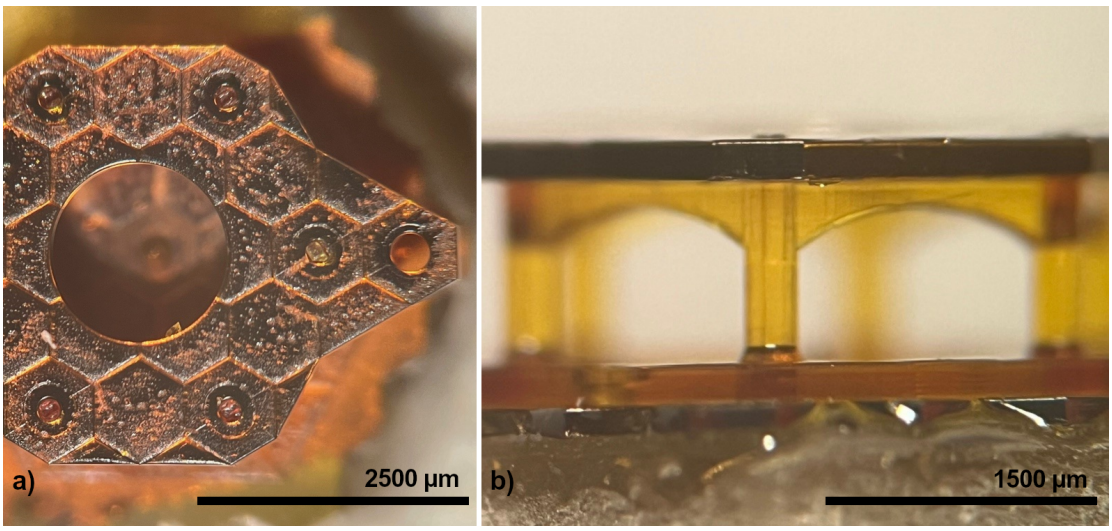

Figure 3. Images taken under an optical microscope showing the electrode assembly in a) top view and b) side view. In the top view a) one large extractor hole is visible with a single emitter below the extractor. The emitter is out of focus. Additionally, five of six connector holes which connect the electrode carrier to the "click-connectors" on the lower part as well as one of the two wire holes can be seen. The side facing of the electrode carrier facing the emitter structure is metallised with gold, giving the electrode a reddish-golden colour. In side view b), the spacer part of the electrode with the pillars and arches can be seen. The carrier, which rest ion the top of the arches and is hold in place by the "click connectors" placed on top of the pillars, is connected to the spacer. The assembly of carrier and spacer is fastened by additional "click connectors" to the top of the emitter plate. The entire assembly is glued to the propellant reservoir propellant reservoir.

Depending on the optics of the 3D lithography system the voxel size varies, which in turn changes the possible printing resolution. In our clean room, we have a NanoScribe PPTG+ system. In high precision mode, the device is capable of reaching a feature resolution better than 100 nm in lateral dimensions. With this device available to us we can manufacture high-precision electrospray emitters and peripheral parts for the thruster assembly. We have shown in our previous work, that we are able to manufacture capillary-type electrospray emitters with a capillary diameter of 10 µm and a capillary length of more than 200 µm.[14] Furthermore, since we benefit from the freedom of design, we can manufacture emitter geometries that are impossible to fabricate with subtractive or less precise methods. As an example, we manufactured emitter geometries with a spiral capillary and emitters with a free floating ball inside to regulate the propellant flow. Furthermore, pseudo-porously structured material and externally wetted emitters can be manufactured. Figure 2 shows some examples of fabricated emitters, featuring a spiral capillary, a thin long capillary and the the aforementioned 'ball-valve' emitter.

B. Integrated electrode and emitter assembly

Besides emitter structures, we can also manufacture peripheral parts like the extraction electrode for the thruster assembly. By 3D printing the extraction electrode, we can utilise the precision of the printing process to guarantee the alignment of emitter structure and extractor hole. This also allows us to manufacture customised electrodes specially adapted for our emitters. Our current electrode design went through multiple iterations and improvements and is made up from two parts. Figure 3 shows our current design of the electrode assembly.

The first part is the electrode carrier, which is the electrically active part of the electrode assembly. It is a 200 µm thick plate with the extractor holes. The number, size, and position of the holes can be adjusted freely and offers great flexibility. While the plate is made from a polymer and is, thus, non-conductive, a thin metal layer is depositioned using a thermal evaporation device. A wide variety of metals are available for coating and we opt for either gold or silver, due to their high conductivity and easy handling during deposition. Additionally, the carrier plate features six very small connector holes and two larger contact

holes. The contact holes can fit a thin wire which than connects the metal plating to an electrical contact. With the six connector holes the carrier is later friction fitted to the second part of the electrode, the spacer. The spacer, as the name implies, is used to generate the desired spacing between the emitter structures and the electrode carrier. It can be split in three levels. On the first level a thin ring plate with two alignment holes is present. This ring later sits on the emitter surface and physically connects the electrode assembly to the emitter structures via the alignment holes. The second level is made up from six round pillars. These pillars determine the distance of the electrode carrier from the emitter structure. The height of the pillars can be changed depending on the use case and is freely adjustable. On the last level of the spacer, arches connect the pillars and stabilise the structure. Placed onto the arches are six "click-connectors". These "click-connectors" fit into the six small holes on the electrode carrier and allow it to be fitted onto the spacer. Using this kind of connecting method, the electrode can be assembled completely without glue or other adhesives. It can hold together even under mechanical stress just due to the tight tolerances and the design of the connectors. While the connectors can withstand a quite surprising amount of force before disconnecting, they can still be carefully dislodged and the electrode can be disassembled without damaging any parts. With this design we have a very flexible part available for our emitter structures and we can adopt our thruster design on the requirements.

III. Experimental methods

A. Experimental set-up

We use our electrospray characterisation set-up 'ELEKTRA' at the JLU Giessen for the characterisation of the manufactured samples. Figure 4 shows a simplified schematic drawing of the set-up. The set-up features two identical cubic vacuum chambers connected via a plate valve. Each chamber is fitted with a turbo molecular pump and a roughing pump, which let the chambers reach a background pressure as low as 5×10^{-8} mbar.

In the first chamber the fluid assembly, the propellant feeding system, DC current collectors and connectors for the voltage supplies are present. The fluid assembly and propellant feeding system consist of a high precision syringe pump and a fused silica capillary tubing system. Threaded fittings connect the emitter assembly to the tubing system. Depending on the syringe used, the feeding rate can be set in the nano litre per minute range, thus allowing very fine control over the propellant flow. In the first chamber a collector plate is placed in the beam path of the emitters, which collects all extracted ions. The emission current can be measured using amplifier electronics in conjunction with the collector plate. A window on one side of the chamber grants optical access to the interior of the chamber. In-situ footage of individual emitters is captured by a camera with microscope optics placed in front of the window.

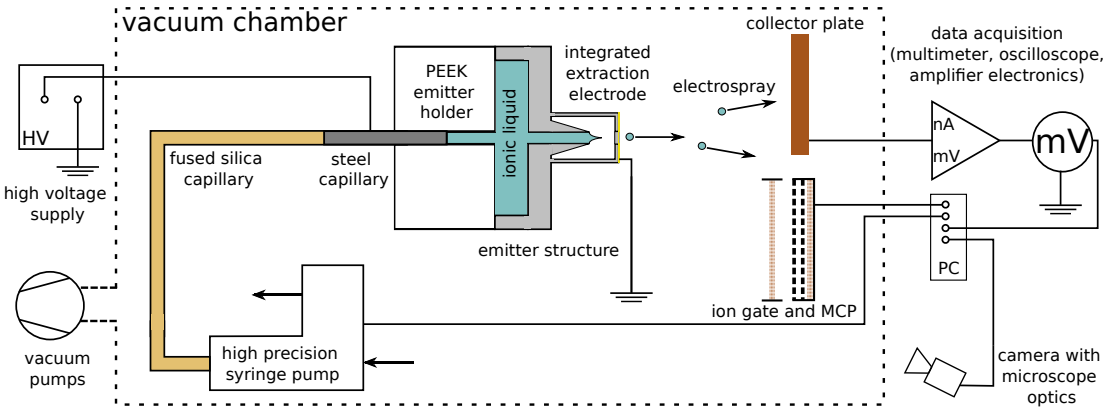

Figure 4. Simplified schematic drawing of the 'ELEKTRA' testing facility at the JLU Giessen. The facility is used to test and characterise electrospray emitters. The set-up features a controllable high precision propellant feeding system, DC measurement with the necessary electronics, an optical camera or in-situ video capture and a time-of-flight MCP mass spectrometer.

The second chamber houses a multi channel plate (MCP) delay-line mass spectrometer. This advanced detector system is capable of detecting individual ions and their lateral impact position on the MCP. Using this set-up in combination with an pulsed ion gate, time of flight and beam postilion data can be obtained, which makes it possible to calculate the I_{sp} and the beam divergence angle of a given thruster. More information about the experimental set-up can be found in our previous work.[14–16]

B. In-situ optical characterisation

To gain more insight into the emission behaviour besides the DC measurements, optical observations offer a significant advantage in identifying characteristics of the emitter structures used. By observing the emitter structures directly, we gain information about the emission process and to some degree can identify the emission mode. Additionally, we can correlate the images from the optical observation with the results of the simultaneously conducted DC measurements and thus gain even more information about the emission. By using a live video feed it is also possible to adjust the emission parameters like extraction voltage and feeding rate according to the situation observed. Furthermore, the video helps to find the cause of arcing, which is one of the major causes of failure for electrospray thrusters. The video data allows reviewing previous tests and analysing challenges and potential problems for each design tested. Based on the findings we can identify the influence of the emitter geometry on the emission behaviour and further refine or rethink our approach on emitter geometries.

For our optical observation, we use a 'Pixelink' grey scale camera. An adjustable focus tube connects the camera with a 10× microscope objective with an long focal length. Via the adjustable focus the magnification of the image can be adjusted, which makes it possible to zoom in on either an individual emitter or capture an overview of multiple emitters.

IV. Experimental results

We selected various characteristics we want to examine ion the context of performance tests. The selected parameters may differ from conventionally selected ones, but are essential for this step in the development of our electrospray thruster. We examine the stability of emission, propellant flow behaviour, emission current, and necessary extraction voltage. Since we work with a wide range of geometries for our emitter structures, including externally wetted, porous emitters and capillary type emitters, we focus on identifying the influence of the emitter geometry on the emission. Furthermore, we developed our integrated extraction electrode and want to characterise how different electrode geometries change the emission dynamics of the emitters. We want to categorize and identify geometries that work best, before optimising the thruster for usage. To gain such insight we use the 'ELEKTRA' facility and focus on optical and emission current data for the moment. In this regard no time-of-flight experiments were carried out yet, but we will further characterise promising emitter geometries using time-of-flight experiments in the future.

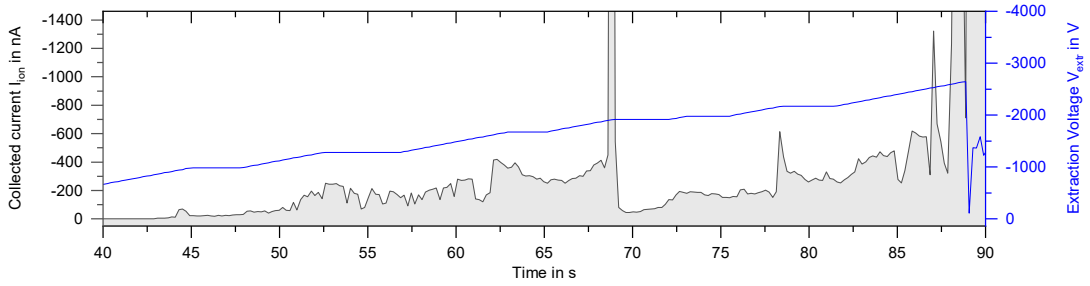

Figure 5. Extraction data collected from a cluster of seven externally wetted emitters. The emitter design features a fluid retention ring around each emitter, a propellant supply capillary for each emitter and emitter shaped similar to the one shown in Fig. 2 b) . For this experiment the active feeding system of the 'ELEKTRA' facility with EMIM-Im as propellant was used. The graph shows the measured current collected at the collector plate and applied extraction voltage against the time.

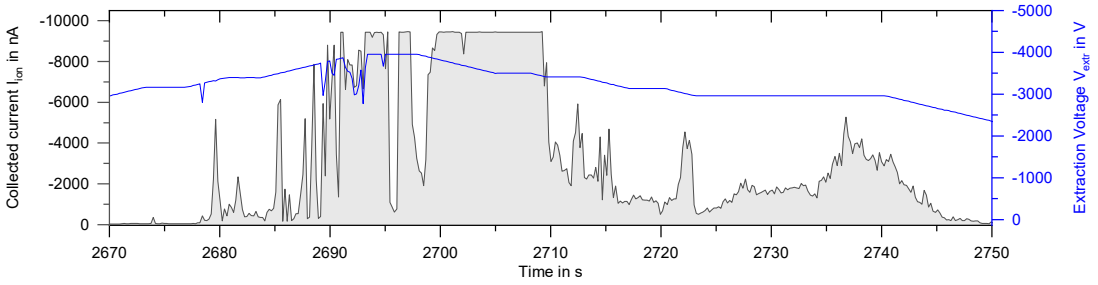

Figure 6. Extraction data collected from a single pseudo-porous emitter structure. The pseudo-porous emitter is made up from about 30 interconnected square capillaries with a side length of 10 µm. The capillaries form a mesh like structure mimicking a porous material without any randomness. For this experiment the active feeding system of the 'ELEKTRA' facility with EMIM-Im as propellant was used. The graph shows the measured current collected at the collector plate and applied extraction voltage against the time.

A. Externally wetted emitter

The first results we want to present are from an externally wetted emitter. The emitter design used in this experiment features a shape similar to the emitter shown in Fig. 2, but with only one cone structure instead of a crown configuration. The design has a fluid retention, so the propellant is contained in the area close to the emitter. Propellant is supplied via four small feeding capillaries, connecting the base of the emitter to a reservoir beneath it. A cluster of seven identical emitters is placed in an equidistant formation on the surface. For this experiment, we used our integrated extraction electrode with seven extractor holes, each aligned to one emitter. As propellant we used EMIM-Im, which was supplied to the emitters by the active feeding system of the 'ELEKTRA' facility. We measured the extracted current at the collector plate and the applied extraction voltage over time. The results are shown in Fig. 5. During the experiment the emitters were first primed with propellant. A fixed amount of liquid was pumped into the reservoir and the emitters. In the video feed it was confirmed that the liquid was confined by the retention ring. Afterwards a voltage was applied to the ionic liquid. As seen in Fig. 5, at a voltage of about 200 V the first ions were extracted around the 45 second mark. The current increased with the applied voltage. At the 68 second mark an arcing event occurred, resulting in a very high peak of extracted current. The extraction stabilised afterwards and resumed the trend from before till the 88 second mark. At this point multiple arcing events occurred and stopped the controlled emission.

B. Pseudo-porous emitter

The second result we want to share is obtained from from a pseudo-porous emitter. What we call a pseudo-porous emitter is a structured material that features multiple interconnected capillaries forming a porous-like super structure. In our design we used square capillaries with a 10 µm side length, which resulted in a 'waffle' like emitter appearance. Each capillaries had a length of 200 µm and the emitter featured more than 30 of these interconnected capillaries. Again we used an integrated electrode with a single extractor hole aligned to the emitter. Similar to the experiment presented above we used the EMIM-Im and the active feeding system of our testing set-up. For this experiment the voltage was applied before the fluid was pumped into the emitter. We opted for a fluid based start-up since we wanted to discourage overspilling. The obtained results can be seen in Fig. 6. In the figure the graph shows the collected current an applied high voltage over time. The first ions were registered around the 2680 second mark. A long wind-up time resulted from the fluid based start-up, because the fluid first needed to penetrate the porous like structure. This could be observed in the camera feed. In the graph the current is cut-off at the -10000 nA level in multiple segments. The extracted current was so high in these segments, that it overflowed the measurement range of the amplifier electronics resulting in the cut-off data. The real extraction current was higher than what was measured, but we cannot make any assumption about its real value at these points.

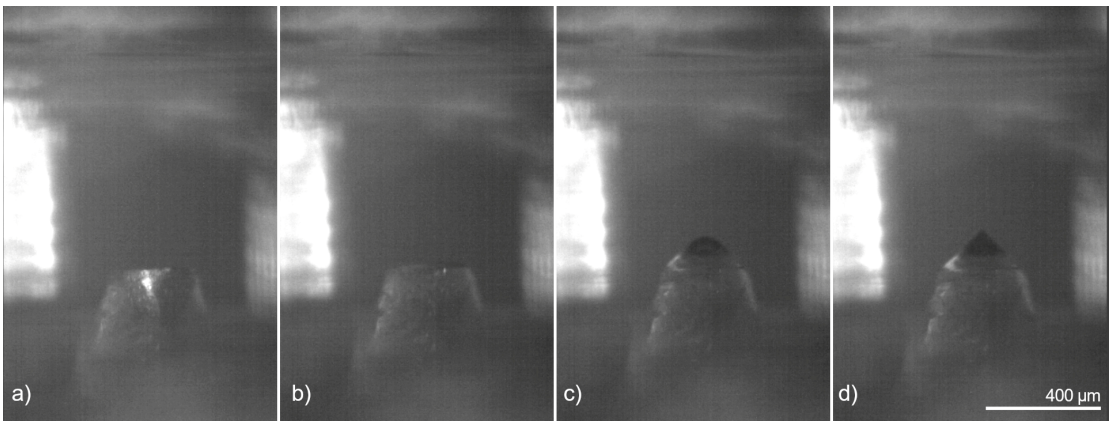

Figure 7. A series of four images extracted from a live video capture of a single capillary type emitter. In all four images the same emitter is shown at different times of the experiment. Starting from the left the emitter at the beginning of the experiment is visible. The capillary is empty and no voltage was applied. In the second image a low voltage was applied to the ionic liquid. The liquid is pulled into the emitter and fills it up to the top. In the third image a voltage of about 1500 V was applied. At the tip of the emitter a fluid meniscus can be observed, In the last image the a Taylor-cone is clearly visible at the emitter tip. A voltage of 2200 V was applied to the liquid for the Taylor-cone to from.

C. Capillary-type emitter

The third and last results we want to share is a data set consisting of four images extracted from the camera feed and the correlating measured data. The data is from a capillary-type emitter with a diverging nozzle. Figure 2 d) shows the emitter. The nozzle diameter increases from 60 µm capillary at the feeding capillary to a 300 µm diameter at the tip. For this experiment we used a passive feeding system. EMIM-Im was pre filled into a reservoir below the emitter structure, which was open on one side exposing the ionic liquid to thev acuum conditions of the test chamber.

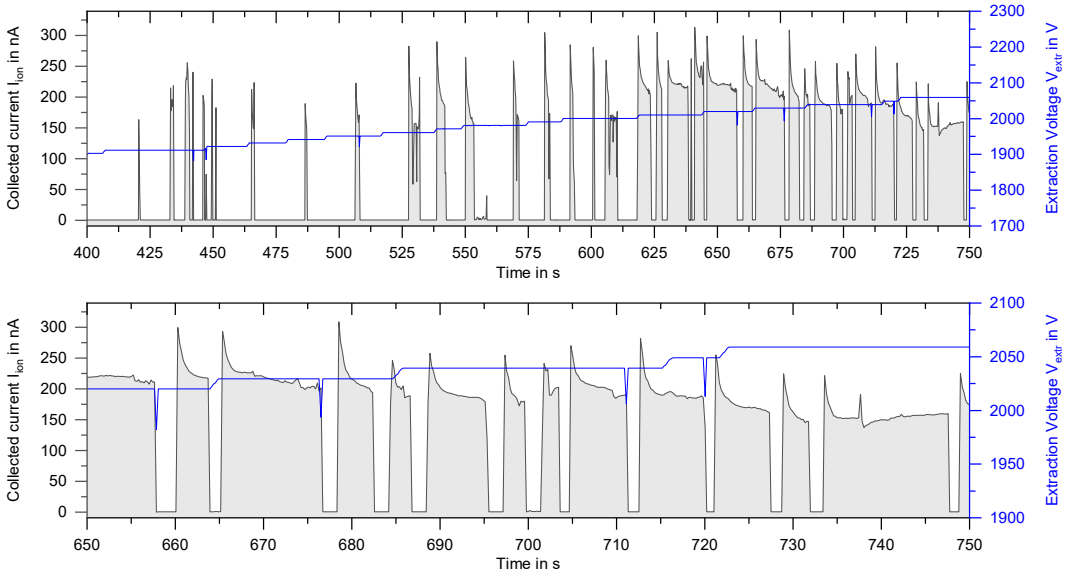

Figure 8. Extraction data collected from a capillary type emitter with a diverging nozzle. The nozzle diameter increases from 60 µm to 300 µm. For this experiment, a passive propellant feeding system without flow control was used. The propellant was the ionic liquid EMIM-Im. The graph at the top shows the measured current collected at the collector plate and applied extraction voltage against the time. The graph at the bottom shows a selection of the same data at a smaller time scale.On the shorter time scale, the extraction trend becomes visible.

A thin stainless steel wire was dipped into the fluid resting in the reservoir and connects it to the negative HV power supply. This emitter was also fitted with an integrated extraction electrode. Via the camera live view we were able to capture relevant optical data. We could identify significant steps during the emitter start-up. At the start the emitter was completely empty, since no fluid was pushed into it during assembly and fuelling. This is shown by Fig. 7 a). For the first start-up we raised the extraction voltage from 0 V linearly to 2000 V with a rate of 10 $\frac{\mathrm{V}}{\mathrm{s}}$. At about 500 V we could observe the fluid being pulled from the reservoir below into the capillary. The fluid rose up to the tip where it stopped by itself, visible in Fig. 7 b). With further rising voltage, the fluid was pulled into a meniscus over the emitter tip as shown in Fig. 7 c). After reaching 1900 V, the meniscus periodically transformed into a Taylor-cone and started emitting ions. Such a Taylor-cone is presented in Fig. 7 d). In the video the Taylor-cone was stable for a few seconds and than collapsed back to the meniscus. It than reformed after a short time, repeating the cycle again. With higher voltage, the emission became more stable and the intervals between cone formation decreased. This can also be seen in the collected current data in Fig. 8. The top graph shows an overview of the start-up process beginning with the first observed Taylor-cone The second graph at the bottom of the figure shows a magnified section of the later time span of the experiment. From the data the formation of the Taylor-cones and their decay can be observed. Also the trend of more stable emission with rising voltage is visible, as the intervals between single emission events reduces and the cone stays stable for longer periods. This data was obtained using a positive voltage supply. We repeated the experiments with negative extraction voltage and a pulsed positive-negative voltage. For all cases we were able to reproduce the results. However, with the pulsed voltage the results were far less stable and varied significantly with the applied voltage ratio. Nevertheless, we were able to extract ions in both polarities.

V. Discussion of results

Based on our self-set standards regarding the performance of our emitters we can evaluate them. Starting with the external emitters we can assess the stability of emission, propellant flow behaviour, emission current, and necessary extraction voltage. From the data it is clear that the maximal emission current level is too low for a seven emitter cluster. We suspect that not all of the emitters were evenly supplied with propellant and therefore emitted ions at different rates. We reached about 250 nA at an extraction voltage for about 500 V. The ratio of extracted current to applied voltage is quite promising. If the trend visible in the data can be continued by improving the fluid distribution and emitter geometry, these 3D micro printed externally wetted emitters may perform similar to conventionally fabricated externally wetted emitters. However, in the data multiple arcing events can be seen. At the end, near 2000 V of extraction voltage, the emission resulted in such heavy arcing, that the emitter structures were destroyed. To make use of the promising trend in extraction current we need to address the arcing challenge. On way to achieve this is to change the geometry or propellant distribution of the emitters as well as the electrode shape. Further experiments need to be conducted to come to a conclusion, but so far the results are encouraging.

Out of the three emitter types we explored emitters the pseudo-porous material the least. The idea of fabricating a structured material mimicking porous emitters is quite new, due to the challenging fabrication process. From what we observed in our experiments the material behaves differently compared to "natural" porous materials. This makes sense, as the fabricated material lacks any kind of randomness. Amongst the emitters tested, the pseudo porous emitter has the highest emission current per emitter. A single emitter was able to emit more than 10.000 nA of current. The real peak current is unknown as the emitted current went over the measurement range. The emitter design here has a footprint of $3.8 \cdot 10^{-8}\,\mathrm{m}^2$ resulting in a theoretical current emission per area of more than 250 $\frac{\mathrm{A}}{\mathrm{m}^2}$. However, the data reveals also that the emission was extremely unstable, lasting only about 20 s. The emitter also needed significant higher operation voltages compared to the other emitters tested. Higher voltages showed in our experiments a trend to more and heavier arcing. A lot more results are needed to come to a conclusion regarding this emitter geometry.

The most stable and predicable emission was shown by the capillary emitter. We could repetitively start and stop the extraction in both polarities. The emission current profile was very consistent averaging to about 200 nA for a single emitter. This emission current translates to a current emission per area of about 2.8 $\frac{\mathrm{A}}{\mathrm{m}^2}$. While the emitted current is significantly lower than that of the porous emitter we tested, the emission was very stable. We did not observe any arcing during operation. Furthermore, no active feeding was required making it the simplest of the three designs. During the experiment the liquid did not overspill at all and was well contained by the emitter tip. The geometry is very promising and is a good candidate

for further development.

VI. Conclusion and outlook

The results we have presented in this paper show that there is a lot of potential in additively manufactured electrospray emitters. The freedom of design offered by the 3D lithography emitter geometries enables us to prepare designs previously impossible to manufacture. This technique is applicable to all three emitter types making it very versatile. Additionally peripheral parts like the extraction electrode can also be manufactured as well. In combination very fine tuned and precise thruster assemblies can be made. We have presented images of such emitter parts and an integrated extraction electrode. The assembled thruster heads were tested in out electrospray test facility 'ELEKTRA' at the JLU Giessen. Data for one emitter of every category, externally wetted emitter, capillary-type emitter and pseudo-porous emitter, was presented proving the feasibility of our manufacturing method. The data shows promising trends especially for externally wetted and capillary type emitters. A stable emission in both polarities as well as in pulsed mode was achieved with a capillary type emitter. Emission for both pseudo-porous and externally wetted emitters was possible as well, however, less stable.

In our future work, we want to focus more on improving the designs presented here. With improving the structured materials new possibilities may arise further helping to advance the emitters and their emission behaviour. Additional we want to characterise the existing emitters in more detail using our time-of-flight set-up to determine the specific impulse and emission mode. We also need to measure the intercepted current at our electrode and adjust the extractor design to minimise any ion impacts on the electrode.

Acknowledgments

The authors gratefully acknowledge funding by the German Federal Ministry for Economic Affairs and Climate Action under the contract (FKZ) 50RS2203.

References

[1]E. S. D. Office, "ESA'S ANNUAL SPACE ENVIRONMENT REPORT." `https://www.sdo.esoc.esa.int/environment_report/Space_Environment_Report_latest.pdf`, 2024. Accessed: 2024-05-10.

[2]K. Lemmer, "Propulsion for CubeSats," *Acta Astronautica*, vol. 134, pp. 231–243, 2017.

[3]P. C. Lozano, M. Martínez-Sánchez, and V. Hruby, *Electrospray Propulsion*. 2010.

[4]G. I. Taylor, "Disintegration of water drops in an electric field," *Proceedings of the Royal Society of London. Series A. Mathematical and Physical Sciences*, vol. 280, no. 1382, pp. 383–397, 1964.

[5]D. V. M. Máximo and L. F. Velásquez-García, "Additively manufactured electrohydrodynamic ionic liquid pure-ion sources for nanosatellite propulsion," *Additive Manufacturing*, vol. 36, p. 101719, 2020.

[6]B. D. Prince, B. A. Fritz, and Y.-H. Chiu, *Ionic Liquids in Electrospray Propulsion Systems*, ch. 2, pp. 27–49.

[7]D. Krejci and P. Lozano, "Space propulsion technology for small spacecraft," *Proceedings of the IEEE*, vol. 106, pp. 362–378, 3 2018.

[8]J. Holbrey and K. Seddon, "Ionic liquids," *Clean Products and Processes*, vol. 1, pp. 223–236, 1999.

[9]B. S. Peter, R. A. Dressler, Y.-h. Chiu, and T. Fedkiw, "Electrospray propulsion engineering toolkit (espet)," *Aerospace*, vol. 7, no. 7, 2020.

[10]S. Dandavino, C. Ataman, C. N. Ryan, S. Chakraborty, D. Courtney, J. P. W. Stark, and H. Shea, "Microfabricated electrospray emitter arrays with integrated extractor and accelerator electrodes for the propulsion of small spacecraft," *Journal of Micromechanics and Microengineering*, vol. 24, p. 075011, 6 2014.

[11]V. Harinarayana and Y. Shin, "Two-photon lithography for three-dimensional fabrication in micro/nanoscale regime: A comprehensive review," *Optics and Laser Technology*, vol. 142, p. 107180, 2021.

[12]F. L. Kunze, T. Henning, and P. J. Klar, "Taking internally wetted capillary electrospray emitters to the sub-ten-micrometer scale with 3d microlithography," *AIP Advances*, vol. 11, no. 10, p. 105315, 2021.

[13]A. del Campo and C. Greiner, "SU-8: a photoresist for high-aspect-ratio and 3d submicron lithography," *Journal of Micromechanics and Microengineering*, vol. 17, pp. R81–R95, may 2007.

[14]F. L. Kunze, T. Henning, and P. J. Klar, "3d micro printed capillary electrospray thruster with a fully modular integrated extraction electrode," *Journal of Electric Propulsion*, vol. 3, no. 3, 2024.

[15]F. L. Kunze, T. Henning, and P. J. Klar, "Validation of pure su-8 micro 3d printed internally wetted capillary type electrospray mircoemitters for thruster applications," in *8th internatinonal conference on space propulsion, Estoril*, no. SP2022-082, 2022.

[16]F. L. Kunze, T. Henning, and P. J. Klar, "3D micro printed internally wetted capillary type electrospray emitters on the single micrometer scale," *37th International Electric Propulsion Conference (IEPC), Boston*, no. IEPC-2022-175, 2022.

Chapter 4

Discussion

The results achieved over the course of the project are, on the whole, highly satisfactory. The initial objectives of the project were achieved, and a laboratory prototype of a micro 3D-printed electrospray emitter was subjected to a successful series of tests (VI). However, this constitutes merely the inaugural phase of this technology. There are, however, several challenges that remain to be addressed, including the adaptation of an active feeding system for the 3D-printed capillary emitters. Moreover, further experiments are required to investigate the impact of geometry on emission behaviour.

During the course of the project, a number of unforeseen challenges had to be addressed, necessitating the implementation of alternative solutions. It was initially assumed that the fabrication process would present the most significant challenge. However, the fabrication process was found to be more straightforward to resolve in comparison to the characterisation experiments (V,VI). The characterisation experiments presented a significantly greater challenge due to unreliable data acquisition and reproducibility issues. The high degree of miniaturisation introduced an additional layer of complexity to the challenge (IV). Furthermore, it was difficult to distinguish between successful and unsuccessful tests. It was exceedingly difficult to reproduce the circumstances that led to a positive outcome (I,II).

At the outset of the project, the primary objective was to adapt the findings of the preceding project [8–10, 15]. This entailed the translation of the 2.5D capillary emitter design to a comprehensive 3D-based fabrication process. The adaptation process was successfully implemented; however, a direct continuation of the previous design was not feasible due to the limitations of the new fabrication method (I,II). This significantly reduced the potential insights that could be gained from the previous results. The fabrication process utilising SU-8 polymer demonstrated a relatively rapid and notable advancement in comparison to the previously employed 2.5D process, particularly in terms of design parameters (I - III).

Emitters with a capillary diameter of less than 10 µm and a height of 200 µm represent a notable advancement in microtechnology documented in the existing literature [32, 61] (I - III).

Although these results are noteworthy, it should be noted that SU-8 has not been demonstrated to support structures exceeding 250 µm in height. This impeded the advancement of the thruster system as a whole. Moreover, the extreme miniaturisation also presented a challenge. The SU-8 emitter exhibited a tendency to overflow during operation (IV). In light of the findings from the preceding project, it was initially hypothesised that an active feeding system would be necessary. This hypothesis was also partially confirmed. The capillary tubes were found to require a relatively high pressure to prime them with fluid, due to their small diameter of 10 µm. However, once the capillary was filled, a steady flow was observed, even with no or minimal input pressure. This results in overspilling (IV). A hypothesis that is currently being tested is that, contrary to the Law of Hagen-Poiseuille, which predicts a reduction in flow rate with decreasing diameter, at this micro scale capillary forces dominate the flow regime. The capillary forces continue to pull fluid through even though the feeding mechanism is stopped. While this hypothesis has yet to be confirmed and needs further verification, the observed results align with those observed by other groups who have explored emitters as small as these [32, 61].

In consideration of these findings, a decision was made to pursue a multifaceted approach to addressing this challenge. Firstly, the process of extreme miniaturisation was halted in favour of adopting larger emitters with a capillary diameter of 60 µm (IV-VI). Secondly, in order to address the issue of overspilling, a passive feeding system was implemented (VI). Larger emitters could be manufactured using IP-Q resin, and a new large feature processing solution was introduced for use with the 3D lithography device (IV-VI). The capacity to manufacture structured elements up to 10 mm in height has enabled the creation of new designs. The new emitter designs retained the high aspect ratio capillary with an emitter height of up to 600 µm, while utilising larger capillary diameters (VI). Therefore, this was not a regression in fabrication capabilities. Furthermore, the possibility of integrating a modular extractor electrode, which can be attached directly to the emitter structure, is also afforded. The fabrication of a fully 3D-printed extractor electrode at this level of miniaturisation represents a novel approach within this technology. No other devices comparable to this one could be found in the literature, which marks this as noteworthy achievement (IV,V).

With the adaptation of lager emitters and a passive feeding system, more reliable and reproducible experiments could be conducted. Another major factor that improved the advancement and troubleshooting was the implementation of a camera

system that allowed to obverse the emitters during testing (IV,VI). The optical feedback was essential in identifying the issue regarding the active feeding system. The captured videos also allow to optical identify the emission modes of the emitter to some degree, adding more insights to the experimental results.

Nevertheless, despite the favourable outcome of the project, there are still numerous aspects that require further investigation. The most pressing requirement is to ascertain the influence of the emitter geometry on the emission behaviour. An optimised geometry for emission is a prerequisite for future advancements into array configurations. It has been demonstrated that single emitters are capable of emitting up to 10 µA of current, which is a notable achievement (VI). However, this is not sufficient for a full thruster system. This necessitates the implementation of an array-based approach in the future. Moreover, additional data on dual polarity emission is necessary. While the emission in both polarities has been confirmed, stable emission with switching polarities has not yet been achieved. This is also essential for the implementation of this technology as a thruster system. Furthermore, the feeding system must be redesigned to support long-term testing. The passive feeding system can only support a certain operation time; therefore, either an advanced passive system must be implemented or the active feeding system must be reimplemented.

Chapter 5

Current status, trends and future prospects

5.1 Status of the development

Significant advancements with promising novel results have been made since the last publication included in chapter 3 of this thesis. The technology has demonstrated considerable advancement over a relatively brief period of time, with results that in quality surpass those presented so far in literature and define the current state-of-the-art.

An additional series of experiments was conducted to investigate the influence of the emitter geometry on the emission behaviour. The emitter design used for these experimental series is based on the design presented in a conference publication for the IEPC 2024, which can be found in chapter 3. The emitter assembly includes the integrated extraction electrode developed during this project, with the specific design parameters used for this series shown in Fig. A.2 in the appendix. The extraction electrode features an orifice diameter of 1715 µm at a distance of 700 µm from the emitter top corresponding to an opening half angle of roughly 50° in the standard configuration. In excess of 50 individual emitters and a number of emitter geometries have been characterised, yielding valuable insights and significant results. Four distinct approaches to gain insight into the emission behaviour were employed: (i) a systematic variation of the emitter orifice diameter, (ii) a systematic variation of the inner capillary diameter, (iii) a variation of the spacing between the emitter and the extraction electrode, and (iv) a study of a newly developed emitter design, which was based lessens learned during the experimental series (i) to (iii).

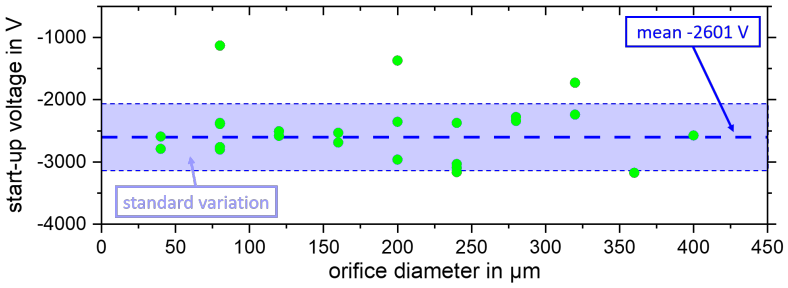

Figure 5.1: Data obtained on series (i) of emitters. Plotted is the start-up voltage against the orifice diameter for 21 emitters. The dashed blue line marks the mean start-up voltage and the blue shaded area the standard deviation. A schematic drawing of the emitter design used is shown in Fig. A.1 in the appendix. A systemic incrementation from 400 µm to 40 µm in 40 µm steps was applied to the orifice diameter, and therefore also the orifice angle. All the other parameters were unchanged. The emitters were characterised with a negative polarity extraction voltage with a passive feeding system in the experimental set-up described in chapter 3.

Approach (i) focused on a systematic variation applied to the emitter orifice diameter, reducing it from 400 µm to 40 µm in 40 µm increments. To keep the design parameters as controlled as possible, only parameters in direct correlation with the orifice diameter, like the orifice angle, were changed to acquire a consistent emitter geometry. The technical drawing of the emitter geometry used is provided in the Fig. A.1 in the appendix. In consideration of potential fabrication defects, three sets of seven to ten emitters, with a total of 28 emitters, were characterised of which 21 yielded usable results. The emitters exhibiting unusable results had fabrication defects or did not show any emission.

The results obtained from this experimental campaign are shown in Fig. 5.1, Fig. 5.2, and Fig. 5.3. The first important result is the reproducible and predicable ion emission from the emitters. All tested emitters in this series were capable of producing an extraction current. Furthermore, it was observed that the emission behaviour exhibited a number of intriguing patterns, which offer significant potential for further investigation and development. Firstly, the start-up voltage, defined as the voltage at which a Taylor cone first forms and begins to emit ions, appears to be relatively constant across all emitter orifice diameters for this emitter geometry. With the exception of a few emitters, the start-up voltage was observed to be approximately -2000 V to -3000 V in negative polarity. This can be seen in Fig. 5.1. Most of the emitters are within the single standard deviation from the mean start-up voltage of approximately -2600 V. The mean start-up voltage is indicated by the blue line in Fig. 5.1 and the standard deviation by the blue shaded area. The observed exceptions, which are statistically outside the voltage range, may be explained by either surface wetting or a difference in background

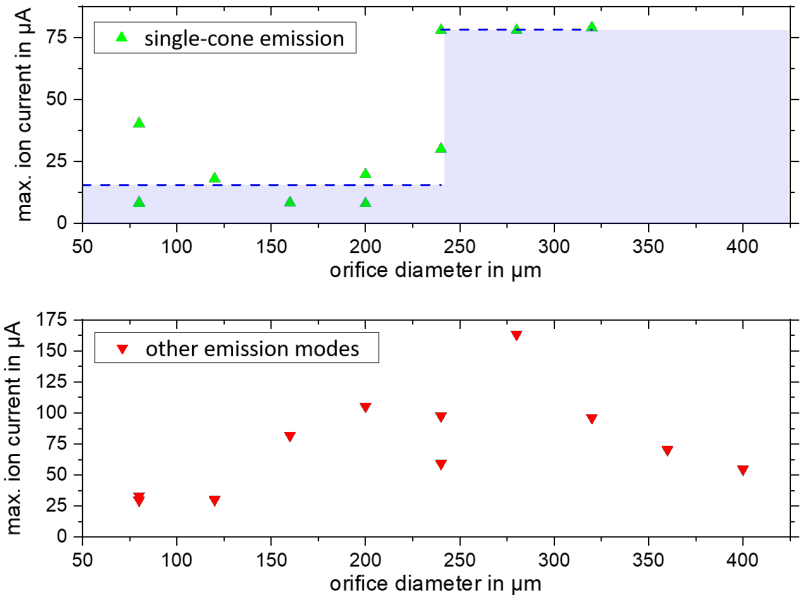

Figure 5.2: Data obtained on series (i) of emitters. Plotted is the maximum emission current against the orifice diameter for 21 emitters. Emitters exhibiting single-cone emission are plotted in the top graph and marked as green triangles. The other emission types are plotted in the graph below and marked as red triangles. For the single-cone emission a steep increase in extraction current can be observed around a orifice diameter of 240 µm. This sudden increase is marked in the top graph by the blue area. The experimental set-up used is described in chapter 3.

pressure in the reservoir. It is hypothesised that the presence of gas within the reservoir exerts a background pressure on the fluid, thereby influencing the equilibrium state and the formation of the Taylor cone. This may provide an explanation for the lower start-up voltages observed in some emitters. One potential avenue for testing this hypothesis would be to eliminate the possibility of trapped gas in the reservoir by redesigning the shape of the propellant tank. A revised tank geometry was devised in light of the observed issues, and further experimentation is required to substantiate the hypothesis. The schematic drawing of the newly developed reservoir is provided in Fig. A.5 in the appendix.

Another observation derived from the experiments is a potential correlation between the maximum emitted current and the diameter of the emitter orifice. As shown in Fig. 5.2 at orifice diameters of about 200 µm to 250 µm the maximal extracted current shows a visible step, increasing from about 10 µA to about 75 µA for single-cone emission. Nevertheless, this rise in the maximum emission current also leads to a decline in emission stability. As the orifice diameter increases, the occurrence of multi-cone emission and arcing also rises. An example is provided in Fig. 5.3, which depicts the distinction between single-cone emission and multi-cone

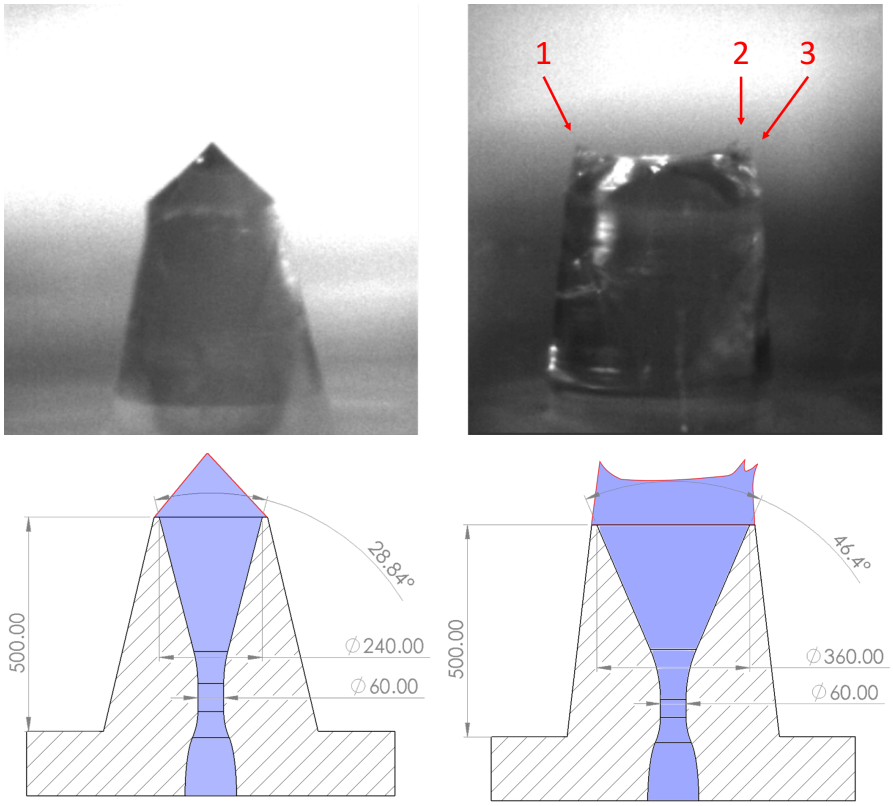

Figure 5.3: Two images extracted from a live video captured during an experiment. Each image depicts a single emitter, which is part of series (i) of samples designed to investigate the impact of emitter geometry on emission behaviour. The emitter shown on the left features a capillary opening of 240 µm at the summit and a diameter of 60 µm within the emitter. The emitter is operating in single-cone mode, with a very distinct Taylor cone visible at the emitter tip. The emitter depicted in the right image displays the same emitter geometry, but with an opening of 360 µm and a diameter of 60 µm within the emitter. As illustrated in the image, the emitter is operating in multi-cone mode, characterised by the presence of three visible Taylor cones. The Taylor cones are marked by red arrows in the image. It can be observed that the cones are emitting to the sides.

emission. Multi-cone emission is less favourable as in this emission mode several Taylor cones are dispersed on the emitter tip, as illustrated in the accompanying image, and are moved to locations not on the symmetry axis of the emitter. The emission from these cones typically hits the electrode or support structures, causing short circuits or arcing events. This significantly reduces the lifetime of the emitter assembly.

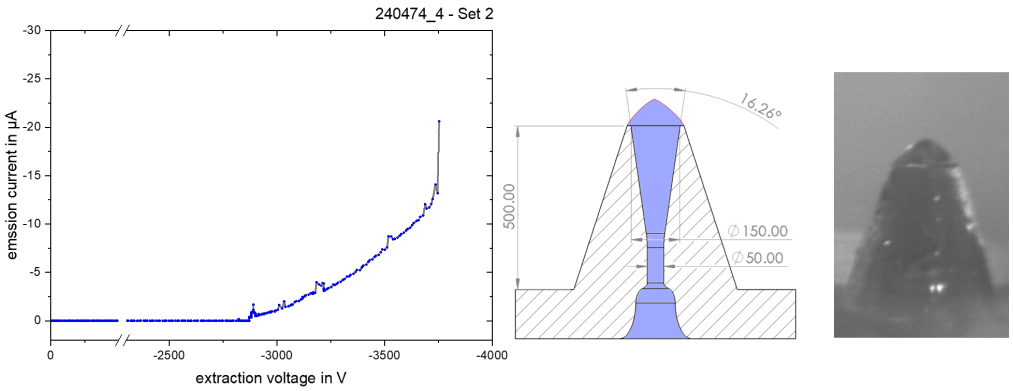

Figure 5.4: U-I plot, schematic drawing of the emitter and a single image extracted from the video capture of the experiment. This data was acquired using an emitter of the experimental series (ii). The emitter features an inner capillary diameter of 50 µm and an orifice diameter of 150 µm. The increased emission stability for these particular design parameters is supported by the extracted video image and the shape of the U-I curve. The Taylor cone depicted in the image shows no tilt and is very symmetric, indicating a stable state. Similar, the U-I curve shows very little disturbances for low values of the absolute extraction voltage down to -3700 V.

The variation approach (ii) concentrated on the examination of geometric changes pertaining to the inner capillary. In this experimental series, the same emitter geometry as before was used, depicted in the schematic drawing in Fig. A.1 in the appendix. However, in series (ii) the inner capillary diameter was systematically reduced from 50 µm to 20 µm in 10 µm increments. The emitter orifice diameter was fixed to 150 µm to achieve comparability between emitter sets. Three sets of 4 emitters, a total of 12 emitters, were fabricated and characterised. The intention of this geometry variation was to explore the possibility of reducing the propellant flow rate in line with the law of Hagen-Poiseuille and other literature discussed in chapter 2.

This approach showed very promising results. Reducing the diameter of the capillary within the emitter led to markedly different emission behaviour compared to the emitters tested in approach (i). The reduction in diameter leads to emitters operating in multi-cone mode at a weaker applied electrical field. This can be explained by the anticipated reduction in flow rate. As a consequence there is not enough fluid present at the emitter tip to consistently form a single large Taylor cone. This is also supported by the video captured during the experiment, that shows the emitter visibly emptying with increasing applied field strength. This effect was most pronounced for the emitters with a capillary diameter of 20 µm to 30 µm, which reinforces the conclusion about the reduced flow rate. These results confirm the possibility of controlling the flow rate by changing the inner capillary diameter, which constitutes a major improvement, as it allows for fine control of

the propellant flow in the emitter. The reduction in flow rate also beneficially changes the emission behaviour of several emitter geometries. While the emitters with a very low capillary diameter exhibit the aforementioned multi-cone emission behaviour, emitters with slightly larger capillary diameters of about 40 µm to 50 µm show an improved emission stability compared to the emitters used in series (i). Measurement data revealing the stability improvement is shown in Fig. 5.4 for the emitter with 50 µm capillary diameter. This leads to the hypothesis that emitter orifice and capillary diameter are directly linked and may have to be changed together to achieve the best results. The fixed orifice diameter of 150 µm was, presumably, too large for the 20 µm to 30 µm diameter capillaries to show stable emission. Further experiments have to be conducted to investigate the relationship between size of the emitter orifice and capillary diameter in more detail.

In the third series of samples (iii) a reduced distance of the emitter to the extraction electrode was investigated whilst the diameter of the extraction electrode orifice was kept constant at 1715 µm (see Fig. A.2 and Fig. A.3 in the appendix). The distance from emitter to the electrode orifice was reduced by 400 µm, from 700 µm to 300 µm bringing them significantly closer together, but at the same time increasing the opening half angle from 50° to 70°. The emitter design and variation was the same as for series (ii). The emitters from approach (ii) showed the best emission stability and therefore were the prime candidates to have the highest comparability in emission behaviour. Two sets of four of those emitters were fitted with the shorter spacer, resulting in a total of 8 emitters for this series.

The expected outcome was an increase in arcing events and instabilities as well as a reduced start-up voltage with decreasing distance between extraction electrode and emitter orifice. In contrast, the actual results showed an even further increased emission stability. Exemplary results are shown in Fig. 5.5. Since the emitter design is identical to the one used in Fig. 5.4, a direct comparison of the results from series (ii) reveals the increased emission stability and the influence of the reduced distance to the extraction electrode. The U-I curve plotted in the graph in Fig. 5.5 shows the very stable behaviour from 0 V to -3000 V. Around -3250 V the transition from single-cone emission to multi-cone emission is observable, as illustrated by the four images presented in Fig. 5.5. Correlating video sequence and current data shows clear demarcations when the emitter switches from single to multi-cone emission. Even in multi-cone mode no arcing was observed and the emission was, except for the area from -3500 V to -3800 V, very predictable. The reason for the decrease in emission current in area from -3500 V to -3800 V is still unclear. Most likely is that the propellant flow was reduced for a while due to debris or bubbles inside the propellant. However, gaining insight into the mechanisms underlying the transition from single-cone to multi-cone emission is significant.

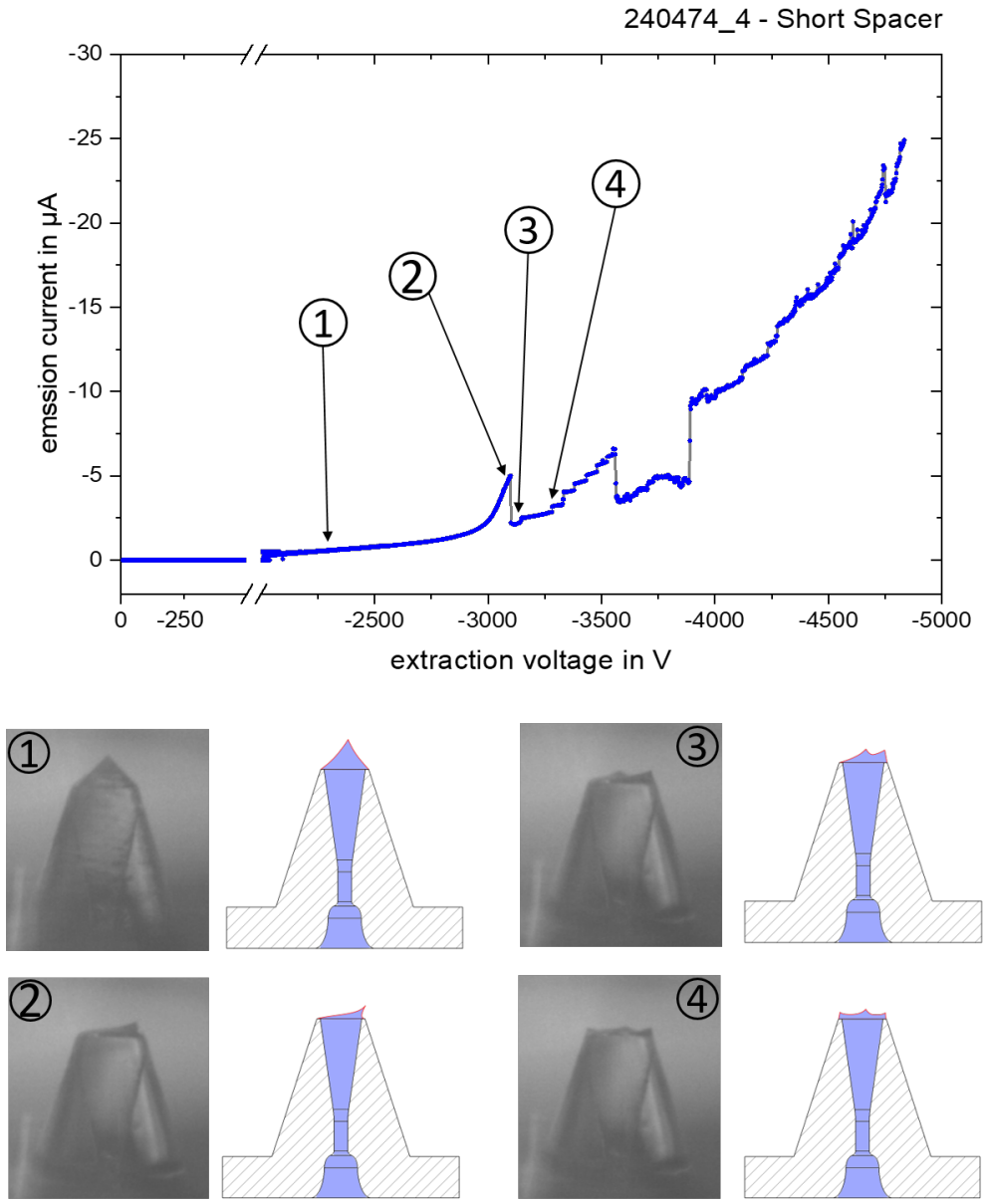

Figure 5.5: U-I plot, four images extracted from the corresponding video captures of the experiment and four schematic drawings of the emitter of series (iii) used in the experiment. The curve exhibits a characteristic exponential increase in current with rising extraction voltage. In the voltage range from 0 V to -3.1 kV the emitter operates in single-cone emission mode (1). At about -3.3 kV the emitter starts to operate in multi-cone mode as can be seen in picture (2) and subsequently (3). Further increasing the voltage results in more Taylor cones forming on the emitter tip (4). Each new cone can be referenced to a step in the U-I-curve.

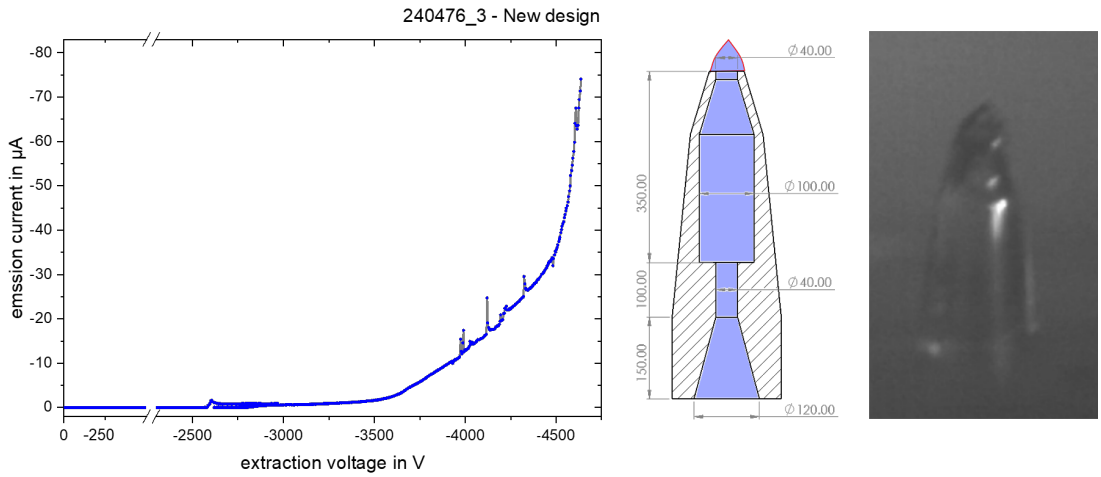

Figure 5.6: U-I plot, a single image extracted from the video capture of the experiment and schematic drawing of the emitter. For this measurement the newly developed emitter design (iv) was used, which intended to turn the lessons learned throughout series (i) to (iii) into improvements of performance. The schematic drawing of this emitter design can be found in Fig A.4 in the appendix. The emitter shown in this figure features an inner capillary diameter of 40 µm. The electrode design was that shown in Fig. A.2 in the appendix. The maximum extracted current reached about 75 µA and followed the characteristic exponential increase with rising voltage. No arcing was observed and the emitter operated very stably.

The most common modes of failure are arcing and short-circuit events, that damage the emitters. These events are typically caused by ionic liquid that forms a conductive bridge from the high voltage fluid to the grounded support structures of the electrode. In most cases unstable emission and multi-cone emission provide the necessary fluid for such short-circuit bridges. By eliminating the possibility of such events to occur the longevity of the emitter may be increased significantly. Therefore, predicting the transition mechanisms from single-cone mode to multi-cone mode will be crucial for developing strategies to enhance the longevity of the emitters.

In the experimental variation (iv) a new emitter design was devised, which is based on the lessons learned and results of the three preceding experimental series. The design intended to address multiple issues that became obvious during the other experiments, like overflowing or unwanted multi-cone emission. The technical drawing of the emitter can be found in Fig. A.4 in the appendix, that of the extraction electrode in Fig. A.2. Since beneficial design dimensions were unclear, a systematic variation very similar to the series (ii) was applied to the new design. The inner capillary was decreased from 50 µm to 20 µm in 10 µm increments. A total of eight emitters were fabricated.

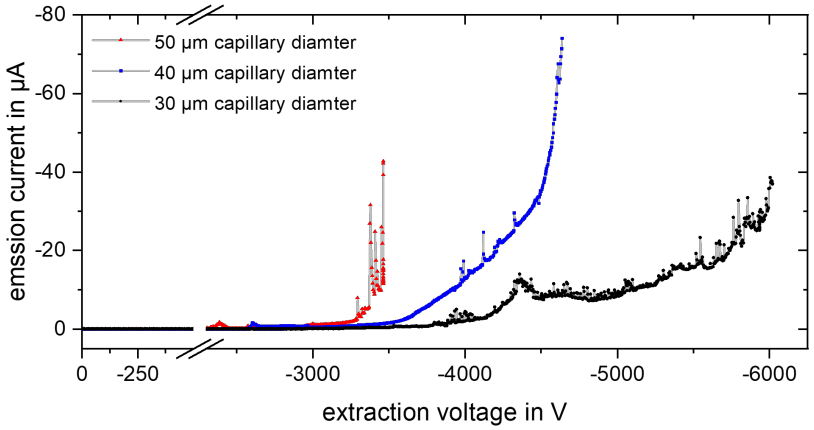

Figure 5.7: Three U-I curves for the emitters from series (iv) with an inner capillary diameter from 50 µm (red) to 30 µm (black). In direct comparison the U-I curve for the emitter with 40 µm (blue) capillary diameter shows the best performance. The results are similar to observations made during series (ii) and (iii), which can be attributed to too much or too little flow rate. The forth emitter with a capillary diameter of 20 µm had a manufacturing defect and was not fit for a comparison.

As can be seen in Fig. 5.6 and Fig. 5.7, the emitter of the new design with a 40 µm capillary diameter showed the best performance of this series. The emission was highly stable and achieved 75 µA at -4800 V at its best. Furthermore, no arcing was observed during the experiment, and only single-cone emission was evident. The other emitters from this series showed similar results, but with slightly reduced performance, which can be seen in Fig. 5.7. The emitters with larger and smaller capillary diameters showed the same issues observed for emitters of series (i) and (ii), which can be attributed to too much or too little propellant flow rate. Nevertheless, the new design demonstrates a lesser extent of this issue in comparison to the design utilised in (i) and (ii).

Besides the increased performance, the emitter design is also considerably more compact than the other designs, which in theory allows assembling more tightly packed arrays. Overall the implemented design changes intended to improve the emission behaviour yielded remarkably good results. This makes this design the most successful of all studied in this thesis.

A review of the literature reveals no examples of polymer-based 3D micro-printed electrospray emitters that can be directly compared to the results obtained on emitter of series (i) to (iv). Nevertheless, there are analogous electrospray concepts with comparable emitter dimensions, geometries, and fabrication methods that allow a comparison.

An example for a comparable emitter design in terms of size and manufacturing method is the electrospray system developed at Cornell University. They utilise 3D lithography to manufacture porous emitters from silica glass beads. Their emitter design is comparable in size and shape to the one used in series (i), with a conical structure ranging from 300 µm at the base to 5 to 10 µm at the tip. Their emitter was capable of emitting up to 2 µA in current in both polarities [50]. The new design presented in series (iv) vastly outperforms these results with a maximum current per emitter of about 75 µA. Furthermore, the design from series (iv) has a smaller footprint with only 150 µm diameter at the base.

Another example of a comparable electrospray system is the PET-50, from the Southampton University. The PET-50 is based on porous emitter fabricated using SLA 3D printing and features four thruster heads each fitted with 313 individual emitters resulting in a total of 1252 individual emitters. The specific design dimensions of an individual emitter are unknown. This system is currently tested for flight readiness. It is already fully integrated in a 1 U form factor. In this state the system achieved an emission current of 1394 µA at -3400 V [99]. This translates to about 1 µA per emitter. Even when compared with this more developed and flight ready thruster assembly, the results of the experimental series (iv) are very promising. However, it should be mentioned, that the PET-50 primarily operates in pure ionic mode at a specific operation point. This means, that the reported 1394 µA are not the maximal achievable current of the system, but represent the upper limit of the nominal operation current. Nevertheless, the emitters characterised in series (i) to (iv) all showed comparable or better results in terms of emission current.

A third comparable emitter design is the capillary type electrospray system developed at UC Irvine. Their emitters feature a straight cylindrical capillary etched from a silicon substrate. They reported capillary sizes ranging from 275 µm down to 40 µm, making them very similar to the emitters used in series (iv). Furthermore, their design also features an integrated extractor electrode, with a distance of about 300 µm from emitter to electrode. They reported an emission current of about 0.3 µA per emitter. However, their system employed hydraulic resistance channels and an active feeding system, with the goal of only supplying a minimum amount of propellant to each emitter, therefore, operating at below maximum capacity [100]. The emitters used in series (iii) and (iv) exhibit a high degree of similarity with regard to their design parameters, and demonstrate a comparable performance to their system. The emission of the emitters from series (iii) shown in Fig. 5.5 in the voltage range from -2000 V to -3100 V may be best compared with those results because of the intentional limiting of the flow rate. The emitters from series (iii) outperform the emitters from the University of Irvine by a factor of about 10 or higher.

5.2 Future avenues and research opportunities

The technology of 3D micro-printed electrospray thrusters improved significantly in a very short period of time. This is due to the incredibly short prototyping time and fast design adoption achievable due to the feasibility of the technology. Based on the results achieved with the geometry parameter variation presented above, there are several promising avenues for improvements and further developments.

One possible way forward could be array fabrication. The feasibility of fabricating identical emitters into large arrays has already been demonstrated during this project. An investigation into the potential of emitter arrays would improve the capabilities of this technology as an electric propulsion system. Using the scalability of electrospray emitters to its fullest, in combination with fast prototyping, freedom of design, and modularity provided by the 3D-lithography process, this technology may become very successful in the field. However, beside the obvious advantages of the array approach, there are some challenges that need to be faced. One challenge is the interaction between emitters in close proximity to each other. The proximity of the emitters may have an effect on the emission behaviour. It seems reasonable to assume that such an effect would be observed in the field distribution in the vicinity of the emitter tips, as has been discussed in the literature. Furthermore, it may be assumed that the provision of propellant by the same reservoir may affect the performance, for example due to "communicating pipes". Devising emitter geometries that are not impacted and behave predictably in terms of array positioning is essential to overcome this challenge.

As already pointed out above, a revision of the fluid feeding system is essential. Some work in this regard has already been started, with the recently developed passive feeding reservoir included in Fig. A.5 in the appendix. A revised fluid system that allows for long term testing and provides a predicable propellant flow would be very beneficial for the technology of this emitter technology as a whole. If a passive or an active feeding system will be best, has to be investigated in the future.

Other aspects worth exploring are different operation points for the emitters. As described in the chapter 2, electrospray emitters can emit ions in very different modes. Pure ionic mode is the preferred operation mode, due its high efficiency. However, other modes may also be beneficial. Mapping emitter operation in dependence on operational parameters such as flow rate, extraction voltage and polarity, may yield insight on how to operate these emitters in different modes. This could yield more flexibility in the application in an electric propulsion system.

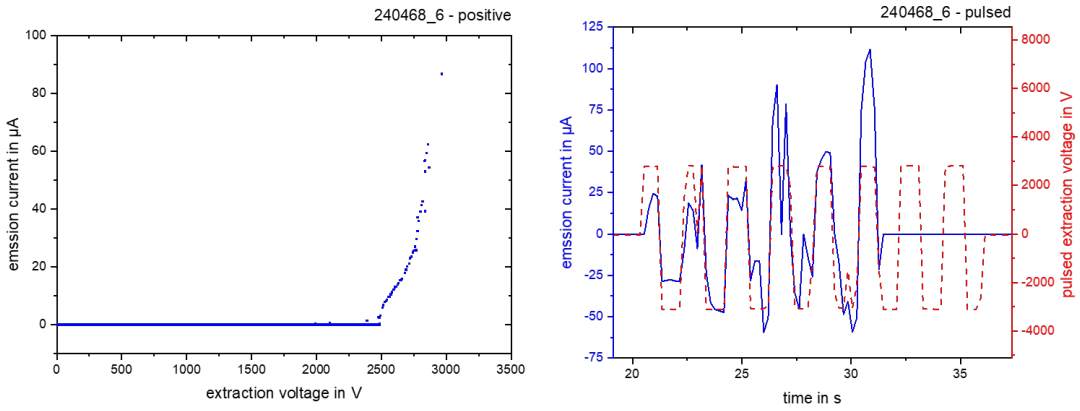

Figure 5.8: Data obtained during approach (i), consisting of a U-I curve for emission in positive polarity and a time resolved plot of the extraction current and high voltage for pulsed emission. The emitter used for these experiments features a 240 µm orifice and a 60 µm inner capillary. Most of the experiments in the series (i-iv) were carried out in negative extraction polarity to ensure comparability. The data shown here was collected as a prove of concept for multi polarity operation.

Since the different modes vary in the required operation parameters, with some emission modes only occurring at specific propellant the flow rates, a controllable flow rate may be necessary. If the flow rate needs to be adjusted directly, an active system of some kind is required. The tool to identifying different emission modes may be time-of-flight mass-spectrometry. This technique was already discussed during the project and can provide the necessary insights, like beam composition, ion velocity and ion energy to determine the emission mode.

Very closely related to the characterisation of the operation space is the adaptation of multi-polarity ion emission. As for now, ion emission was primarily achieved using negative high voltage for emitters discussed in this work. However, electrospray emitters using ionic liquids are capable of emitting ions in both positive and negative polarity. This capability has also been proven by the experiments conducted during this project for example in the publication IV in section 3.6. Nevertheless, this possibility was hardly explored, due to the unstable emission behaviour until recently. With the recent advancements, stable emission both polarities as well as in pulsed mode was confirmed and achieved reproducibly. Fig. 5.8 shows data collected during the experimental series (i) as proof of concept for multi-polarity and pulsed operation. As the focus of the experimental series was on the influence of the geometry, only a few experiments were carried out with positive and pulsed extraction voltages. With the stable emission in both polarities, a new avenue to devising a control scheme to operate the emitters in a pulsed emission mode opens up. The few experiments conducted using pulsed mode showed promising results.

This could be a worthwhile investigation, as pulsed ion emission would increase the electric propulsion capabilities of this technology, in particular as neutraliser usage may be avoided this way.

Additionally, it may prove beneficial to investigate alternative materials for the emitter structures. The 3D lithography device used to manufacture the emitters is also capable of producing pure silica glass models, if a secondary sinter process is applied. By changing the material to a glass-based kind, the longevity and emission behaviour may be further improved. Furthermore, the use of glass as a material allows for the utilisation of liquid metal as a propellant, given that glass is capable of withstanding higher operational temperatures.

Setting aside the goal of developing an electric propulsion system, this technology may also be interesting for mass spectrometry or material processing. The high modularity and capability to provide ions at a wide range of extraction energies may be interesting for the aforementioned applications.

In conclusion, the potential avenues of inquiry in this research field are contingent upon the intended application and the desired outcome. The objective of further research into a propulsion system may differ from that of fundamental science issues. It is now possible to define the future direction of the research idea of 3D lithographically fabricated electrospray emitters, given that the underlying technology has been validated during this project.

Appendix

A.1 Additional conference publication RGCP 2021

This conference publication precedes the initial journal publication and contains an unedited version of some findings. It should be noted that this publication does not represent any advancement that has not already been mentioned. It features some more in depth methods that were inconsequential in comparison to other findings. Accordingly, this publication has been relocated to the appendix as supplementary material.

F. Kunze wrote the first draft of the manuscript. The manuscript underwent revision by all of the contributing authors. The experiments and data acquisition were conducted by F. Kunze and L. Hanstein. B. Mogwitz provided help with the focused ion beam device. Furthermore, P. Klar and T. Henning provided supervisory and project management oversight.

Fabrication of internally wetted electrospray emitters by 3D microlithography and characterisation by destructive imaging

F Kunze, L Hanstein, B Mogwitz, T Henning and P J Klar

I. Physikalisches Institut, Justus-Liebig-Universität Gießen, Heinrich-Buff-Ring 16, 35392 Gießen, Germany

E-mail: fynn.kunze@physik.uni-giessen.de

Abstract. Electrospray microemitters with capillary diameters of a few micrometres were fabricated by 3D microlithography (two photon lithography) in the photostructurable polymer SU-8. Results on the optimisation of the writing process are presented. The quality of the emitters, especially the continuity of the capillaries, was demonstrated by destructive imaging, namely, by mechanical grinding of emitters embedded in resin and by precision milling with a focussed ion beam, respectively, followed in each case by scanning electron micrography.

1. Introduction and motivation

Small and micro satellites have become more and more relevant for commercial and scientific applications in the past decade as these small satellites are cheaper to launch compared to conventionally sized satellites, while still offering vast mission possibilities. Constellations like OneWeb or Starlink are prominent examples for applications of small satellites. For constellation flights, accurate position and attitude keeping of the members of the constellation as well as a good fuel economy are important. Furthermore, scientific missions like LISA, also require precise orbit and attitude control with very small impulse bits and with a low thruster noise, which can be provided by miniaturized thrusters [1, 2, 3].

These requirements demand the development of precise miniaturised thrusters fitting on a very small satellite with possibly only a few litres of volume. Electric propulsion systems are most likely to fulfil these requirements. Therefore, the scaling-down of existing and proven electric propulsion systems systems is a logical approach [1].

However, upon the scaling-down of existing systems, some problems are encountered. For plasma based thruster for example, it becomes harder to generate a stable plasma as the plasma vessel is scaled down due to the increasing surface-to-volume ratio, resulting in poor efficiency. Bulky components that do not fit into small satellites and high power consumption are some known challenges [4].

Therefore, instead of relying on the scaling down of existing technologies, developing new miniaturised thruster is a necessity. One candidate are electrospray emitters, also known as colloid emitters. These are very scalable and even profit from scaling down as they become more efficient with reduced geometric dimensions. The general concept behind electrospray emitters

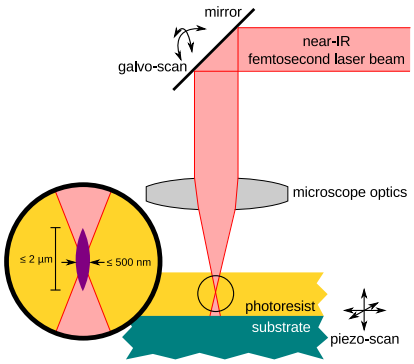

Figure 1. Principle of 3D microlithography (two-photon-laserlithography).

is the use of a static electrical field to extract ions [5] from a liquid propellant and accelerate them, thus creating the thrust.

Possible propellants are liquid metal or ionic liquids. If ionic liquids are used, both positively and negatively charged ions can be extracted from the propellant, eliminating the need for external neutralisers [6]. There are three types of electrospray emitters [7], namely, internally wetted or capillary type emitters, externally wetted emitters, and porous emitters. Of these three types we shall focus on the internally wetted or capillary type emitters, using an ionic liquid as propellant. There are primarily two fabrication technology families for capillary emitters. The first one is the silicon based fabrication, which has been successfully applied in the Unites States and Europe [8]. The other path, which this paper is focused on, is the use of photolithography and photopolymers. The emitters and all possible parts are created using photolithography as core technique and photopolymer, in our case SU-8, as base material. SU-8 is a negative tone resin, which distinguishes itself due to high mechanical stability and resistance against harsh external influences. In the past, planar photolithography was employed to create stacked structures, thus creating quasi-3D emitters. A combination of planar photolithography and 3D microlithography demonstrated the possibilities offered by 3D microlithography, especially the freedom of design [9]. The next step is to fully utilise the 3D lithography to manufacture emitters and emitter arrays without additional planar lithography steps.

2. 3D microlithography

The general principle of operation is shown schematically in Fig. 1. 3D microlithography systems, also known as two-photon-laserlithography, use a near infrared femtosecond fibre laser with a standard wavelength of about 1080 nm, which in further modulated to 780 nm. Single photons emitted by the laser carry too little energy to trigger a photochemical reaction in the photoepoxy, thus passing through it unhindered. However, this changes when the laser beam is focussed through microscope optics, providing such a high intensity in a small volume element (voxel) near the focus, that two-photon processes occur at a statically high rate. The energy of the two photons combined is sufficient to trigger a photochemical reaction. By scanning the focus through the photoepoxy in three dimensions, structures can be written with a very high degree of design freedom and a spatial resolution down to a few hundred nanometres. This can be achieved by either changing the beam path via mirrors (galvo-scan) or changing the sample position (piezo-scan).

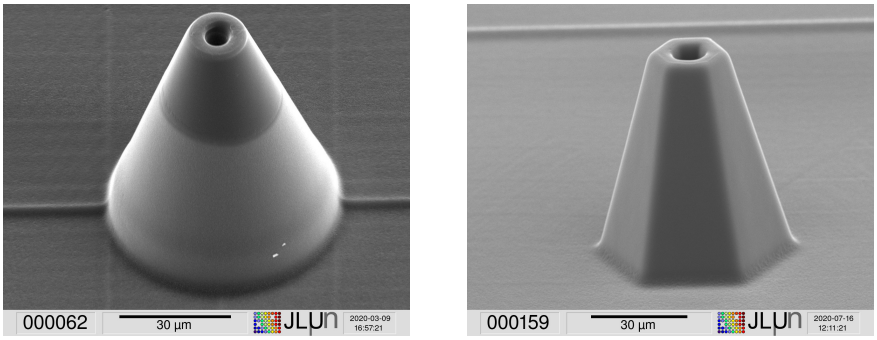

(a) **(b)**

Figure 2. SEM pictures of pure SU-8 micro capillary emitters. Both emitters were fabricated in a single exposure step using 3D microlithography (two-photon lithography). The emitters are placed on a handling base which is also written by the exposing laser beam. The capillary extends through the whole structure including the base. On the left (a), a typical conic micro emitter is shown. The stitch between two chunks of the base plate can be seen crossing the emitter base from left to right. The discolouration near the tip is likely a result of the metallisation process carried out prior to the SEM investigation. On the right (b), an emitter with a hexagonal cross section is shown. This emitter was fabricated using similar parameters like those used for the emitter on the left.

3. Single emitters

The first step in creating functional emitter arrays is the fabrication of single emitters which then can be assembled into an array.

3.1. Emitter structure

Single emitters fabricated in SU-8 photopolymer with only 3D microlithography are shown in Fig. 2. The conic emitter on the left demonstrates the three main features: firstly, the capillary carrying the propellant to the extraction site at the tip of the cone, secondly, the cone itself, shaped to improve the electrical field distribution at the tip and to reduce the chance of propellant overflowing and wetting the surface, and, thirdly, the base plate that separates the outside (vacuum side) from the inside (propellant reservoir).

3.2. Fabrication parameters

For the fabrication of the emitters shown in Fig. 2 the Nanoscribe PPGT 3D microlithography system was employed. As substrate, a 280 µm thick Si wafer (100 surface orientation) with a spin coated layer of 100 µm of SU-8 was used. The Nanoscribe was used in the 20 × objective, mask-less (air gap) configuration. In table 1, all process relevant parameters are listed. The whole emitter was programmed in the GWL language which is directly processed by the device. GWL is comparable with G-Code most commonly employed in 3D printing and CNC manufacturing. As the system can only operate a field of view with a diameter of 600 µm with the 20 × objective, the structure has be cut into smaller pieces, so-called chunks. Each chunk overlaps a little with adjacent chunks (stitching). A corresponding seam can be observed in the left hand image in Fig. 2. The shape of the chunks can be adjusted, in this case, a quadratic base of 250 µm × 250 µm was chosen. To optimise the writing time, a “shell and scaffolding” technique was used: only the bottom, the walls and the top of each chunk were written, leaving unexposed resin inside each chunk. Bottom and top were written 3 µm thick, while the walls were 5 µm thick. This proved to

Table 1. Process parameters used in the GWL code for the fabrication of single emitters with the Nanoscribe PPGT 3D microlithography system

parameter	value
slicing distance	0.3 µm
hatching distance	0.3 µm
scanning speed	50000 µm s^{-1}
base plate lateral size	2 mm × 2 mm
base plate height	20 µm
emitter height (height over substrate)	60 µm (20 µm+40 µm)
emitter diameter at base	30 µm
chunk size	250 µm × 250 µm
writing time	132 min

result in sufficient structural stability until the later fabrication steps. Leftover unexposed resin is flood exposed after the developing step using a UV light source, thus forming a solid material. The shell and scaffolding technique results in a much shorter overall writing time. After the writing process the structure was developed using mr-Dev 600 developer. The flood exposure was done in a Suss MA 56 mask aligner with a high pressure mercury lamp and is only applied to the base plate and not the emitters. To separate the structure from the silicon substrate, the wafer was placed in a potassium hydroxide solution with 27 % concentration at 80 °C over the course of two to five hours depending on the wafer. The structures may separate from the wafer with some parts of the wafer still intact, eliminating the need to fully dissolve it.

3.3. Freedom of design

As shown in the right hand image in Fig. 2, the emitter shape can be defined with great freedom of design within the 3D microlithography process. A hexagonal cross section was chosen for the emitter, as well as for the chunks of the base plate in this example. This degree of freedom of design cannot be achieved with planar lithography and neither with silicon technologies. It can also be applied to the internal structures of the emitter, creating for example capillaries with non-circular cross sections or with more complex internal surface structures, like fins or meanders. This may influence the emission behaviour of the emitters and needs to be examined further.

4. Arrays and systematic variation

4.1. Arrays

In the left image of Fig. 3, an array with 25 individual emitters is shown. Such an array may later be part of a larger array. Each single emitter has a footprint of approximately 30 µm × 30 µm. This translates into an emitter density of 1100 emitters per square millimetre. By changing the spacing and position of the emitters an even higher density may be possible. For any array of emitters highly uniform individual emitters are essential since variations in parameters, especially geometric dimensions, between them may render the emission behaviour unpredictable. Therefore, it is necessary that the fabrication process yields uniform emitters when the same GWL code is used. The emitters in Fig. 3 on the left were written using the same GWL base code and only changing the relative starting position of the writing process. There are minimal to no visible differences between the single emitters.

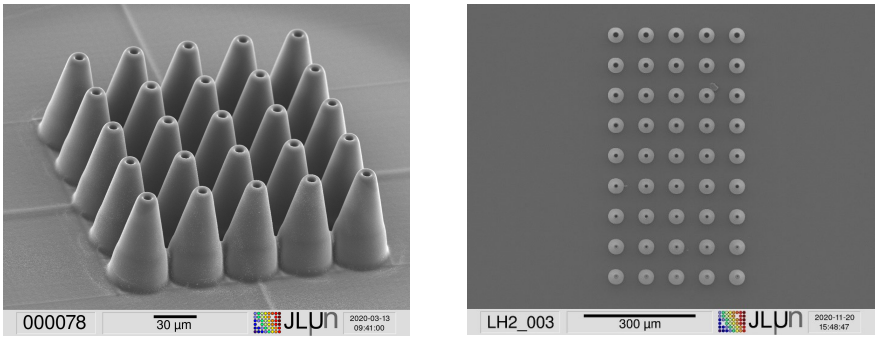

(a) **(b)**

Figure 3. SEM images of an array of nominally identical emitters (a) and of an array of systematically varied emitters (b). The individual emitters in the left hand image are 40 µm in height over the base plate, have a diameter of 20 µm at the base and a capillary diameter of 8 µm. On the right hand side, a systematic variation in capillary diameter is shown. The five emitters in one row are identical. From top to bottom, the capillary diameter starts at 16 µm and is reduced by 1 µm with each consecutive row down to a capillary diameter of 8 µm on the last row.

4.2. Systematic variation of parameters

An important advantage of defining the structures to be lithographed as programme code, GWL in this case, is that systematic variations of geometric parameters can easily be implemented, by looping over chosen variables in an array of test structures. In Fig. 3 on the right hand side an array of emitters (without base plate) is shown. The capillary diameter is systematically reduced from top to the bottom row, starting at 16 µm at the first row and decreasing in 1 µm steps to 8 µm in the bottom row. The whole array was fabricated using the same GWL-code with only iterative adjustment to the diameter variable. This allows for combining emitters with different parameters into an array in a single process step. This is difficult to achieve with other fabrications techniques such as planar photolithography, because for each capillary diameter a different mask is necessary.

5. Characterisation by destructive imaging

Quality assurance of the capillary is essential in establishing a fabrication process for internally wetted electrospray emitters. Important issues are the continuity of the capillary and the homogeneity of its diameter over its entire length. These qualities can only be evaluated by subjecting samples to destructive testing with subsequent microscopic imaging. In the first approach we used a grinder with sandpaper of different grit to grind down emitters embedded in epoxy resin to achieve a cross-section. The silicon substrate was in this case removed after embedding and before starting the grinding process. In the second approach we used a focused ion beam (FIB) with xenon ions to make free-form cuts in emitter test structures on their silicon substrate. The results, exemplary shown in Figs. 4 and 5, confirm both that the capillaries were continuous for sufficiently large diameters and that the diameter did not vary significantly over the capillaries' length.

5.1. Grinding

To achieve a clean cross-section view of different emitters and each reveal the capillary layout, an array of emitters with systematically varied capillary diameter was written onto a silicon

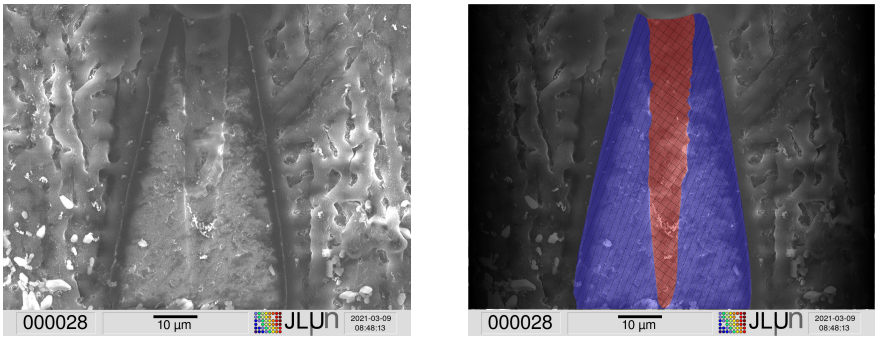

(a) **(b)**

Figure 4. SEM image of a cross-section of a capillary micro emitter (a). The emitter was embedded in epoxy resin, the silicon substrate dissolved in a potassium hydroxide solution, and the sample was ground with sandpaper of grits 240, 600, and 1200, respectively, until the capillary of the emitter was visible in an optical microscope. The sample was metallised via sputter disposition with few nanometres of gold for imaging in a scanning electron microscope. The emitter was not embedded perfectly at a 90-degree angle to the sanding surface. Therefore, the cross-section shows an oblique cut. On the right hand side (b) the emitter is highlighted in stripe-hatched blue and the capillary in cross-hatched red. The nominal capillary diameter is 13 µm.

die. To make it easier to observe the emitter, no base plate was written. The emitters on their substrate were embedded into a clear epoxy (bisphenol-a-epichlorhydrin). After the resin had cured, the silicon substrate was dissolved with potassium hydroxide, leaving only the emitter cones embedded in the resin. This allowed a clear view on the bottom of the emitters in an optical microscope. It was confirmed that the diameters of the capillaries at their bottoms (facing the tank side) matched those at the top (facing the vacuum side) within measurement accuracy, and thus, that capillaries that appeared to be continuous in non-destructive imaging inspection still appeared to be continuous when viewed from the substrate side. Afterwards the emitters were ground with an automated grinder with 240 grit sandpaper in steps down to 1200 grit sandpaper. Between the steps of sanding the emitters were inspected periodically to check if a clean cross-section was visible. The process was repeated until a clean cut was achieved. After metallising the grinding surface via sputter disposition with gold, SEM images were taken. A typical image is shown in Fig. 4. The capillary is clearly visible in the centre of the emitter. The emitter was not perfectly embedded at 90-degree angle to the sanding surface, leading to an oblique cross-section of the cut with the capillary. At the tip an orifice of approximately 12 µm to 13 µm can be observed, which is matching the nominal (programmed) diameter within micrometre accuracy. The capillary and emitter are highlighted in the right hand side image in Fig. 4. Furthermore it can be stated that the whole emitter shows a very good overall fabrication quality. There are no visible cracks or defects. The surface quality of the capillary seems also very good with only residual remains from the metallising process.

5.2. Cross-section via focused ion beam (FIB)

As second approach to make the internal layout visible a xenon focused ion beam etching system was employed. A similar emitter array as described in section 5.1 was fabricated. The emitters were metallised with gold to facilitate the FIB process by reducing charging. Various orientations of the ion beam milling direction relative to the intended cross section plane were tested. When

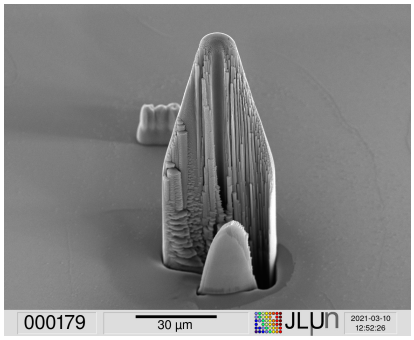

Figure 5. SEM picture of a capillary microemitter in cross-section produced with a focused ion beam. The emitter has a height of 70 µm including the base and a capillary diameter of 8 µm. The capillary opening is visible in the centre. Due to the FIB cut some artefacts, so called rippling, are visible.

milling exactly parallel to the cutting plane, a deterioration of the emitter at the cutting plane was observed, very likely due to local heating. The best results were achieved by orienting the milling direction in a right angle to the plane of the cut, at the expense of the so-called rippling of the cross-section visible in Fig. 5. The emitter shown in Fig. 5 has a nominal diameter of 8 µm. The capillary is visible through almost the whole emitter. At the base, no clean cut was be achieved under the non-optimised conditions in this test run. The surface quality of the capillary appears to be very good and matches the results discussed in section 5.1. The true capillary diameter seems to be around 6 µm to 7 µm. This may be a consequence of the fabrication process as the writing voxel of the 3D lithography device has a diameter of its own. How much the real emitter diameters differ from the programmed nominal diameter has yet to be fully determined.

6. Conclusion and outlook

The results show that the fabrication of internally wetted electrospray emitters for electric propulsion application entirely in 3D microlithography is feasible. The emitters exhibit a high surface quality as well as a well-defined and clean capillary. Even at single digit micrometre diameters the capillaries are continuous, homogeneous in diameter, and show little signs of defects. Furthermore, emitters can be manufactured with precision and reproducibility allowing uniform arrays to be reliably fabricated. The next step will be to characterise the ionic emission of emitters fabricated as shown above. A further possible development path is the application and fabrication of complex geometries and capillary layouts deviating from straight, uniform-diameter capillaries, especially to tackle the challenge of achieving a sufficiently high fluidic resistance, which is a common difficulty in internally wetted emitter fabrication.

Acknowledgments

EU regional funding via the EFRE scheme of the State of Hesse is gratefully acknowledged.

References

[1] Lemmer K 2017 *Acta Astronautica* **134** 231–243
[2] Gonzalez del Amo J 2015 European Space Agency (ESA) electric propulsion activities *34th Int. Electric Propulsion Conf., Kobe* IEPC-2015-02
[3] Krejci D and Lozano P 2018 *Proceedings of the IEEE* **106** 362–378
[4] Holste K *et al.* 2020 *Review of Scientific Instruments* **91** 061101
[5] Taylor G I 1964 *Proceedings of the Royal Society of London. Series A. Mathematical and Physical Sciences* **280** 383–397
[6] Mueller J 1997 Thruster options for microspacecraft - a review and evaluation of existing hardware and emerging technologies *33rd Joint Propulsion Conf. and Exhibit* AIAA 97-3058 (American Institute of Aeronautics and Astronautics, Inc.)
[7] Peter B S, Dressler R A, Chiu Y h and Fedkiw T 2020 *Aerospace* **7** ISSN 2226-4310

[8] Dandavino S, Ataman C, Ryan C N, Chakraborty S, Courtney D, Stark J P W and Shea H 2014 *Journal of Micromechanics and Microengineering* **24** 075011
[9] Henning T, Huhn K and Klar P J 2019 Characterisation of electrospray microemitters fabricated by planar and 3d photolithography *36th Int. Electric Propulsion Conf. (IEPC), Vienna* IEPC-2019-344

A.2 Schematic drawings

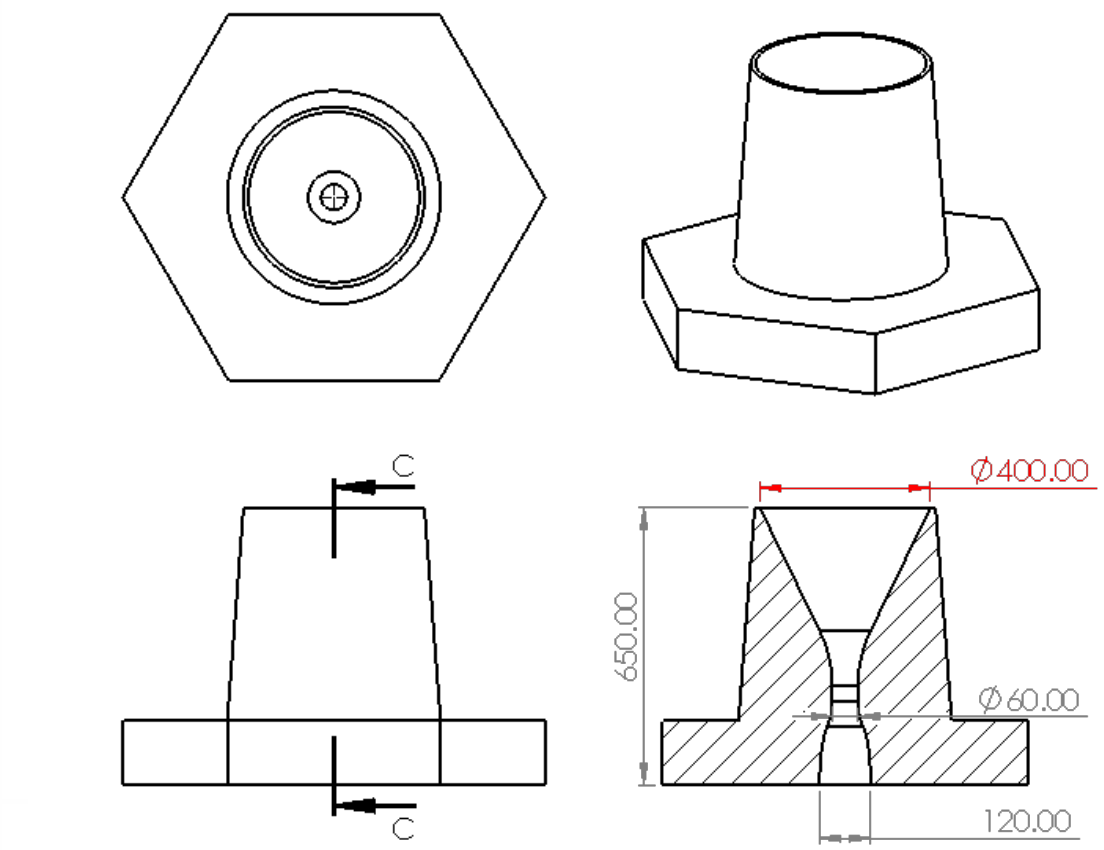

Figure A.1: Schematic drawing of the emitter design for series (i) presented in Chapter 5. The design was systematically changed by reducing the orifice (marked in red) from 400 µm to 40 µm in diameter in 40 µm steps. The other parameters remained unchanged as far as possible. Only parameters directly correlated to the orifice diameter, like the orifice angle, were changed along the diameter to achieve a viable geometry.

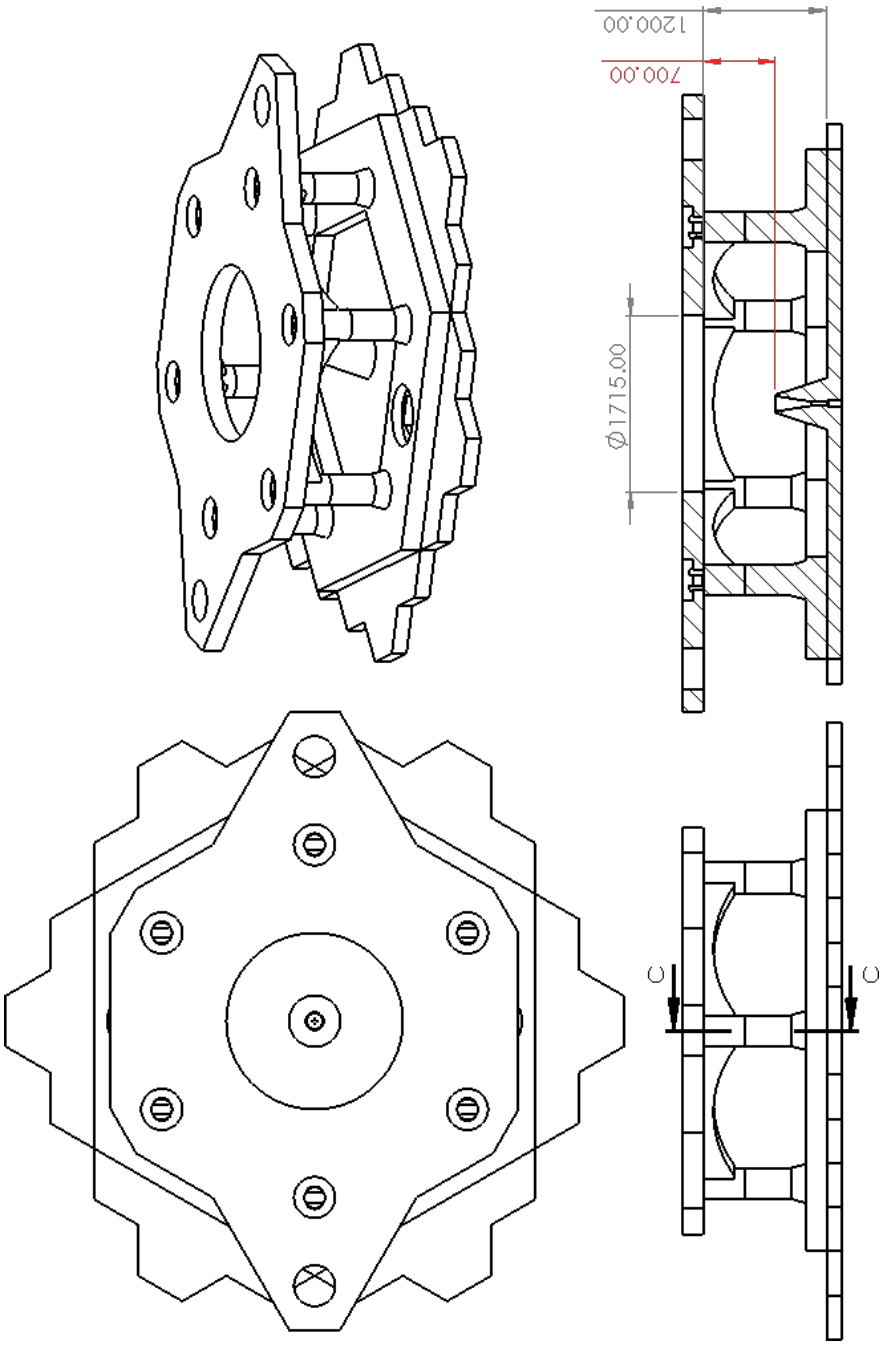

Figure A.2: Schematic drawing of the electrode used for series (i), (ii) and (iv). The electrode orifice diameter is 1715 µm and was not changed for any of the series. Marked in red is normal distance of the emitter tip to the metallised plane of the electrode, which was set to 700 µm for series (i), (ii) and (iv).

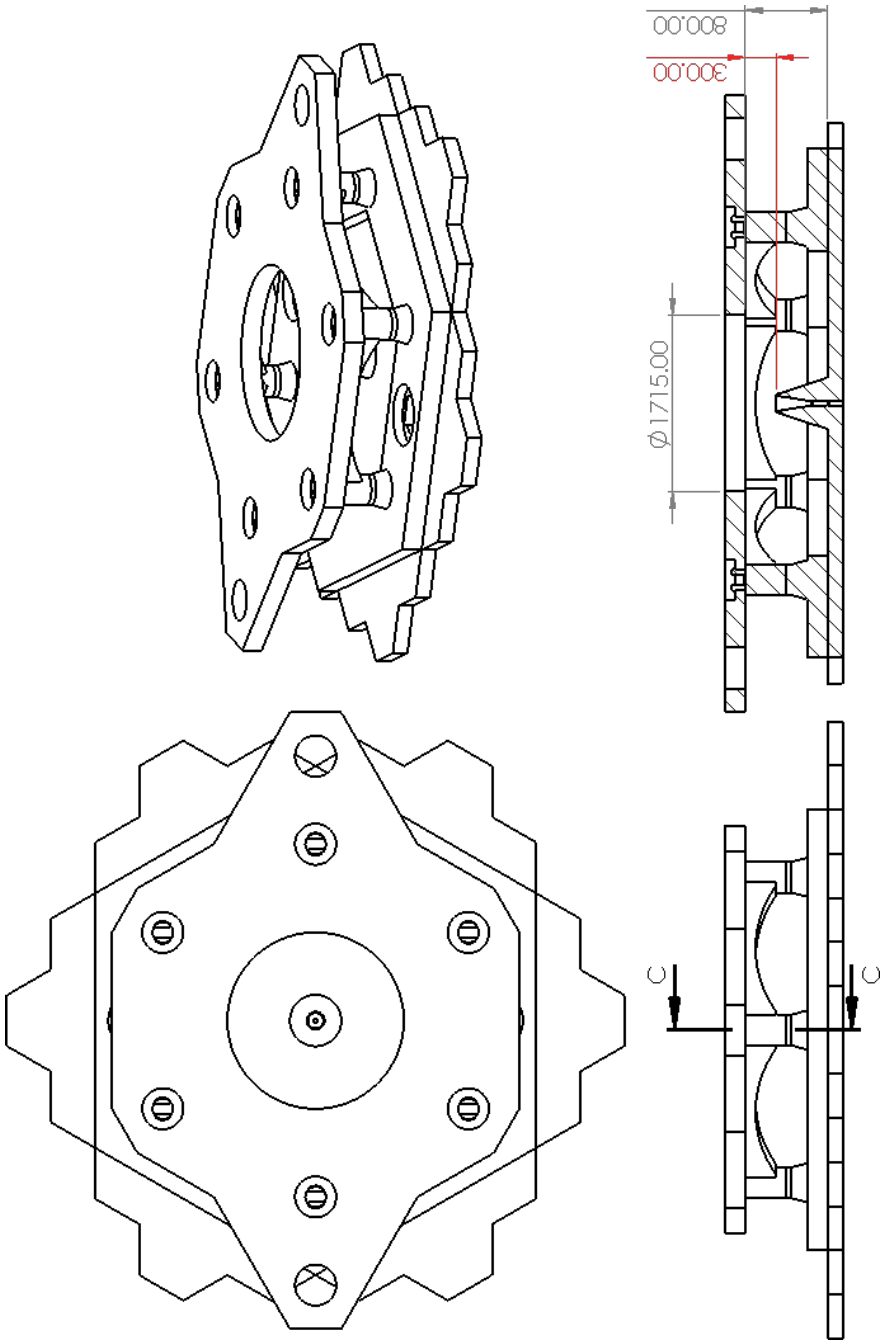

Figure A.3: Schematic drawing of the electrode used for series (iii). The electrode orifice diameter is 1715 µm and was not changed. Marked in red is normal distance of the emitter tip to the metallised plane of the electrode, which was reduced to 300 µm for series (iii).

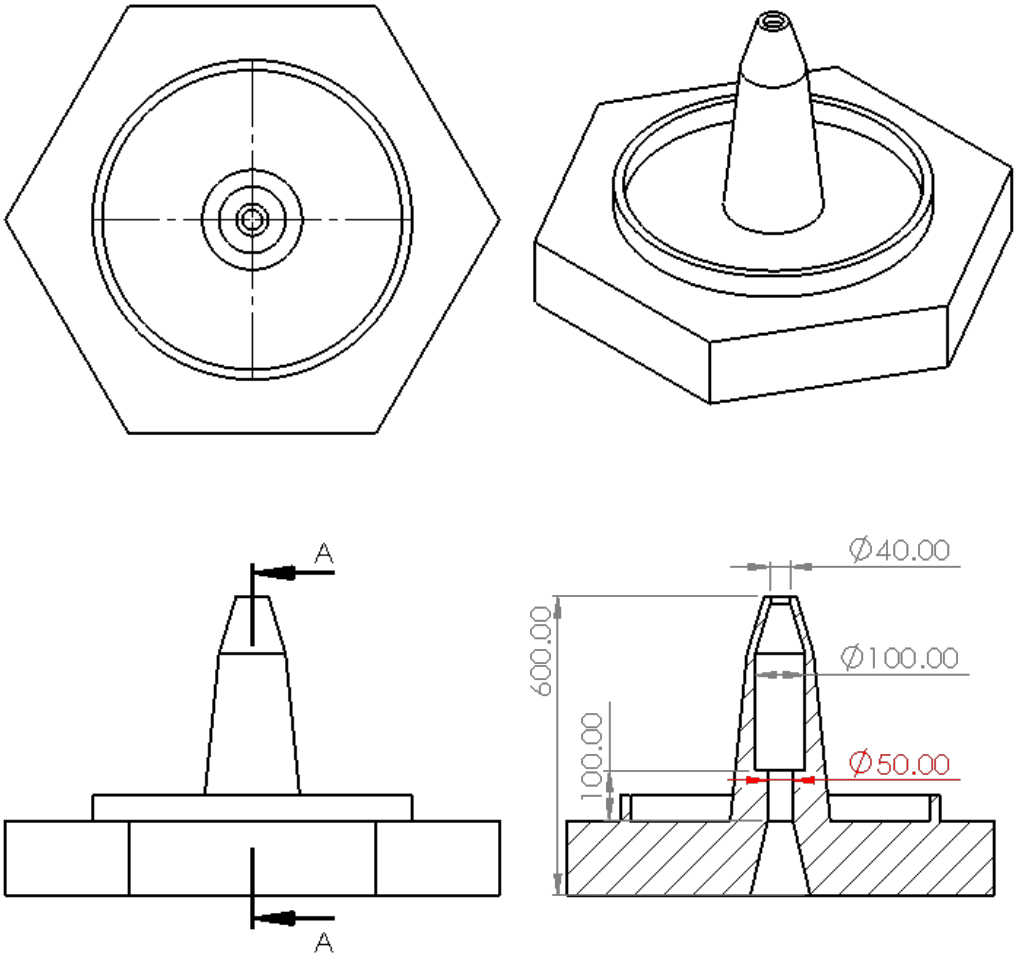

Figure A.4: Schematic drawing of the emitter design for series (iv) presented in Chapter 5. The design was systematically changed by reducing the inner capillary (marked in red) diameter from 50 µm to 20 µm. The other parameters remained unchanged as far as possible. Only parameters directly correlated to the orifice diameter, like the orifice angle, were changed along the diameter to achieve a viable geometry.

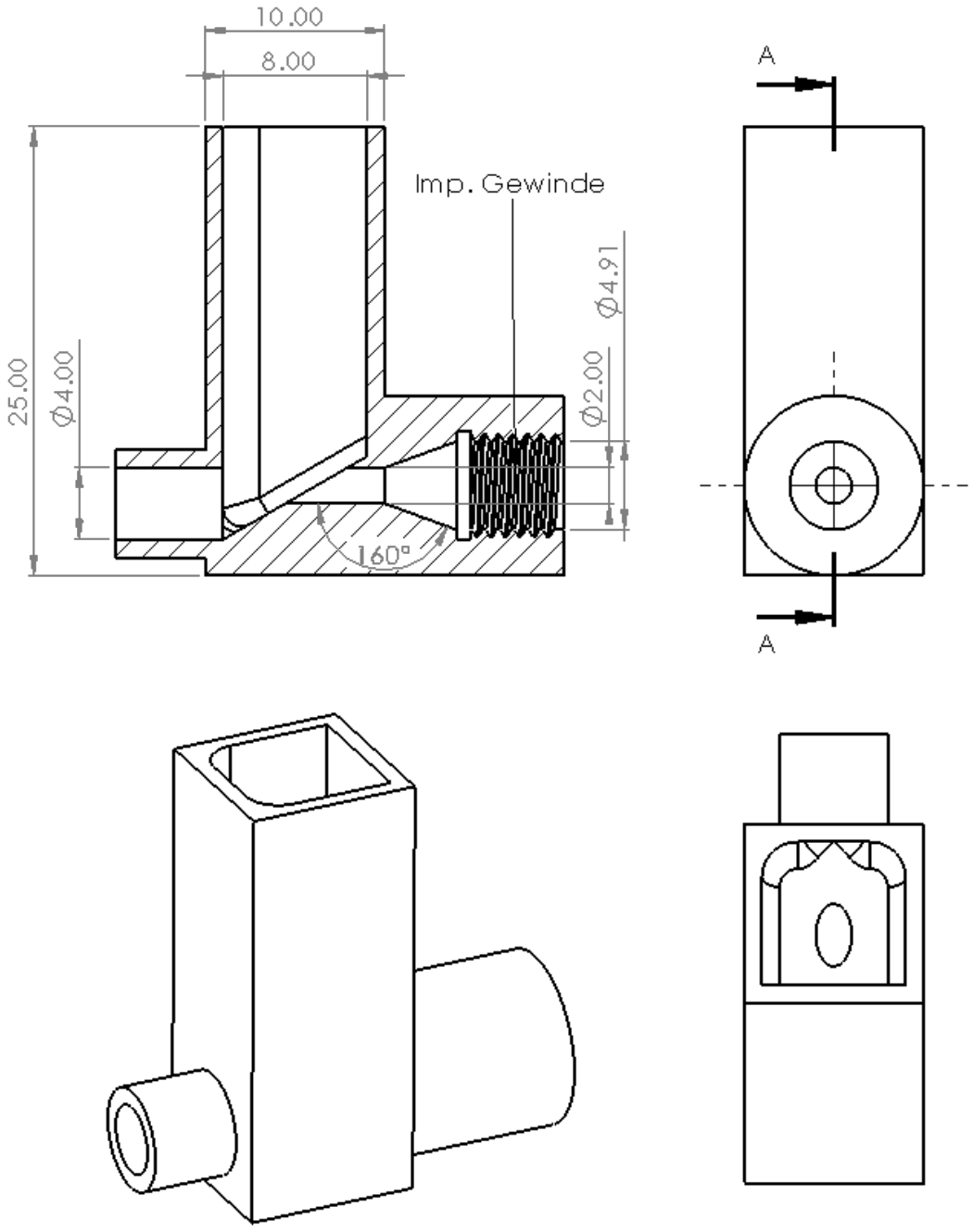

Figure A.5: Schematic drawing of the improved passive feeding reservoir, which was developed based on the experimental results of the experimental series discussed in chapter 5

References

[1] ESA Space Debris Office. *ESA's annual Space Environment Report*. Accessed: 2024-05-10; Assets used with permisson from the original author. 2024. URL: https://www.sdo.esoc.esa.int/environment_report/Space_Environment_Report_latest.pdf.

[2] Gil Denis et al. "From new space to big space: How commercial space dream is becoming a reality". In: *Acta Astronautica* 166 (2020), pp. 431–443. ISSN: 0094-5765.

[3] République Française. *French Space Operations Act n°2008-518 of 3rd June 2008*. Accessed: 2024-08-08. URL: https://www.legifrance.gouv.fr/loda/id/JORFTEXT000018931380.

[4] République Française. *Decree on Technical Regulation issued pursuant to Act n°2008-518 of 3rd June 2008, 31 March 2011*. Accessed: 2024-08-08. URL: https://www.legifrance.gouv.fr/loda/id/JORFTEXT000024095828.

[5] Paulo C. Lozano, Manuel Martínez-Sánchez, and Vlad Hruby. "Electrospray Propulsion". In: *Encyclopedia of Aerospace Engineering*. 2010. DOI: 10.1002/9780470686652.eae121.

[6] David Krejci et al. "Flight heritage of Indium-based FEEP propulsion systems across different applications and orbits: In space cleaning of extractor electrode". In: *38th International Electric Propulsion Conference, Toulouse*. IEPC-2024-279. 2024.

[7] ENPULSION GmbH. *Available Thruster Comparison*. Accessed: 2024-09-23. 2024. URL: https://www.enpulsion.com/order/.

[8] Katharina Huhn et al. "Investigation of the emission behavior of miniaturized SU-8 based colloid emitters". In: *33rd International Electric Propulsion Conference, Washington DC*. IEPC-2013-141. 2013. URL: http://electricrocket.org/IEPC/nl5kwbt2.pdf.

[9] Katharina Huhn et al. "Colloid emitters in photostructurable polymer technology: Fabrication and characterization progress report". In: *34th International Electric Propulsion Conference, Kobe*. IEPC-2015-120. 2015. URL: http://electricrocket.org/IEPC/IEPC-2015-120_ISTS-2015-b-120.pdf.

[10] Torsten Henning, Katharina Huhn, and Peter J. Klar. “Characterisation of electrospray microemitters fabricated by planar and 3D photolithography”. In: *36th International Electric Propulsion Conference (IEPC), Vienna*. IEPC-2019-344. 2019. URL: http://electricrocket.org/2019/344.pdf.

[11] Robert S. Legge and Paulo C. Lozano. “Electrospray Propulsion Based on Emitters Microfabricated in Porous Metals”. In: *Journal of Propulsion and Power* 27.2 (2011), pp. 485–495. DOI: 10.2514/1.50037.

[12] Manuel Gamero-Castaño and Marc Galobardes-Esteban. “Electrospray propulsion: Modeling of the beams of droplets and ions of highly conducting propellants”. In: *Journal of Applied Physics* 131.1 (Jan. 2022), p. 013307. ISSN: 0021-8979. DOI: 10.1063/5.0073380.

[13] Paul R. Chiarot, Pierre Sullivan, and Ridha Ben Mrad. “An Overview of Electrospray Applications in MEMS and Microfluidic Systems”. In: *Journal of Microelectromechanical Systems* 20.6 (2011), pp. 1241–1249. DOI: 10.1109/JMEMS.2011.2168810.

[14] K. Holste et al. “Ion thrusters for electric propulsion: Scientific issues developing a niche technology into a game changer”. In: *Review of Scientific Instruments* 91.6 (June 2020), p. 061101. DOI: 10.1063/5.0010134.

[15] Torsten Henning et al. “Miniaturized Electrospray Thrusters”. In: *IEEE Transactions on Plasma Science* 46.2 (2018), pp. 214–218. DOI: 10.1109/TPS.2017.2755373.

[16] David Krejci et al. “Design and Characterization of a Scalable ion Electrospray Propulsion System”. In: *34th International Electric Propulsion Conference and 6th Nano-satellite Symposium, Hyogo-Kobe*. IEPC-2015-149/ISTS-2015-b-149. 2015.

[17] Richard G. Forbes and Neboysha N. Ljepojevic. “Liquid-metal ion source theory: electrohydrodynamics and emitter shape”. In: *Surface Science* 266.1 (1992), pp. 170–175. ISSN: 0039-6028. DOI: 10.1016/0039-6028(92)91016-5.

[18] Ivanhoe Vasiljevich et al. “Development of an Indium mN-FEEP Thruster”. In: *44th AIAA/ASME/SAE/ASEE Joint Propulsion Conference & Exhibit*. 2008. DOI: 10.2514/6.2008-4534.

[19] Tony Schönherr et al. “Development, Production, and Testing of the IFM Nano FEEP Thruster”. In: *36th International Electric Propulsion Conference, Vienna*. IEPC-2019-362. 2019.

[20] Juergen Mueller. “Thruster options for microspacecraft - A review and evaluation of existing hardware and emerging technologies”. In: *33rd Joint Propulsion Conf. and Exhibit*. AIAA 97-3058. American Institute of Aeronautics and Astronautics, Inc., 1997. DOI: 10.2514/6.1997-3058.

[21] Benjamin St. Peter et al. “Electrospray Propulsion Engineering Toolkit (ESPET)”. In: *Aerospace* 7.7 (2020). ISSN: 2226-4310. DOI: 10.3390/aerospace7070091.

[22] Manel Caballero-Pérez and Manuel Gamero-Castaño. “Increasing Specific Impulse in Electrospray Devices through Emitter Design”. In: *38th International Electric Propulsion Conference, Toulouse*. IEPC-2024-558. 2024.

[23] Fynn L. Kunze, Torsten Henning, and Peter J. Klar. “Taking internally wetted capillary electrospray emitters to the sub-ten-micrometer scale with 3D microlithography”. In: *AIP Advances* 11.10 (2021), p. 105315. DOI: 10.1063/5.0066619.

[24] Fynn L. Kunze, Torsten Henning, and Peter J. Klar. “3D micro printed capillary electrospray thruster with a fully modular integrated extraction electrode”. In: *Journal of Electric Propulsion* 3.3 (2024). DOI: 10.1007/s44205-023-00066-7.

[25] Juergen Mueller, Richard Hofer, and John Ziemer. *Survey of propulsion technologies applicable to cubesats*. Version V2. 2010. DOI: 2014/41627.

[26] L.F. Velasquez-Garcia, A.I. Akinwande, and M. Martinez-Sanchez. “A Micro-Fabricated Linear Array of Electrospray Emitters for Thruster Applications”. In: *Journal of Microelectromechanical Systems* 15.5 (2006), pp. 1260–1271. DOI: 10.1109/JMEMS.2006.879707.

[27] L.F. Velasquez-Garcia, A.I. Akinwande, and M. Martinez-Sanchez. “A Planar Array of Micro-Fabricated Electrospray Emitters for Thruster Applications”. In: *Journal of Microelectromechanical Systems* 15.5 (2006), pp. 1272–1280. DOI: 10.1109/JMEMS.2006.879710.

[28] Francisco José Blázquez-Plaza, Andrés Barrado, and Mick Wijnen. “Experimental Validation of Electrospray Thrusters Current Balancing for Spacecraft Charging Mitigation”. In: *38th International Electric Propulsion Conference, Toulouse*. IEPC-2024-142. 2024.

[29] Stéphane Mazouffre. “Electric propulsion for satellites and spacecraft: established technologies and novel approaches”. In: *Plasma Sources Science and Technology* 25.3 (2016), p. 033002. DOI: 10.1088/0963-0252/25/3/033002.

[30] Richard E. Wirz et al. “Electrospray Thruster Performance and Lifetime Investigation for the LISA Mission”. In: *AIAA Propulsion and Energy 2019 Forum*. DOI: 10.2514/6.2019-3816.

[31] Peter Wright, Anirudh Thuppul, and Richard E. Wirz. “Life-Limiting Emission Modes for Electrospray Thrusters”. In: *2018 Joint Propulsion Conference*. AIAA 2018-4726. DOI: 10.2514/6.2018-4726.

[32] Enric Gustan-Gutierrez and Manuel Gamero-Castaño. “Microfabricated Electrospray Thruster Array with High Hydraulic Resistance Channels”. In: *Journal of Propulsion and Power* 33.4 (July 2017), pp. 984–991. DOI: 10.2514/1.B36268.

[33] John B. Fenn et al. “Electrospray ionization–principles and practice”. In: *Mass Spectrometry Reviews* 9.1 (1990), pp. 37–70. DOI: 0.1002/mas.1280090103.

[34] John B. Fenn. “Ion formation from charged droplets: roles of geometry, energy, and time”. In: *Journal of the American Society for Mass Spectrometry* 4.7 (1993), pp. 524–535. ISSN: 1044-0305. DOI: https://doi.org/10.1016/1044-0305(93)85014-O. URL: https://www.sciencedirect.com/science/article/pii/104403059385014O.

[35] Paul Kebarle and Liang Tang. “From ions in solution to ions in the gas phase - the mechanism of electrospray mass spectrometry”. In: *Analytical Chemistry* 65.22 (1993), 972A–986A. DOI: 10.1021/ac00070a001.

[36] Geoffrey Ingram Taylor. “Disintegration of water drops in an electric field”. In: *Proceedings of the Royal Society of London. Series A. Mathematical and Physical Sciences* 280.1382 (1964), pp. 383–397. DOI: 10.1098/rspa.1964.0151.

[37] Sachin K. Singh and Arunkumar Subramanian. “Phase-field simulations of electrohydrodynamic jetting for printing nano-to-microscopic constructs”. In: *RSC Adv.* 10 (42 2020), pp. 25022–25028. DOI: 10.1039/D0RA04214E.

[38] Simon J. Gaskell. “Electrospray: Principles and Practice”. In: *Journal of Mass Spectrometry* 32.7 (1997), pp. 677–688. DOI: 10.1002/(SICI)1096-9888(199707)32:7<677::AID-JMS536>3.0.CO;2-G.

[39] Juan Fernández de la Mora. “The Fluid Dynamics of Taylor Cones”. In: *Annual Review of Fluid Mechanics* 39.Volume 39, 2007 (2007), pp. 217–243. ISSN: 1545-4479. DOI: 10.1146/annurev.fluid.39.050905.110159.

[40] Elaine M. Petro et al. “Multiscale modeling of electrospray ion emission”. In: *Journal of Applied Physics* 131.19 (May 2022), p. 193301. ISSN: 0021-8979. DOI: 10.1063/5.0065615.

[41] Peter Wright et al. “Novel Variable Mode Emitter for Electrospray Thrusters”. In: *Presented at the 36th International Electric Propulsion Conference, Vienna.* IEPC-2019-650.

[42] Joan Rosell-Llompart, Jordi Grifoll, and Ignacio G. Loscertales. “Electrosprays in the cone-jet mode: From Taylor cone formation to spray development”. In: *Journal of Aerosol Science* 125 (2018), pp. 2–31. ISSN: 0021-8502. DOI: 10.1016/j.jaerosci.2018.04.008.

[43] Nolan M. Uchizono et al. “Emission Modes in Electrospray Thrusters Operating with High Conductivity Ionic Liquids”. In: *Aerospace* 7.10 (2020). ISSN: 2226-4310. DOI: 10.3390/aerospace7100141.

[44] Manuel Gamero-Castaño and M. Magnani. “The minimum flow rate of electrosprays in the cone-jet mode”. In: *Journal of Fluid Mechanics* 876 (2019), 553–572. DOI: 10.1017/jfm.2019.569.

[45] M. Cloupeau and B. Prunet-Foch. “Electrostatic spraying of liquids in cone-jet mode”. In: *Journal of Electrostatics* 22.2 (1989), pp. 135–159. ISSN: 0304-3886. DOI: https://doi.org/10.1016/0304-3886(89)90081-8. URL: https://www.sciencedirect.com/science/article/pii/0304388689900818.

[46] Paulo Lozano, Benajmin Glass, and Manuel Martinez-Sanchez. "Novel Variable Mode Emitter for Electrospray Thrusters". In: *Presented at the 29th International Electric Propulsion Conference, Princeton University*. IIEPC-2005-192.

[47] N. M. Uchizono et al. "The role of secondary species emission in vacuum facility effects for electrospray thrusters". In: *Journal of Applied Physics* 130.14 (Oct. 2021), p. 143301. ISSN: 0021-8979. DOI: 10.1063/5.0063476.

[48] Chengjin Huang et al. "Experimental investigation on current modes of ionic liquid electrospray from a coned porous emitter". In: *Acta Astronautica* 183 (2021), pp. 286–299. ISSN: 0094-5765. DOI: 10.1016/j.actaastro.2021.03.014.

[49] Benjamin D. Prince, Bruce A. Fritz, and Yu-Hui Chiu. "Ionic Liquids in Electrospray Propulsion Systems". In: *Ionic Liquids: Science and Applications*. Chap. 2, pp. 27–49. DOI: 10.1021/bk-2012-1117.ch002.

[50] Suhail Chamieh et al. "Additive Manufacturing and Characterization of Porous Glass Electrospray Emitters". In: *38th International Electric Propulsion Conference, Toulouse*. IEPC-2024-744. 2024.

[51] Fumiya Tachibana, Toshiyuki Tsuchiya, and Yoshinori Takao. "Uniform needle-emitter arrays for ionic liquid electrospray thrusters with precise thrust control". In: *Japanese Journal of Applied Physics* 60.SC (2021), SCCL06. DOI: 10.35848/1347-4065/abe997.

[52] E. Jane Maxwell, Xuefei Zhong, and David D. Y. Chen. "Asymmetrical Emitter Geometries for Increased Range of Stable Electrospray Flow Rates". In: *Analytical Chemistry* 82.20 (2010), pp. 8377–8381. DOI: 10.1021/ac1017953.

[53] David Villegas-Prados et al. "Emission characterization of externally wetted electrospray thrusters using computed tomography". In: *38th International Electric Propulsion Conference, Toulouse*. IEPC-2024-744. 2024.

[54] Johann C. Poggendorf. "Über elektrische Spitzenwirkung". In: *Annalen der Physik und Chemie*. Vol. 215. 1870, pp. 341–349.

[55] Adam L. Collins et al. "Assessment of Grid Impingement for Electrospray Thruster Lifetime". In: *Presented at the 36th International Electric Propulsion Conference, Vienna*. IEPC-2019-213. 2019.

[56] Kevin D. Sampson et al. "Design and Preliminary Progress of the Scalable, Nanofabricated, Advanced Ionic Liquid (SNAIL) Thruster". In: *38th International Electric Propulsion Conference, Toulouse*. EPC-2024-212. 2024.

[57] Koki Takagi et al. "Simple model of multi-scale and multi-site emissions for porous ionic liquid electrospray thrusters". In: *Journal of Applied Physics* 135.24 (June 2024), p. 244502. ISSN: 0021-8979. DOI: 10.1063/5.0195699.

[58] Uwe Scheithauer et al. "Alternative Process Routes to Manufacture Porous Ceramics—Opportunities and Challenges". In: *Materials* 12.4 (2019). ISSN: 1996-1944. DOI: 10.3390/ma12040663. URL: https://www.mdpi.com/1996-1944/12/4/663.

[59] M R Natisin et al. “Fabrication and characterization of a fully conventionally machined, high-performance porous-media electrospray thruster”. In: *Journal of Micromechanics and Microengineering* 30.11 (2020), p. 115021. DOI: 10.1088/1361-6439/abb8c3.

[60] Nobel Prize Outreach AB. *The Nobel Prize in Chemistry 2002*. Accessed: 2024-09-05. 2002. URL: https://www.nobelprize.org/prizes/chemistry/2002/summary/.

[61] Enric Lluis Grustan-Gutierrez. “Multiplexing of electrospray sources for space propulsion and physical sputtering”. URL: https://escholarship.org/uc/item/87z193nc.

[62] Busek Co.Inc. *Available Thruster Comparison*. Accessed: 2024-09-23. 2024. URL: https://static1.squarespace.com/static/60df2bfb6db9752ed1d79d44/t/61292b0fa097083a87c4ce1f/1630087953271/BETMAX_v1.0.pdf.

[63] ienai SPACE inc. *Thruster specifiactions of ATHENA*. Accessed: 2024-10-07. URL: https://ienai.space/.

[64] Andreas Gebhardt. *Understanding additive manufacturing*. Hanser publications Munich, Germany: 2011. ISBN: 978-3-446-43162-1.

[65] Athanasios Goulas and Ross J. Friel. *Practical 3D Printers*. 2012. DOI: 10.1007/978-1-4302-4393-9.

[66] Amanda Su and Subhi J. Al’Aref. “Chapter 1 - History of 3D Printing”. In: *3D Printing Applications in Cardiovascular Medicine*. Ed. by Subhi J. Al’Aref et al. Boston: Academic Press, 2018, pp. 1–10. ISBN: 978-0-12-803917-5. DOI: 10.1016/B978-0-12-803917-5.00001-8.

[67] Chuan Huang et al. “Electrospray Deposition of Energetic Polymer Nanocomposites with High Mass Particle Loadings: A Prelude to 3D Printing of Rocket Motors”. In: *Advanced Engineering Materials* 17.1 (2014), pp. 95–101. DOI: 10.1002/adem.201400151.

[68] Jeongwoo Lee et al. “A review on 3D printed smart devices for 4D printing”. In: *International Journal of Precision Engineering and Manufacturing-Green Technology* 4 (2017), 373–383. DOI: 0.1007/s40684-017-0042-x.

[69] Igor Levchenko et al. “Additive Technologies and Materials for the Next-Generation CubeSats and Small Satellites”. In: *Advanced Functional Materials* (), p. 2407602. DOI: 10.1002/adfm.202407602.

[70] Athanasios Goulas and Ross J. Friel. “3D printing with moondust”. In: *Rapid Prototyping Journal* 22 (6 2016), pp. 864–870. ISSN: 1355-2546. DOI: 10.1108/RPJ-02-2015-0022.

[71] Daniel J. Thomas. “Advanced active-gas 3D printing of 436 stainless steel for future rocket engine structure manufacture”. In: *Journal of Manufacturing Processes* 74 (2022), pp. 256–265. ISSN: 1526-6125. DOI: https://doi.org/10.1016/j.jmapro.2021.12.037.

[72] Mallikarjuna N. Nadagouda, Vandita Rastogi, and Megan Ginn. "A review on 3D printing techniques for medical applications". In: *Current Opinion in Chemical Engineering* 28 (2020), pp. 152–157. ISSN: 2211-3398. DOI: 10.1016/j.coche.2020.05.007.

[73] Ada-Ioana Bunea et al. "Micro 3D Printing by Two-Photon Polymerization: Configurations and Parameters for the Nanoscribe System". In: *Micro* 1.2 (2021), pp. 164–180. ISSN: 2673-8023. DOI: 10.3390/micro1020013.

[74] Xiaoqin Zhou, Yihong Hou, and Jieqiong Lin. "A review on the processing accuracy of two-photon polymerization". In: *AIP Advances* 5.3 (Mar. 2015), p. 030701. ISSN: 2158-3226. DOI: 10.1063/1.4916886.

[75] Andreas Ostendorf and Boris N Chichkov. "Two-photon polymerization: a new approach to micromachining". In: *Photonics spectra* 40.10 (2006), p. 72. URL: https://www.photonics.com/Articles/Two-Photon_Polymerization_A_New_Approach_to/a26907.

[76] Brian H. Cumpston et al. "Two-photon polymerization initiators for three-dimensional optical data storage and microfabrication". In: *Nature* 398.6722 (1999), pp. 51–54. ISSN: 1476-4687. DOI: 10.1038/17989.

[77] Marco Carlotti and Virgilio Mattoli. "Functional Materials for Two-Photon Polymerization in Microfabrication". In: *Small* 15.40 (2019), p. 1902687. DOI: 10.1002/smll.201902687.

[78] Yihong Liu, David D. Nolte, and Laura J. Pyrak-Nolte. "Large-format fabrication by two-photon polymerization in SU-8". In: *Applied Physics A* 100.1 (2010), pp. 181–191. ISSN: 1432-0630. DOI: 10.1007/s00339-010-5735-8.

[79] *Multiphoton Lithography: Techniques, Materials, and Applications*. John Wiley & Sons, 2016. ISBN: 978-3-527-33717-0.

[80] Alexander K. Nguyen and Roger J. Narayan. "Two-photon polymerization for biological applications". In: *Materials Today* 20.6 (2017), pp. 314–322. ISSN: 1369-7021. DOI: 10.1016/j.mattod.2017.06.004.

[81] V. Harinarayana and Y.C. Shin. "Two-photon lithography for three-dimensional fabrication in micro/nanoscale regime: A comprehensive review". In: *Optics & Laser Technology* 142 (2021), p. 107180. ISSN: 0030-3992. DOI: 10.1016/j.optlastec.2021.107180.

[82] Edvinas Skliutas et al. "Polymerization mechanisms initiated by spatio-temporally confined light". In: *Nanophotonics* 10.4 (2021), pp. 1211–1242. DOI: doi:10.1515/nanoph-2020-0551. URL: https://doi.org/10.1515/nanoph-2020-0551.

[83] *Optical Spectroscopy: Methods and Instrumentations*. Elsevier Science, 2006. ISBN: 978-0-444-52126-2. DOI: 10.1016/B978-0-444-52126-2.X5024-2.

[84] *NanoGuide*. Infromation for NanoScribe PPGT devices and printing procedures; Accessed: 2024-09-05. URL: https://support.nanoscribe.com/hc/en-gb.

[85] Douglas R. MacFarlane, Mega Kar, and Jennifer M. Pringle. *Fundamentals of Ionic Liquids*. Wiley-VCH, Weinheim, Germany, 2017. DOI: 10.1002/9783527340033.

[86] Pardeep Singh et al., eds. *Handbook of Ionic Liquids: Fundamentals, Applications, and Sustainability*. Wiley-VCH, Weinheim, Germany, 2024. DOI: 10.1002/9783527839520.

[87] Zhigang Lei et al. "Introduction: Ionic Liquids". In: *Chemical Reviews* 117.10 (2017), pp. 6633–6635. DOI: 10.1021/acs.chemrev.7b00246.

[88] Paulo Lozano and Manuel Martinez-Sanchez. "Efficiency Estimation of EMI-BF4 Ionic Liquid Electrospray Thrusters". In: *41st AIAA/ASME/SAE/ASEE Joint Propulsion Conference & Exhibit*. 2005, AIAA 2005–4388. URL: https://arc.aiaa.org/doi/pdf/10.2514/6.2005-4388.

[89] B. Gassend et al. "Fabrication of a fully integrated electrospray array with applications to space propulsion". In: *IEEE 21st International Conference on Micro Electro Mechanical Systems*. 2008, pp. 976–979. DOI: 10.1109/MEMSYS.2008.4443821.

[90] A. Kazakov et al. *NIST Standard Reference Database 147: NIST Ionic Liquids Database - (ILThermo)*. Accessed: 2024-08-13. 2024. URL: https://ilthermo.boulder.nist.gov.

[91] Paul Nancarrow and Hanin Mohammed. "Ionic Liquids in Space Technology – Current and Future Trends". In: *ChemBioEng Reviews* 4.2 (2017), pp. 106–119. DOI: 10.1002/cben.201600021.

[92] G. B. Appetecchi, M. Montanino, and S. Passerini. "Ionic Liquid-Based Electrolytes for High Energy, Safer Lithium Batteries". In: *Ionic Liquids: Science and Applications*. Chap. 4, pp. 67–128. DOI: 10.1021/bk-2012-1117.ch004.

[93] Brian Donius and Joshua Rovey. "Analysis and Prediction of Dual-Mode Chemical and Electric Ionic Liquid Propulsion Performance". In: *48th AIAA Aerospace Sciences Meeting Including the New Horizons Forum and Aerospace Exposition*. 2010. DOI: 10.2514/6.2010-1328.

[94] Masaki Yamagata et al. "The First Lithium-ion Battery with Ionic Liquid Electrolyte Demonstrated in Extreme Environment of Space". In: *Electrochemistry* 83.10 (2015), pp. 918–924. DOI: 10.5796/electrochemistry.83.918.

[95] Stefan Schneider et al. "Ionic Liquid Fuels for Chemical Propulsion". In: *Ionic Liquids: Science and Applications*. Chap. 1, pp. 1–25. DOI: 10.1021/bk-2012-1117.ch001.

[96] S.V. Stovbun et al. "Synthesis and testing of hypergolic ionic liquids for chemical propulsion". In: *Acta Astronautica* 135 (2017), pp. 110–113. ISSN: 0094-5765. DOI: https://doi.org/10.1016/j.actaastro.2016.11.047.

[97] Amelia R. Bruno, Matthew N. Corrado, and Paulo C. Lozano. "Temperature-Dependent Performance of Electrospray Thrusters with ASCENT Monopropellant". In: *38th International Electric Propulsion Conference, Toulouse*. IEPC-2024-782. 2024.

[98] Szymon Dworski and Charlie N. Ryan. "Analysis of Plumes Produced by Novel Ionic Liquids in Electrospray Thrusters". In: *38th International Electric Propulsion Conference, Toulouse*. IEPC-2024-346. 2024.

[99] Szymon Dworski et al. "Performance of a 50 W Porous Electrospray Thruster in Preparation for Flight". In: *38th International Electric Propulsion Conference, Toulouse*. IEPC-2024-350. 2024.

[100] Albert Cisquella-Serra, Marc Galobardes-Esteban, and Manuel Gamero-Castaño. "Scalable Microfabrication of Multi-Emitter Arrays in Silicon for a Compact Microfluidic Electrospray Propulsion System". In: *ACS Applied Materials & Interfaces* 14.38 (2022), pp. 43527–43537. DOI: 10.1021/acsami.2c12716.

Acknowledgements

Hiermit möchte ich mich bei allen bedanken, die mir im Verlauf meiner Promotion und darüber hinaus zur Seite gestaden haben.

Besonders möchte ich meinem Doktorvater, Peter Klar, danken, der es mir ermöglicht hat nach meinem Lehramtsstudium eine Promotion anzutreten. Ihm ist es zu verdankten, dass ich meinen Interessen in der Raumfahrt nachgehen und zur Forschung in dem Feld beitragen konnte. Ich weiß es sehr zu schätzen, dass ich auf so einem interessanten Projekt arbeiten durfte. Er war auch immer mit Rat zur Stelle, wenn es Komplikationen im Projekt gab.

Auch möchte ich mich bei meinem Zweitgutachter Stefan Schippers und den anderen Mitgliedern der Prüfungskommission Hans Leiter und Chris Volkmar bedanken, dass Sie mich durch das Ende meiner Promotion begleiten.

Ein weiter Dank gilt allen Kollegen und Freunden am Institut und in der Arbeitsgruppe. Dies gilt insbesondre für Torsten und Nathalie, die immer als Unterstützung im Reinraum da waren, Kristof, der immer hilfreichen Input zu experimentellen Problemen hatte, sowie alle Kollegen aus dem 4. Stock und den Raumfahren. Danke für die super Arbeitsatmosphäre. Wegen euch hat es immer Spaß gemacht ins Institut zu kommen und auf Dienstreise zu fahren.

Weiterhin möchte ich meinen Freunden, dem Mawi-Clan, danken, die mich in die Gruppe adoptiert haben. Danke auch für all eure Hilfe innerhalb und außerhalb der Uni. Es ist immer lustig und spaßig mit euch!

Auch möchte ich mich bei meiner Freundin bedanken, die immer für mich da ist. Egal ob ich mal schlechte Laune habe oder nicht weiter weiß, du bist immer eine Stütze in meinem Leben.

Einen besondern Dank möchte ich an meine Eltern richten, die immer in jeder Lebenslage für mich da waren. Eure bedingungslose Untersetzung und Liebe haben mich zu dem gemacht der ich heute bin. Ohne euch wäre ich nie so weit gekommen. Ihr habt es mir möglich gemacht zu Studieren und letztlich auch meine Promotion anzutreten.

DANKE! EUCH ALLEN!

Declaration

I declare that I have completed this dissertation single-handedly without the unauthorized help of a second party and only with the assistance acknowledged therein. I have appropriately acknowledged and cited all text passages that are derived verbatim from or are based on the content of published work of others, and all information relating to verbal communications. I consent to the use of an anti-plagiarism software to check my thesis. I have abided by the principles of good scientific conduct laid down in the charter of the Justus Liebig University Giessen „Satzung der Justus-Liebig-Universität Gießen zur Sicherung guter wissenschaftlicher Praxis“ in carrying out the investigations described in the dissertation.

Date

Signature